2014-09-02

Nano Mechanical Machining Using AFM Probe

Mostofa, Md Golam

UNIVERSITY OF CALGARY

Nano Mechanical Machining Using AFM Probe

By

Md. Golam Mostofa

A THESIS

SUBMITTED TO THE FACULTY OF GRADUATE STUDIES

IN PARTIAL FULFILLMENT OF THE REQUIREMENTS FOR THE

DEGREE OF DOCTOR OF PHILOSOPHY

DEPARTMENT OF MECHANICAL AND MANUFACTURING ENGINEERING

CALGARY, ALBERTA

AUGUST, 2014

ABSTRACT

Complex miniaturized components with high form accuracy will play key roles in the future development of many products, as they provide portability, disposability, lower material consumption in production, low power consumption during operation and higher heat transfer due to their very high surface-to-volume ratio. Given the high market demand for such micro and nano featured components, different manufacturing methods have been developed for their fabrication. The common technologies in micro/nano fabrication are photolithography, electron beam lithography and other semiconductor processing techniques.

Although these methods are capable of fabricating micro/nano structures with a resolution of less than a few nanometers, the shortcomings associated with these methods are, production costs for customized products, limited material choices, necessitate the development of other fabricating techniques. An atomic force microscope (AFM) probe based nano fabrication, has, therefore, been used to overcome some the major restrictions of the traditional processes. This technique removes material from the workpiece by engaging micro/nano size cutting tool (i.e. AFM probe) and is applicable on a wider range of materials compared to the photolithographic process.

In spite of the unique benefits of nano mechanical machining, there are also some challenges with this technique, such as size effects, burr formations, chip adhesions, fragility of tools and tool wear. Moreover, AFM based machining does not have any rotational movement, which makes fabrication of 3D features more difficult. Thus, vibration-assisted machining is

introduced into AFM probe based nano mechanical machining to overcome the limitations associated with the conventional AFM scribing.

In this study, scratching tests are performed with a single crystal diamond AFM probe to investigate the cutting characteristics and model the ploughing cutting forces. Calibration of the probe for lateral force measurements is extended through the force balance method. Furthermore, vibration-assisted machining system is developed and applied to fabricate different materials to overcome material selection issue.

The novelty of this study includes the application of vibration-assisted AFM probe based nano scale machining to fabricate micro/nano scale features, calibration of an AFM by considering different factors, and the investigation of the nano scale material removal process from a different perspective.

ACKNOWLEDGEMENTS

I am heartily grateful to those who made this thesis possible, especially my supervisor, Dr. Simon Park, whose encouragements, guidance and support from the initial to the final level provided me with the opportunity to understand the subject and complete this project. My parents (Md. Nazrul Islam and Sufea Islam) and siblings (Nilufa, Ruma and Nasima) deserve special mention for the encouragement and support they offered during my stay in Calgary. I also would like to offer my gratitude to Dr. Martin Jun from University of Victoria for his scientific guidance and support at different stages of this thesis. I appreciate the supervisory committee members who kindly accepted to review this thesis. This project was supported by Alberta Innovates Technology Future (AITF), and Auto21. I am also very thankful to my colleagues - Chaneel Park, Samira Salimi, Mehdi Mahmoodi, Majid Mehrpouya, Amir Kianimanesh, Eldon Graham, Kaushik Parmar, Allen Sandwell, Mohammad Malekian and Dennis Trieu in Micro Engineering Dynamics Automation Laboratory (MEDAL) at the University of Calgary who supported me in many respect during the project. I would like to thank and appreciate the support of my beloved wife (Farzana Sumona Kaderi) at the end of the study. Finally, this thesis is dedicated to the Founding Father of Bangali Nation, Sheikh Mujibur Rahman who led Bangladesh to her liberty.

Table of Contents

List of Tables

List of Figures

List of Symbols and Nomenclature

Symbols	Definition
A	Adhesive Force [nN]
A_1, A_2	Pile-up Area [nm^2]
A_3	Groove Area [nm^2]
A_L, A_m	Lateral and Vertical Contact Area of Probe Tip [nm^2]
D_p	Depth of Penetration [Unit Less]
ΔD	Photo Detector Offset [V/m]
E^*	Reduced Modulus of Elasticity [N/m^2]
F_C	Cutting Force or Lateral Force [μN]
F_T, F_N	Thrust Force or Normal Force [μN]
H	Hardness of Workpiece [GPa]
h	Depth of Groove [nm]
h_c	Critical Uncut Chip Thickness (CUCT) [nm]
h_L	Lateral Chip Thickness [nm]
h_m	Minimum Uncut Chip Thickness (MUCT) [nm]
h_t	Tip Height or Moment Arm [nm]
h_v	Vertical Chip Thickness [nm]
h_1, h_2	Pile-up Height [nm]
h_p	Average Pile-up Height [nm]
h_{er}	Elastic Recovery Ratio [%]
κ	Cutting Coefficients [GPa]
k^*	Contact Stiffness [N/m]
K_V	Normal Spring Constant [N/m]
K_θ	Torsional Spring Constant [N-m/radian]

L	Applied Load or Set Point Force in Wedge Method [μN]
ΔL	Slope of the Lateral Voltage and Z-detector/scanner [V/m]
ΔL^A	Approach Slope [V/m]
ΔL^R	Retract Slope [V/m]
MRR	Material Removal Rate [$\mu m^3/s$]
R_e	Tip Edge Radius [nm]
S_L	Lateral Sensitivity of The Probe [V/μm]
S_V	Vertical Sensitivity of The Probe [V/μm]
t_e	Tilting error (%)
V_f	Feed Rate [μm/s]
V_L	Lateral Voltage Change in PSPD (C-D) [V]
V_V	Vertical Voltage Change in PSPD (A-B) [V]
w	Width of the Trench [nm]
W	Half Width of the Friction Loop [V]
W_V	Groove Volume [μm^3]
W_0	Lateral Voltage Regenerated from F-D Plot [V]
W_0'	Slope of W_0 and Z-scan [V/nm]
Z_f	The Deflection of Cantilever for Cutting Force [nm]
Z_S	Depth of Groove due to Thrust Force [nm]
Z_V	Maximum Displacement of the Workpiece [nm]
α	Lateral Calibration Factor [N/V]
α_a	Apex or Semi Angle [°]
α_e	Effective Rake Angle [°]
β	Vertical Calibration Factor [N/V]
γ	Angle of Tip Offset [°]

θ	Facet Angle [°]
ϕ	Angle of the cantilever with respect to sample surface [°]
φ	Angle of the Sample Slope [°]
$\delta_{cantilever}$	Defection of the Cantilever [nm]
Δ	Offset of the Friction Loop [°]
Δ_0	Vertical Voltage Regenerated from F-D Plot [V]
Δ_0'	Slope of Δ_0 and Z-scan [V/nm]
$\mu = F_C/F_T$	Apparent Friction Coefficient [Unit less]
μ_p	Ploughing Friction Coefficient [Unit less]
μ_a	Adhesion Friction Coefficient [Unit less]
μ_s	Friction Coefficient between Diamond Like Carbon and Si
μ_{def}	Deformation Friction Coefficient [Unit less]
η	Angle that the Normal Vector Makes with Respect to the Feed Direction [°]

CHAPTER 1. INTRODUCTION

Micro and nano scale products are experiencing rapidly growing market demands due to their reduced size [Chau et al., 2005], light weight, low power consumption and reduced material requirements. Photolithographic masks [Notargiacomo et al., 1999], labs-on-chips [Vijay et al., 2004] and micro lens arrays [Yabu et al., 2005; Karp et al., 2010] are some examples of miniature devices that are used widely. Labs-on-chips are commonly used in chemical and biological sampling applications to identify certain components or diseases from a small amount of the sample and by using a small amount of chemical reagent. Micro lens arrays are also used in industry to increase the light intensity of products.

Micro/nano products require specific techniques for fabrication that are different from conventional macro fabricating techniques. The most common micro/nano component fabrication process is the photolithography process, which includes LIGA (lithography, electroplating and moulding) [Becker et al., 2002], dip-pen lithography [Piner et al., 2012], nano imprint lithography [Hirai et al., 2002], nano sphere lithography [Christy et al., 2001] and electron beam lithography [Vieu et al., 2000]. Although these processes can make small-scaled products, the expenses associated with clean room facilities, chemicals and equipment, such as metrology tools and mask-making equipment, impose a major restriction on the wide use of these techniques. In spite of their applications on some selective materials, such as silicon and glass wafers, these techniques are difficult to be employed in the fabrication of customized products with

high aspect ratios and three-dimensional (3D) features. As an alternative, tool based micro/nano mechanical machining processes are employed in fabrications.

Mechanical machining, which is defined as the continuous removal of material from a bulk material to generate the desired shape, is cost effective compared to photolithography methods in manufacture of customized micro/nano featured products. With the aid of precise control of the machine tool, such as single crystal diamond cutting tool, it is possible to fabricate components with surface roughness in sub micrometer.

Atomic force microscope (AFM) probe based nano mechanical machining is an unique mechanical machining method that is capable of fabricating small features on different materials. The AFM was primarily developed to perform topographic measurements on material surfaces to obtain surface roughness, high-resolution topography, phase images and tribological parameters [Magonov et al., 1997; Wei et al., 2006]. The AFM has a cantilever probe that can apply very small-scale forces (10^{-18} N) [Binnig et al., 1985] on materials. By applying constant force on the material when the probe is in contact with the workpiece and moving the workpiece [Ruan et al., 1994; Ahn et al., 2009; Malekian et al., 2010], the AFM probe can remove small amounts of material from the workpiece. The process is called nano scribing or nano scratching. This feature makes the AFM probe based machining independent of the material type and allows it to be applied to any material provided that the applied force overpowers the workpiece's material strength.

As the scale decreases in AFM probe based machining, the size effect phenomenon dominates the behaviour of the material/probe interaction. The

consequences of this phenomenon increase the hardness of the material [Lucca et al., 2010] and the flow stress of the material [Malekian et al., 2010]. As a result, in AFM probe based nano mechanical machining, the wear rate of the cutting tool increases. The cutting force needs to be monitored to reduce friction forces and improve the probe life and the quality of the machined features.

There are also some challenges in the AFM setup related to the rotating component, which prevents the AFM probe from direct intermittent cutting and fabricating 3D features. These challenges can be addressed by using vibration-assisted cutting where the workpiece can be rotated or vibrated. The reduced cutting forces in vibration-assisted cutting can increase the productivity of the single point tool based machining at the nano scale. The tool wear is thereby reduced in vibration-assisted machining, as the cutting tools experience less cutting forces and rubbing.

In order to employ vibration-assisted cutting in the AFM setup, the vertical axis of the AFM moves up and down to bring the cantilever to the surface, and the XY stage is used to move the workpiece in the lateral directions, i.e. the X or Y axes. Single axis actuation could be used to apply one-dimensional (1D) vibration-assisted cutting [Mostofa et al., 2010], but it has been proven that two-dimensional (2D) vibration-assisted cutting [Ahn et al., 1999] generates better surface quality, due to the reduction in the per cycle chip thickness [Cerniway, 2001]. Therefore, it is necessary to combine both the X- and Y-axis movements to generate circular or elliptical motion to assist in the generation of intermittent cutting.

The fabrication of 3D features requires movement along an additional axis to compensate for the features in the depth-of-cut direction. This requirement is fulfilled either by moving the AFM probe with the Z-stage or by moving the workpiece by attaching an additional actuator to the material, which can move the workpiece in the vertical direction.

The application of vibration-assisted machining in the nano scale is more challenging than the micro/macro scales due to the very small size of the cutting tool. In the AFM probe setup, where the cutting tool sizes are a few micrometers and the tip radius is in the nano scale (few nano meters), use of vibration-assisted nano machining encounters even more challenges. However, tool-based vibration-assisted machining with reduced cutting forces and additional rotational motion can accelerate the nano mechanical machining process, based on the applied cutting frequency and feed rate, which increases production and brings about a unique benefit over the conventional AFM probe based machining. The successful application of vibration-assisted nano mechanical machining can facilitate the fabrication of a wide range of materials with complex 3D features and better surface finishes.

1.1 Motivations

There are few groups (i.e. Korea, USA, U.K., Germany, and Canada) in the world who are working on the AFM probe based nano mechanical machining, and interests in AFM probe based nano mechanical machining is growing. The nano mechanical machining is more attractive compare to the lithography process due to its little

environmental footprint as no chemical is used. In addition, the process allows to measure topography and mechanical properties without removing the workpiece.

There are several challenges in nano mechanical machining because material behaves differently as the scale goes down, the accurate measurement of the cutting force is difficult as conventional force sensors can not be used, tool dynamics, vibration, temperature, humidity, tool wear, and fragility. The tool shape plays an important role in nano scale machining [Park et al., 2008], and a cutting tool with different tip orientation can perform ploughing and shearing where other experimental conditions are same.

The accurate measurements of the cutting forces are difficult but the measurement is important to understand the cutting mechanism in nano scale as direct visual observation of the cutting process is not possible or difficult. The calibration of AFM to measure the cutting forces in nano mechanical machining is another challenge due to its complexity and takes long time. Besides, many parameters used in calibration process are provided by the manufacturer and some of them vary such as facet angle of the calibration artifact.

Fabricating nano features by AFM probe based scribing can limit the cutting in many ways such as limited depth, and width machined channel and requires multiple cycle of cutting to obtain more depth of cut which does more rubbing of the AFM probe and will result in more wear. In vibration assisted cutting, the tool wear is smaller as it removes the material by intermittent way (tool comes in contact with the workpiece only when the cutting occurs) which removes the excessive rubbing of the tool. The chip

thickness reduces in vibration assisted machining; therefore, the cutting forces are lower which contributes less wear of the tool.

The challenges in nano scribing methods can be eliminated if vibration assisted nano mechanical machining can be applied. However, the challenges associated with the vibration assisted nano mechanical machining is attempted to solve in this thesis.

1.2 Objectives

The significant improvement in the efficiency and productivity of vibration-assisted tool based micro fabrication, compared with conventional machining, has inspired much research in this field. However, applying this technique in nano scale contains several challenges in different aspects. In this section, the execution of such a process is outlined; and, the objectives toward achieving successful employment of the vibration-assisted tool-based nano mechanical machining for the fabrication of nano scale features are described.

1.2.1 Investigations of Nano Mechanical Machining Behaviour

The first objective is the investigation of scratching on material, prior to introducing vibration-assisted cutting. Conventional AFM probe based nano mechanical machining is studied to understand the nano scale material removal process. The investigations includes monitoring of the cutting forces which includes calibration of the atomic force microscope, burr formations, tool wear and friction coefficients during cutting, as well as the examination of the effects of cutting tool shape and feed rates. By

studying the cutting forces, comprehensive information about friction properties and the material removal process can be obtained.

Accurate measurement of the cutting forces requires precise calibration of the probe in both the vertical and lateral directions [Bahrenberg et al., 2003; Asay et al., 2006; Wang et al., 2007]. The development of a new lateral calibration method is, therefore, considered as a goal of this objective. A model for the ploughing force is also provided, which can predict the flow stress and depth of cut in the nano scale material removal process. The investigations were conducted for both ductile and brittle material as the nano scale machining should be able to work independent to material. The scribing experiment is necessary to perform to compare with the vibration assisted nano mechanical machining in terms of machining efficiency.

1.2.2 Development of 3D Vibration Assisted System

The design and fabrication of a vibration-assisted machining system on the AFM probe is another main goal of this study. The piezo actuator based nano positioning stage is designed to provide the necessary movement to the workpiece through a built-in piezo actuation system in the AFM setup and an additional piezo actuator system (AFM Scanner) attached to the workpiece.

The stage design includes both simulation and experimental investigation. The simulation consists of finite element (FE) analysis to investigate the dynamics of the designed stage. The experimental investigation is related to the measurement and calibration of the displacement of the stage at different operational frequencies of the piezo actuators.

1.2.3 Investigation of Vibration assisted AFM probe Based Machining

The third objective is experimental evaluations of vibration-assisted nano mechanical machining of different material by different method such as 1D, 2D and 3D vibration assisted machining. The results of both conventional and vibration assisted machining methods are compared to investigate the differences in different cutting parameters. The depth identification is performed for both scribing and vibration assisted nano mechanical machining.

1.3 Organization of Thesis

The overall organization of the thesis is as follows: In **Chapter 2,** different studies are presented from the literature on the micro machining, AFM probe-based machining, force modelling and vibration-assisted machining. The lack of research in this area is identified. **Chapter 3** describes the development of vibration assisted nano mechanical machining and its motion control. **Chapter 3** also describes the experimental setup and the extensive calibration of the Atomic Force Microscope. The retrofitted AFM to apply vibration assisted nano mechanical machining setup with different sensors and actuators are explained. The experimental methodology is also described in this section for conventional and scribing methodology.

In **Chapter 4**, the nano scribing of aluminum and soda lime glass are described. The cutting force, depth of groove, friction, minimum uncut chip thickness, ploughing and adhesion friction model are explained. In **Chapter 5**, vibration assisted nano mechanical machining has been applied and different phenomena have been studied.

Later, the studied phenomena are compared between the nano scribing and vibration assisted nano mechanical machining results.

The studied nano scribing and vibration assisted nano mechanical machining is summarized in **Chapter 6** and the contribution of this thesis is discussed.

CHAPTER 2: LITERATURE REVIEW

The fabrication of miniature products through the mechanical cutting process has recently gained great interest due to its unique advantages. In this process, a miniature cutting tool is used to remove material from a workpiece based on the established correlation between the tool geometry and the machined surface. The main advantages of tool-based micro fabrication are its cost-effectiveness and ability to process a wider range of materials. However, the fragile cutting tool, size effects and lack of information about material deformation in the micro scale affect the accuracy of the machined products.

Since the 1940s, many research works have been performed to understand and model macro machining processes. These studies were conducted to increase productivity without applying excessive forces or inducing chatter, i.e. self-excited vibration. In order to overcome the challenges associated with tool-based micro/nano fabrication, researchers have incorporated alternative processes, such as vibration-assisted machining, to the conventional tool-based machining process. Vibration-assisted cutting tool-based machining has played an important role in producing ultra accurate products with minimum loss of the cutting tool life [Shamoto et al., 1999]. However, carbon steel machining with a diamond cutting tool is difficult because of the high tool wear due to carbon diffusion from the diamond tool to carbon steel.

In vibration-assisted machining, a fast servo actuates the cutting tool along one [Mostofa et al., 2010], two [Ahn et al., 1999] or three [Shamoto et al., 2005] axes at a high frequency and generates pulsating cutting. The cutting tool is engaged with the

workpiece only when material removal is necessary, and the cutting occurs during a small fraction of the full cycle. This process reduces both burr formation [Moriwaki et al., 1995] and the average cutting force during machining, while generating a sub-micrometer surface finish.

The working principle of the atomic force microscope (AFM) probe based nano mechanical machining is based on the interaction of the probe tip with the workpiece surface. Depending on the relative position of the probe tip and the workpiece, the probe can experience different potential forces stemming from the atomic forces between the atoms of the tip and those of the workpiece surface. The AFM probe can be brought in contact with the workpiece to remove a small amount of material by scanning the surface (i.e. moving in the horizontal direction) and applying a normal force on the workpiece. The challenges associated with this type of probe based micro/nano mechanical machining are tool wear, burr formation and difficulties in the fabrication of 3D features. These limitations in tool-based machining can be overcome by introducing a vibration-assisted cutting mechanism to the AFM probe based machining system.

In this chapter, literature in the micro/nano mechanical machining area is presented. These research works include studies on size effects, ploughing forces and the use of scratch tests on materials to investigate their behaviour in the micro scale. AFM probe based micro/nano mechanical machining is described in detail, and vibration-assisted machining in the micro/nano scale is elaborated by presenting its applications to the micro/nano mechanical machining process.

2.1 Micro and Nano Mechanical Machining

The micro machining (the term was first introduced by Taniguchi, 1983) capability versus the use of cutting tools, abrasive techniques, energy beam processes such as ion beam, electron beam machining and plus scanning probe techniques for surface measurement and molecular manipulation are shown in Figure 2.1. This graph, which was modified by Byrne et al. [2003], demonstrates the improvement of the machining accuracy over the last few decades for different machining processes.

As the scale is reduced in micro machining, the uncut chip thickness (i.e. depth of cut) decreases and introduces several issues, such as material grain size, tool edge geometry and elastic recovery, which need be investigated in order to understand their effects on the surface quality and accuracy of the machined parts [Chae et al., 2007].

Liu et al., [2004] conducted a comprehensive study of micro machining processes in relation to different factors, such as size effects, minimum chip thickness effect, elasto-plastic deformation and microstructure effects. These factors are introduced in detail in the following sections.

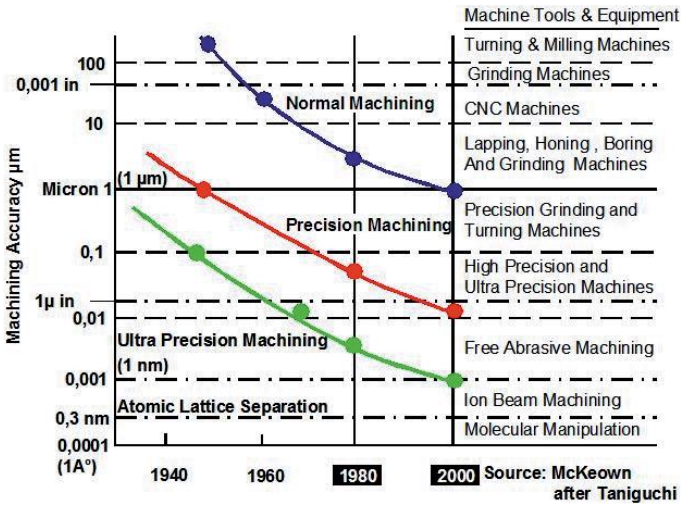

Figure 2.1 Micromachining capabilities over time [Byrne et al., 2003]

2.2 Micro and Nano Scale Phenomena in Machining

Micro and nano mechanical machining differs from macro scale machining in many ways. In macro scale machining there are many parameters that do not affect the cutting mechanism that can affect the micro and nano scale machining such as grain boundaries, surface roughness, tool edge radius and many. Some of the phenomena that affect the micro and nano scale machining are discussed in this section.

2.2.1 Size Effects

One of the most important differences between macro and micro/nano scale machining is that a material's properties and behaviour in the micro/nano scale are highly dependent on size. This is known as size effects. The size effects should be specifically considered in two situations during micro/nano cutting: 1) the uncut chip thickness is

comparable to the edge radius of the tool; and, 2) the microstructure of the material significantly influences the cutting mechanism [Dornfeld et al., 2006]. Downsizing the scale reduces the amount of imperfections per unit volume, reduces the stress concentration points and, hence, reduces material failure during machining. Malekian et al., [2010] has stated that the flow stress (i.e. instantaneous stress that keeps the material flowing during machining) increases due to the size effects in the nano scale during the material removal process.

Unlike with the cutting mechanism in macro machining, which is mainly shearing and chip formation, a material's microstructures play an important role in the cutting mechanism in micro machining. When the edge radius is very small, the grain boundaries of a polycrystalline material play an important role in the chip generation and surface finish [Vogler et al., 2004]. Furukawa et al., [1988] conducted micro machining experiments on an aluminum alloy and studied the cutting force variation corresponding to the grain boundaries. It was concluded in their study that the size effects have an influential role in the cutting mechanism and impact the machining process in different ways.

2.2.2 Minimum Uncut Chip Thickness and Ploughing

The minimum uncut chip thickness (MUCT) is defined as the minimum depth of cut under which the cutting tool does not remove material from the workpiece. Several experiments [Vogler et al., 2004; Malekian et al., 2012] and simulations [Shimada et al., 1993] have been carried out to correlate the MUCT to the cutting parameters, such as

depth of cut and cutting tool edge radius. Based on these studies, the MUCT is highly related to the cutting tool edge radius. The MUCT divides the material removal process into ploughing and shearing regions. If the depth of cut is below the MUCT, the material is pushed under the tool and ploughing occurs; and, if the depth of cut is higher than the MUCT, the material is removed from the workpiece as chips and shearing occurs. Vogler et al., [2004] experimentally obtained the MUCTs for pearlite and ferrite as 0.2 and 0.35 of the edge radius, respectively.

Malekian et al., [2012] recently investigated the MUCT for aluminum and concluded that the stagnant angle (θ_m) and the friction angle ($\beta_s=tan^{-1} F_C/F_T$ when the rake angle is zero) were equal, which resulted in an MUCT equal to 0.23 of the edge radius. Figure 2.2 shows the material flow during micro machining where the chip separation occurs at a stagnant angle (θ_m).

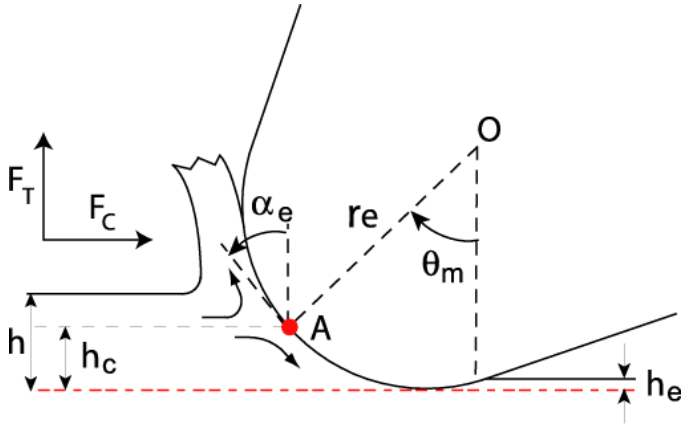

Figure 2.2 Machining using an edge radius tool [Malekian et al., 2011]

Shimada et al., [1993] also performed a molecular dynamic (MD) simulation by modelling the edge radius effects and concluded that MUCT needs to be considered in

simulations to achieve reliable results, since the ploughing process has a significant contribution to the generation of surface roughness. The ploughing mechanism is important in micro mechanical machining, as it causes plastic deformation of the workpiece material without any chip removal. This behaviour results in high cutting forces, specific cutting energy, poor surface finishes and high residual stresses.

2.2.3 Elastic Recovery

In macro scale machining, the depth of cut is quite large; whereas, in micro/nano scale machining, the depth of cut is quite small. Both the ploughing and shearing mechanisms are involved in micro scale machining; therefore, the material is first compressed under the cutting edge and then some portion of the material recovers elastically. This phenomenon, which is known as elastic recovery, plays a key role in micro/nano machining and the modelling of the cutting forces.

Park et al., [2009] considered the elastic recovery effect when modelling the micro milling forces. A scratch test was then performed to measure the elastic recovery by use of a conical tool. Gauthier et al. [2001] also presented experimental results and an analysis of the elastic recovery measurement on a polymeric material. The experimental data were acquired with a conical scratch tool integrated with a built-in microscope, which allowed an in situ analysis of the contact area and the groove left on the surface. The total elasto-plastic penetration depth, h_{ep}, was split into its elastic, h_e, and plastic, h_p, parts, as shown in Figure 2.3. They found that, for most cases, elastic recovery needed to be considered for the accurate prediction of the scratch geometry and the forces.

Unlike in macro cutting operations, when the chip thickness is comparable in size with the edge radius of the tool, there are several scale related phenomena, including the challenges that significantly affect forces, surface finishes, chip formations, tool wear and many others, which need proper investigations.

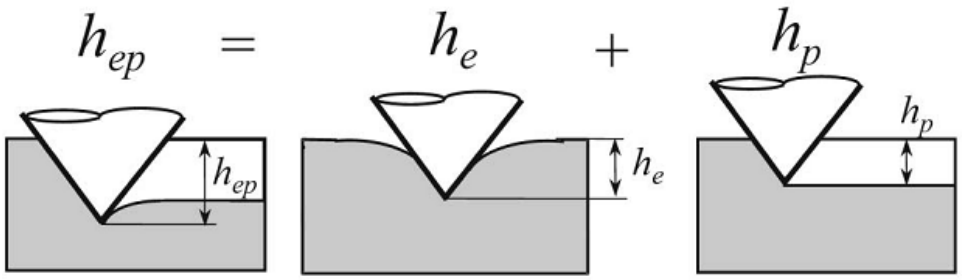

Figure 2.3 Splitting the penetration depth of the tip into the elastic and plastic terms [Gauthier et al., 2001]

2.3 AFM Probe Based Nano Mechanical Machining

The AFM was introduced in the mid 1980s to investigate material properties in the atomic scale. The AFM has also been used in various applications such as scratching, wear and indentation tests and mechanical machining [Bhushan, 2011]. The AFM uses a sharp-tipped probe with a radius of a few nanometers to scan the surface in the atomic scale. As the probe tip is brought near the workpiece surface, two different kinds of forces (i.e. attracting or repelling) act on the probe tip, depending on the distance between the tip and the workpiece. When the cantilever comes into contact with the workpiece in the contact mode, an additional normal force is exerted to the surface by the AFM. As the sample holder moves in the lateral X and Y-directions, the AFM probe removes material from the workpiece surface. By performing precise control over the cutting forces and

scanning speed, it is possible to implement AFM probe based machining in the fabrication of nano scale features.

AFM probe based material manipulation was investigated during a nano scale wear test [Ruan et al., 1994], where silicon nitride tips was used on polymeric magnetic tapes at different loads. Through wear tests, the friction forces and the tribological aspects [Wei et al., 2006; Wang et al., 2008; Shin et al., 2011], such as the velocity dependency of the friction coefficient [Gnecco et al., 2000], were studied. Wear studies can also contribute to the understanding of micro scale material removal in grinding operations. While the applied normal forces in wear tests and the tribological studies were in the nano scale, the magnitude of the applied forces in nano fabrication processes increases to the micro scale with the use of a high stiffness cantilever.

Several studies have used the AFM setup as a mechanical modification tool in experiments on different materials, such as silicon [Ahn et al., 2009], chrome [Malekian et al., 2010], glass [Mostofa et al., 2011] and other metals [Notargiacomo et al., 1999]. Throughout the experiments, different phenomena, such as the feed rate effects on the scratching depth, normal load effects on the scratching depth, friction coefficients, and ploughing and shearing regimes in the course of nano scale material removal, were studied.

One of the advantages of AFM probe based nano mechanical machining is in situ measurement of the fabricated features through another sharper tip without the necessity of removing the workpiece. Using the AFM probe, it is also possible to perform nano indentation tests on the workpiece to investigate different material properties, such as

hardness and modulus of elasticity [Bhushan et al., 2011; Kulkarni et al., 1996]. Nano indentation is considered a nondestructive method, due to the small amount of normal load required in the tests.

There are some of the restrictions associated with the usage of the AFM probe for mechanical machining and tests. The workpiece surface needs to be flat, and the roughness should be small. The stiffness of the cantilever used during the tests should be much higher than normal probes when hard materials are studied. The tool wear, piled-up material, debris and difficulties in the fabrication of 3D shapes are some of the main problems in AFM probe based nano mechanical machining.

2.4 Vibration-Assisted Machining

Introducing controlled vibration to assist the machining process was initiated by many researchers in the late 1950s [Skelton et al., 1968]. These early generations of vibration-assisted machining processes applied vibration in the cutting direction to separate the tool from the chip in each cycle of vibration, reduce friction between the tool and the chip, and ultimately reduce the cutting forces [Moriwaki et al., 1992; Jin et al., 2001]. Since the vibration is applied in a linear fashion, this kind of machining is classified as one-dimensional (1D) vibration-assisted machining [Mostofa et al., 2010]. Figure 2.4 shows 1D vibration-assisted machining and its tool actuator design, which was developed at Pusan National University, Korea.

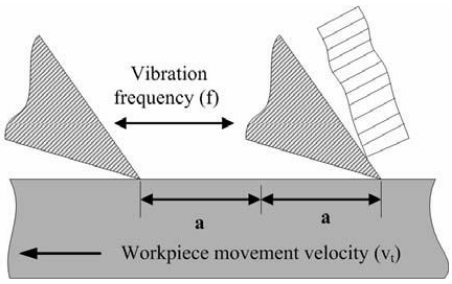

(a)

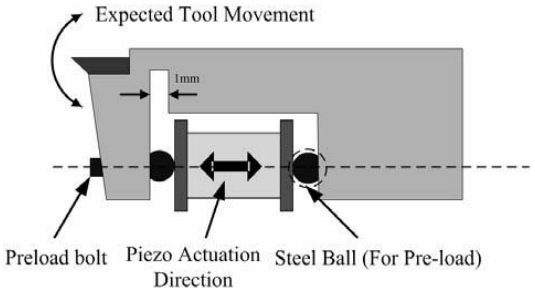

(b)

Figure 2.4 Schematic of (a) 1D vibration-assisted machining and (b) corresponding servo design [Mostofa et al., 2010]

Shamoto et al., [1994] introduced elliptical vibration cutting where, instead of applying 1D linear motion, the cutting tool rotates in an elliptical locus as materials are fed into the tools. This process significantly reduces the required force for machining and improves surface finishes [Shamoto et al., 1994]. Due to its rotational motion in two dimensions, it is classified as two-dimensional (2D) vibration-assisted machining [Ahn et al., 1999]. Figure 2.5 shows the 2D ultrasonic vibration cutting process and relative servo design, which was developed at Pusan National University, Korea.

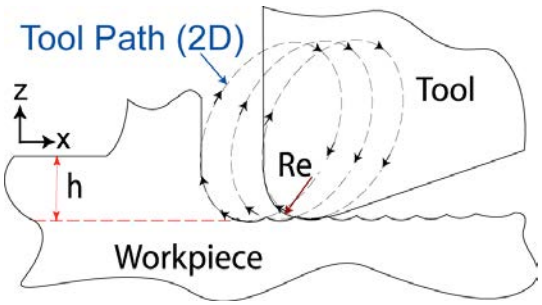

(a)

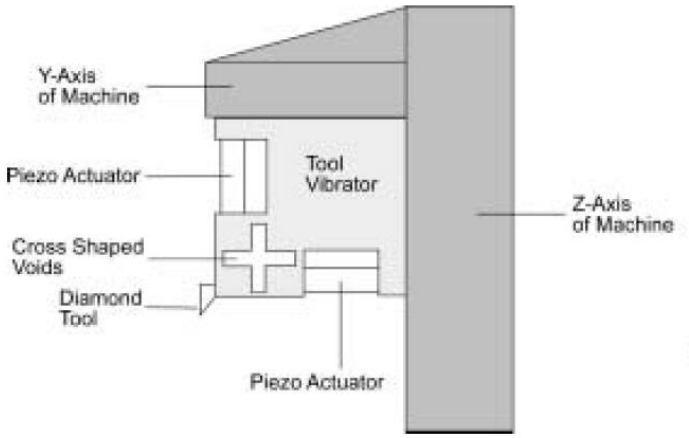

(b)

Figure 2.5 2D ultrasonic vibration cutting: (a) tool tip motion and (b) servo design [Ahn et al., 1999, reproduction was permitted]

The periodic engagement and disengagement of the pulsating cutter in vibration-assisted machining improves the tool-based machining by lowering the cutting forces [Shamoto et al., 1994]. Vibration-assisted machining requires less effort in the surface finishing and burr removal process, as the finished surface has less roughness and fewer burrs [Ahn et al., 1999; Brinksmeier et al., 1999; Shamoto et al., 1994; Shamoto et al., 1999; Ma et al., 2005; Nath et al., 2009].

The cutting forces are also reduced in vibration-assisted cutting, because the chip thickness is considered as the distance between two adjacent elliptical tool paths, and the shear angle changes continuously due to constant change in the rake angle. The sheared chip thickness is lower in elliptical machining (the maximum chip size is the width of the cutting tool or a little more than the tool width for full immersion cutting), and the shear angle is higher compared to conventional machining [Moriwaki et al., 1995]. Tool wear also decreases as the contact between the tool and the workpiece decreases in vibration-assisted machining [Brinksmeier et al, 1999; Shamoto et al., 1999; Cerniway, 2001]. In this type of machining, one complete elliptical path is considered a complete cycle. The cutting tool, which engages with the workpiece for a small fraction of the cycle, experiences less friction from the contact area between the tool and the workpiece. The advantages of vibration assisted machining are listed in Table 2.1.

Ultrasonic vibration-assisted machining is becoming a widespread manufacturing tool in macro/micro scale turning and grinding. However, employment of this technique in the nano scale is still challenging. There are few researchers working on the application of vibration-assisted mechanical machining to the nano scale material removal process. Gozen et al., [2010] developed a customized setup to perform rotating tool-based nano mechanical machining by the AFM probe. They mounted an AFM probe on three-axis actuators to apply circular and elliptical motions for cutting. The limitations associated with the proposed setup are difficulties in the force measurement, unavailability of an in situ imaging system and complexity of the AFM probe mounting on a three-axis stage. Performing the machining also had its own difficulties, where

finding the exact contact point between the workpiece and the nano scale sized tool tip became a major challenge.

Table 2.1 Possible benefits of vibration-assisted machining [Moriwaki et al., 1992 and 1995; Shamoto et al., 1994, 1999, and 2005; Cerniway., 2001; Mostofa et al., 2010]

Benefits of vibration-assisted machining	Remarks
Reduction of forces due to changing of friction force direction	Changing rake and shear angles
Increase in tool life, especially for carbon steel machining	Decreased temperature during machining reduces the carbon affinity
Change in the critical chip thickness	Increases for brittle material
Increase in the surface finish	No need for polishing
Glass cutting	Minimize crack propagation
Reduction of burr formations	Maintaining sharp tools
Minimize ploughing	Minimize residual stress
Nano patterning – improved lubrication delivery	Minimize friction
Reduction of adhesion	Reduces built-up edge (BUE)
Minimize chatter	Reduction of forces and different concept of depths of cuts

2.5 Summary

In AFM probe based machining, the requirements of higher cutting forces, burr formations makes it inefficient as post processing or deburring. On the other hand, the vibration assisted machining can generate a burr free surface or at least less burr formation than nano scribing.

The measurement of the cutting forces is important as it provides frictional information and material removal behaviour. However, measurement of the lateral forces in AFM probe based machining is challenging as the lateral spring constant is difficult to find. Therefore, the force involved in nano scribing and vibration assisted nano mechanical machining is not investigate yet properly.

In this thesis, the challenges of application of vibration assisted nano mechanical machining and investigating the machining phenomena has been resolved by measuring the cutting forces through extensive calibration. A 3-axis vibration assisted system is developed which integrates with AFM machine. This setup can provide a 3-axis vibration to the sample and can be helpful for generating 3D shapes and surface patterning.

The limitations and challenges in conventional machining make it difficult to obtain better machinability. In AFM, the small tool size, limited to scribing, limited tool stiffness and large friction [Malekian et al., 2010] makes the nano scribing process inefficient for nano scale machining. In macro/micro scale machining, the combination of vibration has improved the cutting efficiency from the conventional cutting which includes, orthogonal and milling operation. In AFM probe based scribing, the resonant vibration cutting is not possible as the control of the frequency node is not possible.

Therefore, the non resonant vibration assisted machining could be an approach to apply vibration assisted nano mechanical machining. Beside, the cutting process can be monitored through measurement of the cutting forces shown by Malekian et al., [2010]. The successful application of vibration to AFM cutting will increase the cutting efficiency of nano scale machining, and the rotation motion due to the vibration will help in 3D machining. In applying vibration assisted machining with AFM, 3-axis stage and calibration of AFM is necessary and in the next chapter, the development of 3-axis nano stage, calibration of AFM is described.

CHAPTER 3. EXPERIMENTAL SETUP

In order to fabricate at atomic scale, a commercial atomic force microscope is utilized and retrofitted to achieve the objectives. In this chapter, the atomic force microscope and its basic operating principle are described. The basic lithography process and calibration for measuring the vertical and lateral force are also presented. The development of the 3-axis unit and the methodology to apply vibration to the system for vibration assisted machining are described in this chapter. The control of the vibration system to fabricate in atomic scale is also described.

3.1 Atomic Force Microscope

Atomic force microscopy (AFM) is described as a method of measuring very small forces (as low as 10^{-18}N) and objects as small as 1 Å [Binnig et al., 1985]. The method uses the combination of a scanning tunneling microscope and a stylus (probe). AFM has enabled to scholars to extensively study various areas that were previously impossible to investigate, such as molecular metrology, nano mechanical properties and biological science. Molecular metrology and tribological study at the atomic scale has raised many questions about friction laws in the macro scale; and, scientists are still investigating friction phenomena in the atomic scale [Sills et al., 2003; Barel et al., 2010; Tambe et al., 2005], such as the dependency of kinetic friction on sliding velocity.

In the study of friction, the AFM probe is dragged along the substrate surface; and, the lateral forces, also called as friction force, are measured. The friction coefficient is then calculated; however, the size of the probe plays an important role. In tribological tests, the asperities on the workpiece surface can be deformed physically, and sometimes a small amount of material can be removed [Bhushan., 2005].

The basic working principle of AFM can be described as: the atomic force microscope has a probe (like a stylus), where a tip is attached to a cantilever beam; and, the beam can bend in the vertical and lateral directions, depending on the interaction between the tip and the sample surface. This change in the displacement of the atomic force microscope is used to investigate the interaction between the probe tip and the sample surface.

The working principle can be categorized based on the operational methodology of the atomic force microscope. In non-contact scanning, the AFM probe is excited to its 1st natural frequency and hovers near the workpiece surface (at approximately 50-150 Å). The interaction force changes the frequency of the probe, due to the additional stiffness between the probe tip and the workpiece surface. The change in the frequency is analyzed and transformed into image information.

In contact scanning, a repulsive force acts on the AFM probe from close contact with the sample surface. Therefore, the displacement of the AFM probe due to the repulsive force is analyzed to generate an image. The phase imaging or tapping mode is a combination of contact and non-contact modes, where the vibrating AFM probe taps (alternately touching) the surface instead of only touching the sample. The change in the

phase shift due to intermittent contact is measured and used to generate an image of the sample surface [Jalili et al., 2004]. Figure 3.1 shows the tip-sample distance and the interaction force acting between the tip and the sample surface.

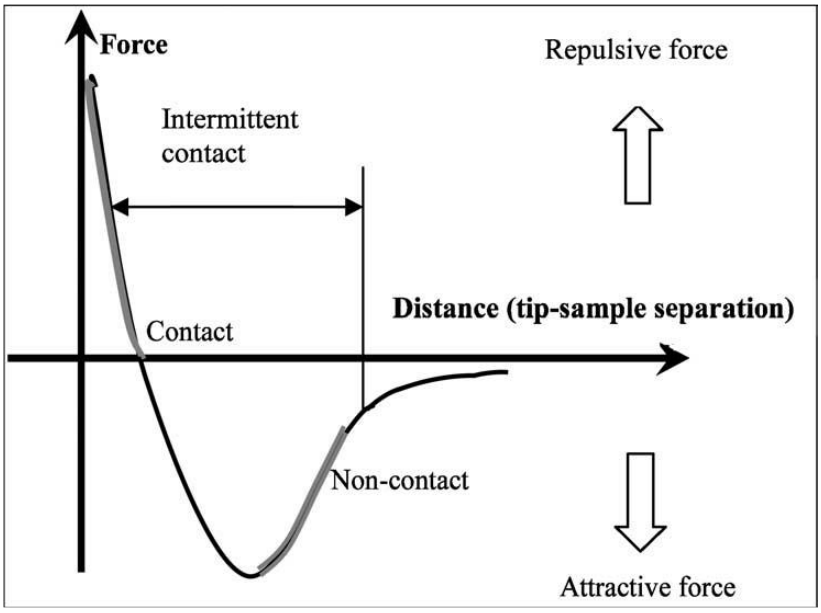

Figure 3.1 Interaction force between the AFM tip and the surface with respect to the distance between them [Jalili et al., 2004]

The AFM probe removes material when in contact mode operation, due to the deformation of the asperities. The AFM probe applies a set point force to maintain the contact between the tip and sample. The applied set point force can be increased, and the AFM probe can penetrate the surface. While moving on the surface, the AFM probe can remove material in the form of chips or can plough the material. Therefore, an AFM probe can be used in nano machining and as nano tool based machining equipment. The set point force during scratching is maintained by a feedback loop of the AFM system and has a bandwidth of 2 kHz.

The schematic shown in Figure 3.2a, describes the basic operating principle of an atomic force microscope. The probe is brought on the surface and depending on the interaction between the probe and sample surface, the cantilever of the probe deflects. The deflection of the AFM probe is sensed by the position sensitive photo diode (PSPD) and generates the voltage. The generated voltage is sent to the computer and controller for imaging and controlling the movement of the X, Y and Z stage. The feed back loop maintains the set point force so that, the AFM probe does not crash. Similar phenomena are carried out while the lithography or nano scribing operation is done. The difference is the set point force magnitude in contact mode operation. In Figure 3.2b, the lithography process is shown where material from the sample surface is removed due to large set point force and the forces acting on the AFM probe which can be measured by calibrating the AFM probe.

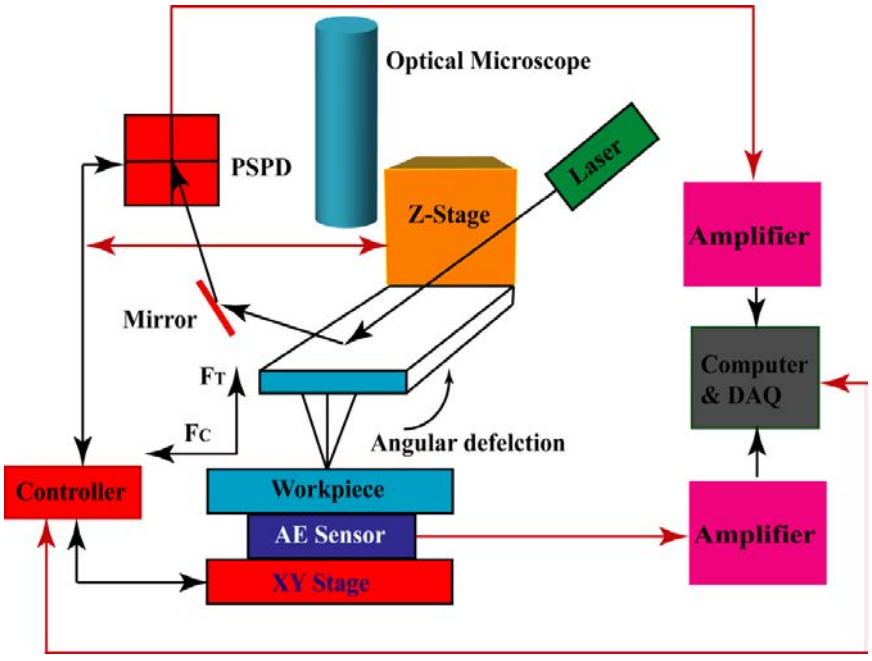

(a)

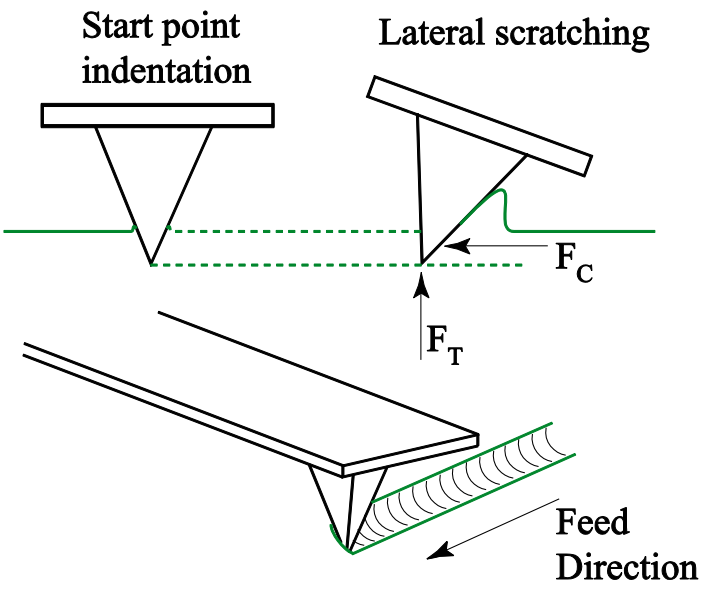

(b)

Figure 3.2 (a) Schematic of the AFM probe based nano scribing experiment and (b) scribing in the lateral direction

The measurement of the cutting forces during nano scribing or vibration assisted cutting is important to understand the material removal process. Therefore, our atomic force microscope has been calibrated to measure the cutting forces involved in nano mechanical machining by AFM. There are various methods to measure the cutting forces and in the following section, all the calibration methods will be discussed and will explain the extension of the existing calibration method.

The AFM can be used to fabricate nano scale features on many engineering materials, some of which are difficult to fabricate using other nano fabrication methods. The small size (a few hundred μm) of the probe with an even smaller tip size (a few nm) makes it difficult for direct observation of the cutting process;

therefore, applied force and lateral cutting forces are measured to investigate the fabrication process. The measurement of the cutting forces in AFM requires calibration of the atomic force microscope in the vertical and lateral directions, in order to measure the vertical and lateral force. The vertical and lateral calibration process is described in the following subsections.

3.2 Calibration of Atomic Force Microscope

In order to accurately measure forces from the deflection of the probe, extensive calibrations of the AFM probe were needed. A laser dependent, position sensitive photo diode (PSPD) can provide voltage readings, depending on the position of the cantilever. The laser deflection changes depending on the displacement of the cantilever as the cantilever deflects during passing over changing topography. To convert voltage signals from the PSPD into cutting (lateral) forces, F_C, and thrust (vertical) forces, F_T, they must be multiplied by calibration constants of α and β, as depicted in Equation 3.1.

$$F_C = \alpha t_e V_L = \frac{K_\theta S_L t_e}{h_t^{\,2}} V_L \quad ;$$
$$F_T = (1 + t_e)\beta V_V = \frac{K_V S_V}{\cos\phi} V_V \qquad 3.1$$

where V_L and V_V are the voltages from the PSPD to the lateral and vertical deflections of the cantilever, respectively; h_t is the moment arm (tip height); S_V and S_L are the vertical and lateral sensitivities, respectively; K_θ and K_V are the torsional and vertical spring

constants for the cantilever, respectively; ϕ is the angle (12° in our case) of the cantilever with respect to the sample surface; and, t_e is the error due to the tilting of the sample.

The thrust force and cutting forces acting on the AFM probe during nano scribing are shown in Figure 3.3. The derivation of the thrust and cutting forces are shown in Equation 3.2 and 3.3. The tilting error components are added after finding the error in calibration which is discussed in the calibration section.

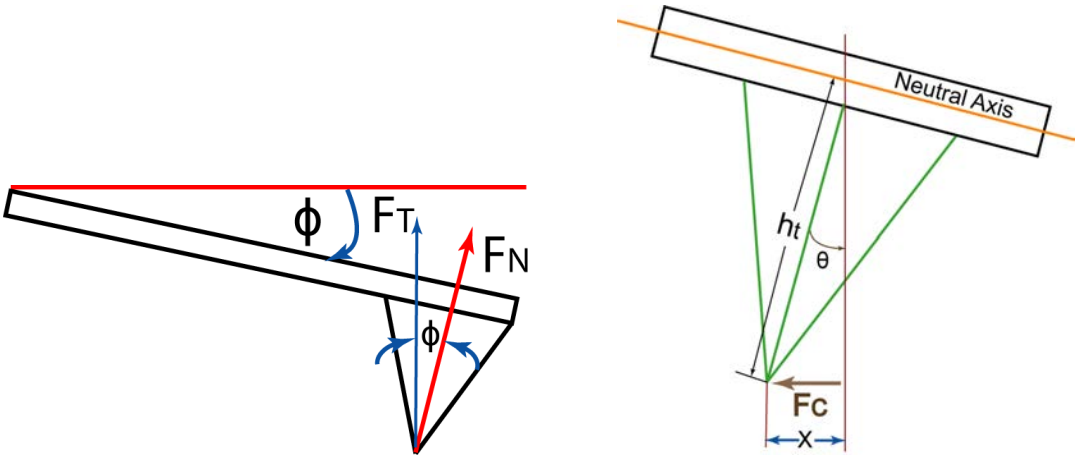

Figure 3.3 (a) Thrust force and (b) cutting force acting on the AFM probe during nano scribing

$$
\begin{aligned}
&F_T = K_V Y \\
&where\, Y = S_V V_V \\
&F_N = F_T \cos\phi = K_V S_V V_V \qquad 3.2 \\
&F_T = \frac{K_V S_V V_V}{\cos\phi} = \beta V_V \;\; where \;\; \beta = \frac{K_V S_V}{\cos\phi_V}
\end{aligned}
$$

$$F_C = K_L X$$

$$where$$

$$X = S_L V_L$$

$$where\, S_L\, is\, Lateral\, Sensitivity\, and\, V_L\, is\, Lateral\, voltage.$$

$$Lateral\, moment\, M_1 = F_C\, h_t = Torsional\, Moment\, M_2 = K_\theta\, \theta \qquad 3.3$$

$$So\, F_C = \frac{K_\theta\, \theta}{h_t}\, where\, \theta \approx \frac{X}{h_t}\, when\, \theta\, is\, small.\, By\, substituting\, \theta,$$

$$F_C \approx \frac{K_\theta\, X}{h_t^{\,2}} \approx \frac{K_\theta\, S_L V_L}{h_t^{\,2}} = \alpha\, S_L V_L \;\; where\; \alpha = \frac{K_\theta S_L}{h_t^{\,2}}$$

3.2.1 Vertical Calibration

In vertical calibration, the stiffness of the cantilever (K_V), vertical sensitivity (S_V) and tilting angle of the cantilever from the horizontal axis need to be determined. The vertical sensitivity factor, S_V, of the PSPD can be obtained through the force-distance (*f-d*) curve by bringing the probe down onto a hard diamond surface as the piezo actuator continues to move down, causing the angle of the cantilever and voltage reading (*A-B*) to change. The S_V is the ratio of the cantilever deflection ($\delta_{cantilever}$) to the corresponding voltage difference obtained from the PSPD shown in Equation 3.4.

$$S_V = \frac{\delta_{cantilever}}{V_V} \qquad 3.4$$

After determining the S_V slope of the retracting plot shown in Figure 3.4, the vertical calibration factor can be found by using Equation 3.1. The S_V was found to be 5.28×10^{-8} m/V from the force-displacement (*f-d*) measurement, as shown in Figure 3.4

where Z-scan values are the displacement of the cantilever the corresponding voltage change.

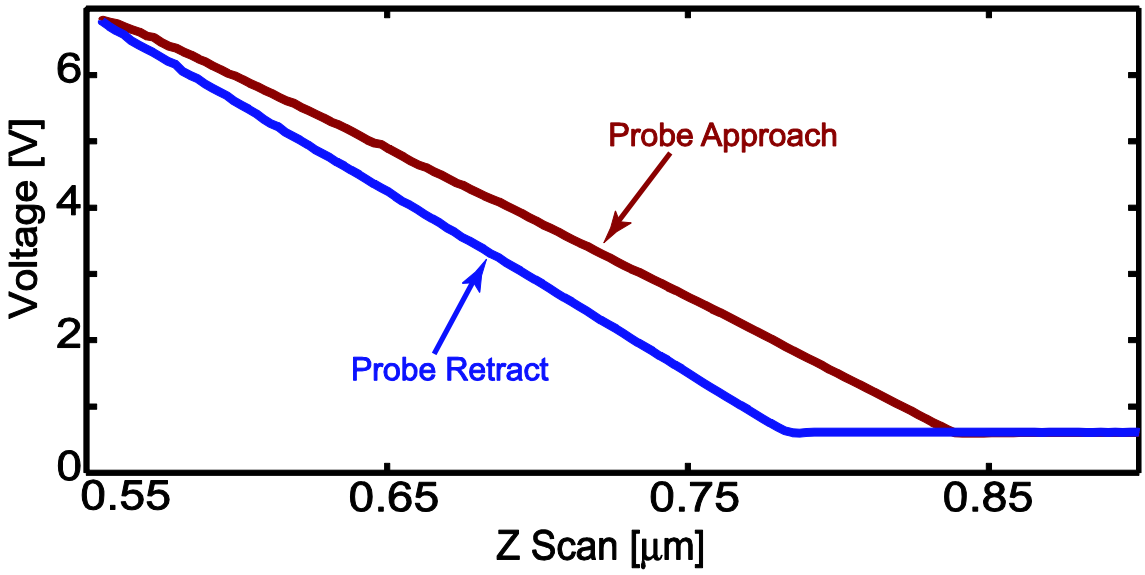

Figure 3.4 Force-displacement measurements to find the vertical sensitivity

3.2.2 Lateral Calibration

There are three different methods that can be applied to calibrate the AFM probe to measure the forces in the lateral direction: the wedge method, the force balance method and the extended force balance method. The extended force balance method was developed in the Micro Engineering Dynamics and Automation Laboratory (MEDAL) at the University of Calgary and applied to compare with other methods. It has shown consistent results in determining the lateral calibration process over other methods. All three methods are described here to give an overview.

3.2.2.1 Wedge Method

The lateral stiffness of a cantilever can be determined experimentally using the wedge method [Varenberg et al., 2003; Wang et al., 2007], which uses a calibration sample with both flat and sloped surfaces with known angles to measure the differences between the frictional forces across the flat surface, both up and down the sloped surface. The calibration samples (MikroMasch TGF11 or TGG01) are used to find the lateral stiffness, as shown in Figure 3.5.

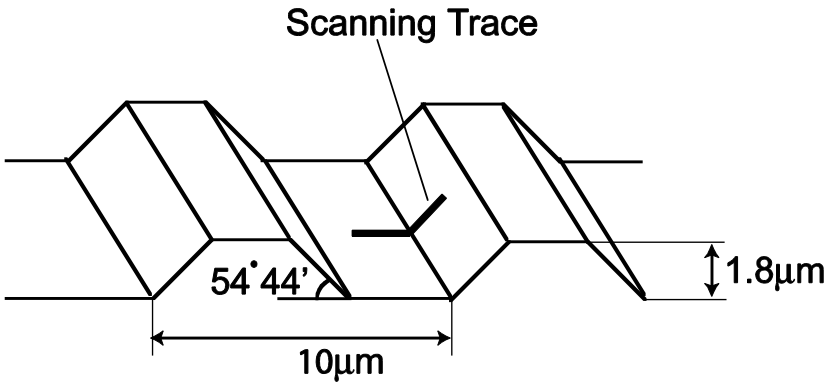

Figure 3.5 A TGF11 calibration sample showing the area to be traced

Friction loops, such as those shown in Figure 3.6, are found as the probe scans (contact mode scanning) over the flat and sloped surfaces with a constant normal force [Wang et al., 2007]. The lateral forces are measured during the contact mode scanning of the calibration artifact. Once the friction loop data is acquired, the first step is to solve for the friction coefficient in the wedge method, μ_w, in the following quadratic equation:

$$\sin\theta(L\cos\theta + A)\mu_w^{\,2} - \frac{\Delta_{slope} - \Delta_{flat}}{W_{slope}}(L + A\cos\theta)\mu_w + L\sin\theta\cos\theta = 0 \qquad 3.5$$

where θ is the angle of the sloped surface; L is the applied load in Newton (N); A is the adhesive force (N), which can be found with an *f-d* curve; Δ is the offset of the friction loop in volts (V); and, W is the half width of the friction loop (V). Solving Equation 3.5 gives two values of μ_w.

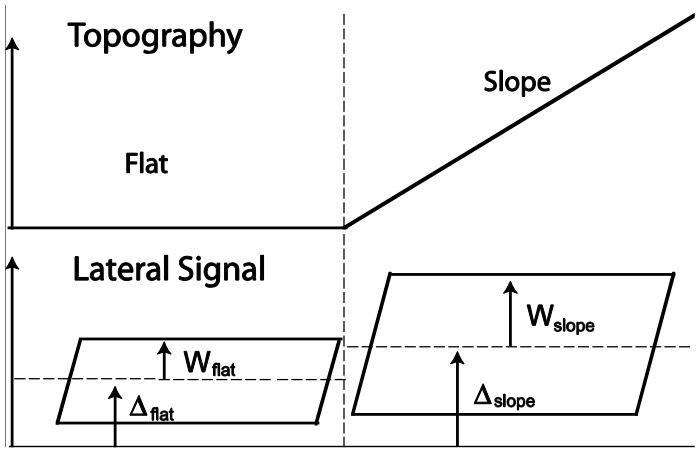

Figure 3.6 Friction loops obtained on flat and sloped surfaces; W is the half width, Δ is the offset of the loop, and both are measured in units of volts

Using μ_1 and μ_2 in Equation 3.6 gives two values of α:

$$\frac{\mu_w(L + A\cos\theta)}{\cos^2\theta - \mu_w{}^2 \sin^2\theta} = \alpha W_{slope} \qquad 3.6$$

Solving for μ_{flat} in Equation 3.7 using α_1 and α_2 gives two values of μ_{flat}:

$$\mu_{flat} = \frac{\alpha W_{flat}}{(L + A)} \qquad 3.7$$

The values of μ_i and $\mu_{i,flat}$ are not equal, but are close to each other. The smallest difference in μ_i and $\mu_{i,flat}$ gives the correct calibration constant, α. Once the calibration constant, α, is found, Equation 3.1 can be used to measure the lateral forces. The advantage of this method is that the friction coefficient is calculated, which can also be used in the force balance method.

3.2.2.2 Force Balance Method

The lateral calibration constant, α, can be found by applying the force balance method [Asay et al., 2006]. Unlike the wedge method, this method is a non-scanning method, ensuring efficient measurement with less damage to the probe tip. This process uses a calibration sample that has both slope and flat facets with a known angle (54.7°).

The method is based on the balancing of forces during *f-d* (force-distance) measurements on the different facets. It requires only normal cantilever stiffness and the angles of the surfaces, and it solves for the lateral calibration constant, α, in N/V (note that this is not the lateral sensitivity), the tip offset angle, γ, and the PSPD offset, ΔD. Figure 3.7 shows the forces acting on the tip while performing *F-D* (force-displacement) measurement, the three facets of the calibration artifact (calibration sample is made of silicon TGF 11) and the Z detector response corresponding to voltage.

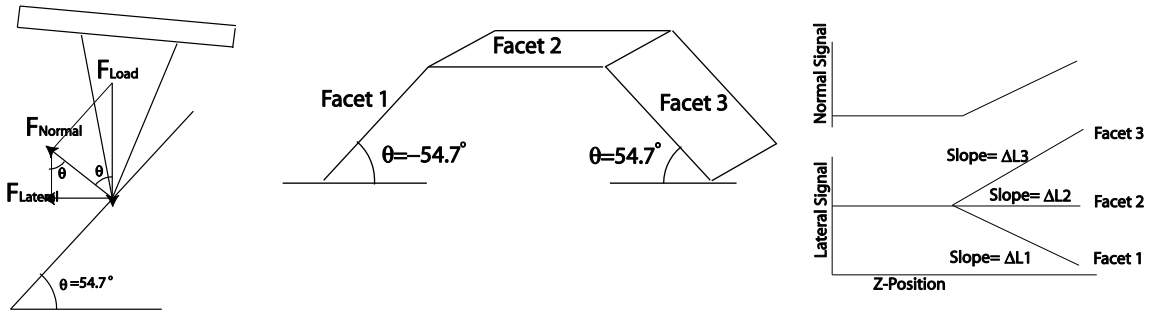

(a) (b) (c)

Figure 3.7 (a) Forces at the tip of the probe, (b) the TGF11 calibration sample showing the three facets, and (c) the voltage versus Z detector graphs produced

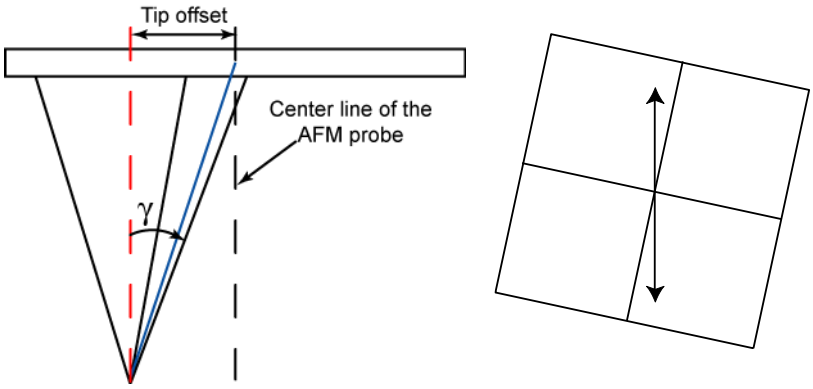

(a) (b)

Figure 3.8 (a) The (exaggerated) offset angle of the tip from the centre of the cantilever, and (b) the displacement of the laser on the PSPD from an *f-d* curve taken on a flat surface when the detector is offset

The force balance method solves for the PSPD and tip offsets. The PSPD offset is caused by misalignment of the PSPD and the cantilever and results in a change in the lateral signal in *F-D* curves, even when the probe is on a flat surface. The tip offset is the amount that the tip is offset from the centre of the cantilever, which causes the probe to twist in one direction more than the other. Figure 3.8 shows the offset angle of the tip from the neutral axis of the cantilever axis and the PSPD offset.

The *f-d* curves are taken on each of the three facets of the calibration sample. The lateral voltage readings *C-D* and Z detector signals are recorded; and, a graph of lateral voltage, as a function of Z displacement is produced, similar to Figure 3.7c. The slopes of the curves produced (V/m) are then used in Equations 3.8, 3.9 and 3.10:

Facet 1 $$(\Delta D + \Delta L_1)\alpha = k_V[\cos(\theta)\sin(\theta - \gamma)] \quad 3.8$$

Facet 2 $$(\Delta D + \Delta L_2)\alpha = k_V[-\sin(\gamma)] \quad 3.9$$

Facet 3 $$(\Delta D + \Delta L_3)\alpha = k_V[\cos(-\theta)\sin(-\theta - \gamma)] \quad 3.10$$

where ΔD is the photo detector offset (V/m), ΔL is the slope of the *C-D* versus *Z* detector curve (V/m), α is the lateral calibration constant (N/V), K_V is the normal spring constant (N/m), θ is the angle of the facet, and γ is the angle of the probe offset.

Equations 3.8, 3.9 and 3.10 do not account for the slipping of the tip during *f-d* measurements. The model assumes that the tip of the probe is stationary on the sample surface as the cantilever twists. To allow for slipping, terms involving the friction between the probe and the sample need to be added. The equations then become:

$$(\Delta D + \Delta L^A)\alpha = k_V[\tan(\theta) + \tan(\gamma)] - \frac{k_V \mu_s}{\cos(\theta)^2 + \mu_s \sin(\theta)\cos(\theta)} \quad 3.11$$

$$(\Delta D + \Delta L^R)\alpha = k_V[\tan(\theta) + \tan(\gamma)] + \frac{k_V \mu_s}{\cos(\theta)^2 - \mu_s \sin(\theta)\cos(\theta)} \quad 3.12$$

where ΔL^A is the approach slope of the facet, ΔL^R is the retract slope of the facet, and μ_s is the coefficient of friction. The friction force can be found using the wedge method or Salvadori's method [2008], but it is very likely that the friction coefficient is small enough that the friction term in Equations 3.11 and 3.12 can be ignored. Solving the system of nonlinear equations gives solutions to γ, ΔD, and α.

3.2.2.3 Extended Force Balance Method

The force balance method is extended [Mostofa et al., 2013] by using a new approach where the force balance is done in a way similar to that of the available force balance method. Figure 3.9 describes the distribution of the force during *f-d* measurement on the inclined facet. To convert voltage signals from the PSPD into thrust (vertical) and cutting (lateral) forces, F_T and F_C, lateral calibration (α) and vertical sensitivity factors are used as Equation 3.1.

The lateral forces are measured based on the torsional displacement of the probe. It is difficult to obtain the accurate torsional spring constant, K_θ, from the theory, due to uncertainties associated with the manufacturing of probe. The wedge [Varenberg et al., 2003] and force balance [Asay et al., 2006] methods can directly acquire the lateral calibration factor, α. The wedge method requires contact mode scanning of the sample to find the difference between the frictional forces across the flat surface, both up and down the sloped surface. However, the scanning experiments have to be performed for several iterations to identify α, and tool wear may occur as a consequence. The force balance method is suggested as an alternative, but requires measuring static *f-d* curves at different slopes. To simplify the lateral calibration procedure, the extended force balance method has been proposed to obtain the lateral calibration factor.

In the extended force balance method, the complex process explained by the force balance method is ignored by removing consideration of the PSPD and probe tip offsets. First, the AFM is calibrated in the vertical direction. For this purpose, the *f-d* experiment

is performed, and the vertical sensitivity of the probe is measured. The vertical calibration factor is then calculated using Equation 3.1.

The extended force balance method also relies on the scanning of sloped artifacts (such as TGF11 as shown in Figure 3.9a) in the contact mode, but scanning of the surface forward and backward once is enough, compared to the many times necessary in the wedge method.

The extended force balance method is based on the determination of the normal force at the sloped surface with respect to the thrust force, which is shown in Figure 3 9b. When the probe is dragged on the artifact, as shown in Figure 3.9b, lateral PSPD voltage signals (*C-D*) are generated, depending on the facets, to determine the torsional bending of the probe. The topography of the calibration artifact is shown in the Figure 3.9a.

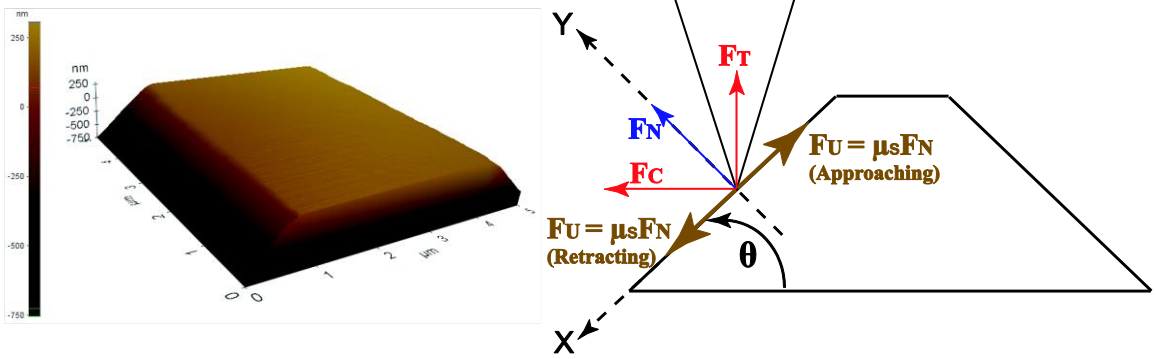

(a) (b)

Figure 3.9 TGF11 calibration sample showing: (a) a scanned image of three facets, and (b) the forces acting at the tip of the probe

From Figure 3.9b, equating the forces on the normal and parallel planes to the sloped surface and balance the forces as:

$$\begin{aligned} &\vec{F}_T + \vec{F}_C = \vec{F}_N + \vec{F}_U \\ &\sum F_X = 0 \; ; \; F_U + F_C \cos\theta - F_T \sin\theta = 0 \\ &\sum F_Y = 0 \; ; \; F_N - F_T \cos\theta - F_C \sin\theta = 0 \end{aligned} \qquad 3.13$$

where F_T is the applied thrust force, F_C is the lateral force, F_U is the friction force and F_N is the normal force acting perpendicular to the sloped surface of the calibration artifact, θ (54.7°) is the facet angle. By equating the sum of forces in both the X- and Y-directions and substituting F_N in to Equation 3.13:

$$\begin{aligned} &\mu\,(F_T \cos\theta + F_C \sin\theta) - F_T \sin\theta + F_C \cos\theta = 0 \\ &F_C \approx \alpha\, V_L \approx \frac{F_T\left(\sin\theta - \mu_s \cos\theta\right)}{\left(\cos\theta + \mu_s \sin\theta\right)} \end{aligned} \qquad 3.14$$

By rearranging Equation 3.14, the lateral calibration factor can be as:

$$\alpha \approx \left(\frac{F_T}{V_L}\right)\left(\frac{\sin\theta - \mu_s \cos\theta}{\cos\theta + \mu_s \sin\theta}\right) \qquad 3.15$$

where μ is the friction coefficient between the probe and the calibration artifact, which is approximately 0.0173 for silicon artifact and diamond like carbon tip [Salvadori et al., 2008]. With Equation 3.15, it was assumed that the probe centre is also the beam centre and that the tilt angle of the artifact is negligible.

Sliding tests were performed on the artifact and found the average approach and retraction lateral voltage, V_L, was 2.171 V from the lateral PSPD signals (*C*-*D*) at the set thrust force, F_T, of 50 μN. The feed rate for approach and retraction was at 0.2 μm/s. The

average lateral calibration factor (α) was found to be 3.136×10^{-5} N/V from Equation 3.15. The calibration procedure was repeated at least six times before the experiment.

The wedge method is a scan-based calibration process where the same calibration artifact is used; however, with two-way, half of the flat facet and half of the slope is scanned to measure the differences between the frictional forces across the flat surface [Malekian et al., 2010], both up and down sloped surface. In the force balance method, the friction coefficient between the probe tip and the workpiece material is needed. The friction coefficient can be obtained from the wedge method and used in the force balance method. There is another method [Salvadori et al., 2008] where the friction coefficient between the tool tip and the workpiece material is obtained separately, independent of the cantilever parameters.

The lateral calibration constant can be obtained through both the wedge and force balance methods. The values have been found to be close; therefore, the force balance method is recommended, so that wear of the probe tip is reduced.

The extended force balance method is a simple and efficient method to find the lateral calibration factor without performing several iterative scans. The deviation of the lateral calibration factor value of the extended force balance method from that of the force balance method was less than 5%. Table 3.1 shows different calibration factors and other parameters related to calibration process.

Table 3.1 Geometry and calibration parameters of the probe

h_t (μm)	θ (deg)	Cantilever Length (μm)	α (N/V)	S_V (m/V)	K_V (N/m)
109	12	636	31.36e-6	5.28e-8	163

3.2.2.4 Investigations of Sources Errors in Calibration Method

In the vertical calibration process, the human error comes from the setting of the sample, which can be tilted. The tilting error can be compensated for by measuring the contribution of the thrust force in the lateral direction. In an ideal case, if the sample is perfectly flat, then there will be zero lateral force when force displacement measurement is performed in vertical direction. Force displacement measurement is performed in 4 different manual setting of the workpiece and in each setting at least 3 f-d measuring experiment is conducted and the average is taken. The voltage change in vertical direction (V_V) and lateral direction (V_L) are measured.

Figure 3.10 shows the measured voltages in vertical and lateral direction corresponding to different thrust force applied in *f-d* measurements. It was observed that, the lateral voltages are not zero and it is increasing with the increase in the thrust force linearly. Therefore, the tilting angle of the sample is contributing to the lateral force, and the measured lateral force is 1.37% higher than the actual cutting force and the thrust force is 1.37% is lower than the actual applied force. This error is can be compensated by introducing an additional tilting error coefficient (t_e) to the thrust force and lateral force equation, which is shown in Equation 3.1. The measured vertical sensitivity is shown in Table 3.2 while the sample is placed at different orientation.

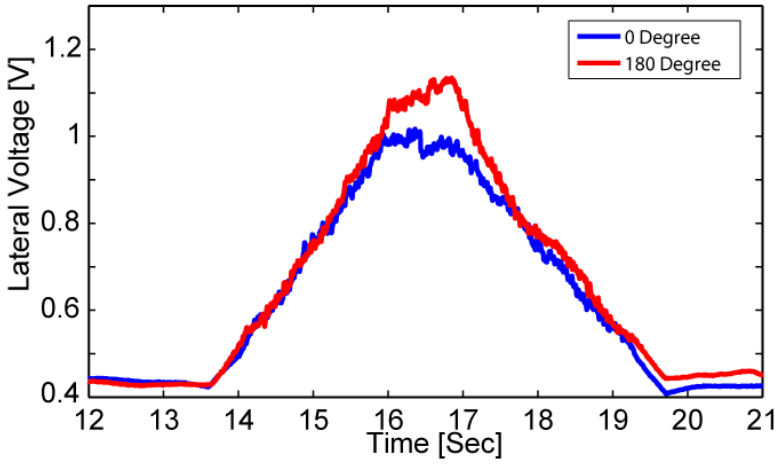

(a)

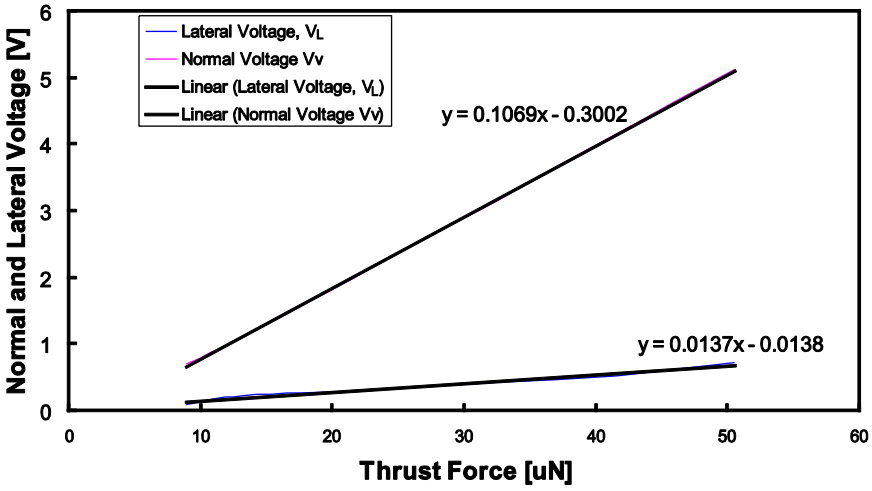

(b)

Figure 3.10 (a) The lateral voltage changes depending on the sample tilting/offset angle at 40 μN thrust force and (b) variation of normal and lateral force corresponding to the thrust force in *f-d* measurement

Table 3.2 Vertical calibration parameters obtained from F-D measurement

Sample Orientation Angle (°)	**Vertical Sensitivity S_V (V/µm)**
0 (Diamond Sample)	14.78
90 (Diamond Sample)	14.19
180 (Diamond Sample)	14.27
270 (Diamond Sample)	14.25

According to the manufacturer, calibration sample (TGF 11) contains features with facet angle of 54.4° but in reality the angle is not perfectly 54.4° which is shown in Figure 3.11. The facet angle varies due to the manufacturing error. Therefore, the facet angle of the calibration artifact is measured several times from AFM scanning images. The facet angle was observed as low as 33.91° and as high as 54.7°. Therefore, the facet angle will definitely affect the lateral calibration factor as the facet angle is a part of the extended force balance method. Six individual facet angles have been measured and the obtained values are 40.72°, 40°, 33.91°, 49.76°, 40.36° and 54.7°. The average facet angle is 43.24°.

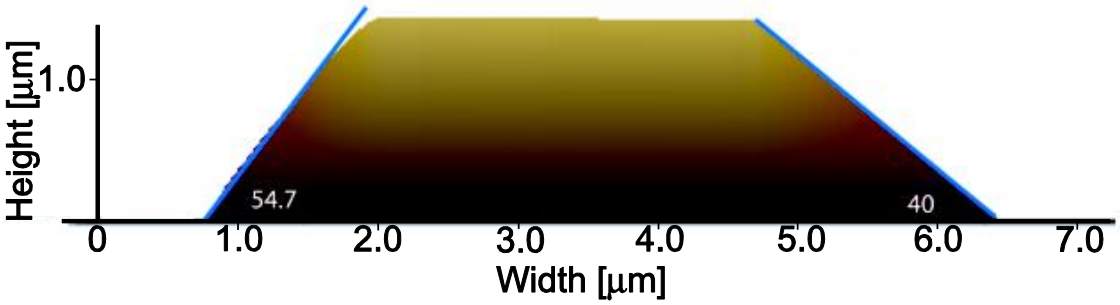

Figure 3.11 Variation of facet angle of the calibration artefact (TGF 11)

The friction coefficient used previously (0.0173) was measured by Salvadori [2008] between diamond like carbon (DLC) and silicon. The AFM probe used in this thesis was made of a sapphire cantilever and a single crystal diamond. The calibration artifact was made of silicon; therefore, the friction coefficient may not be similar for single crystal diamond and silicon. The friction coefficient was investigated using Salvadori's method for the diamond probe and silicon; and, the findings are reported in the following paragraphs, Equation 3.16, Figures 3.13–3.14 and Table 3.3.

The friction coefficient can be measured by using Equation 3.16.

$$\mu_s + \frac{1}{\mu_s} = \frac{2\Delta_0'}{W_0' \sin(2)} \qquad 3.16$$

The calibration artifact (TGF 11) was scanned over a 2 μm^2 area in such a way that the scanned area covered half of the flat facet and half of the sloped facet shown in Figure 3.12.

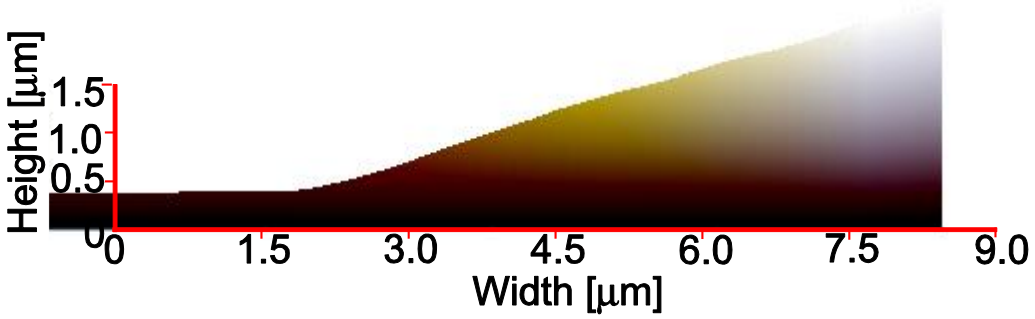

Figure 3.12 Scanned area of TGF 11 calibration artifact showing flat and slope surfaces

The F-D test was performed on the slope and vertical force, and the lateral force was measured in voltage. The Z-scanner data was also captured in µm. The vertical and lateral force data was plotted against the Z-scanner values and the slopes were calculated, as shown in Figures 3.13 and 3.14. The friction coefficient can be calculated using the measured slope in Equation 3.16. The slopes and friction coefficients for different repeated experiments were calculated; and, the average friction coefficient was found to be $0.0329^{+0.006}_{-0.005}$ for diamond and silicon, as shown in Table 3.3. The effect of the friction coefficient on the calibration factor was calculated, and it was found that the calculated friction coefficient could affect the calibration factor by 1.0 to 1.22 %. The nonlinearity in Figure 3.13 may come from two different sources. During force displacement measurement, the cantilever jumps to contact the workpiece due to the attractive force during the approach to the surface and jumps from contact due to the adhesion force during retraction of the cantilever [Capella et al., 1999].

Table 3.3 Friction coefficients measured between the diamond and silicon

Δ_0 Slope	Δ_W Slope	Friction Coefficient (μ_s)	Mean μ_s
-0.00625	0.0007547	0.0332	$0.0329^{+0.006}_{-0.005}$
-0.006326	0.0008956	0.039	
-0.006157	0.0007101	0.0317	
-0.006116	0.0006207	0.0279	

Tool edge radius information was also provided by the manufacturer; however, the tip radius was also measured from a scanning electron microscope (SEM) image. Figure 3.15a shows the approximate the tool edge radius (25 nm) as indicated by the manufacturer. Following the method suggested by the manufacturer, as illustrated in Figure 3.15a, the original SEM image in Figure 3.15c was magnified and analyzed, as shown in Figure 3.15b. The measurement shows that the measured tip radius (24.89 nm) deviated by 0.11 nm from the value provided by the manufacturer (25 nm).

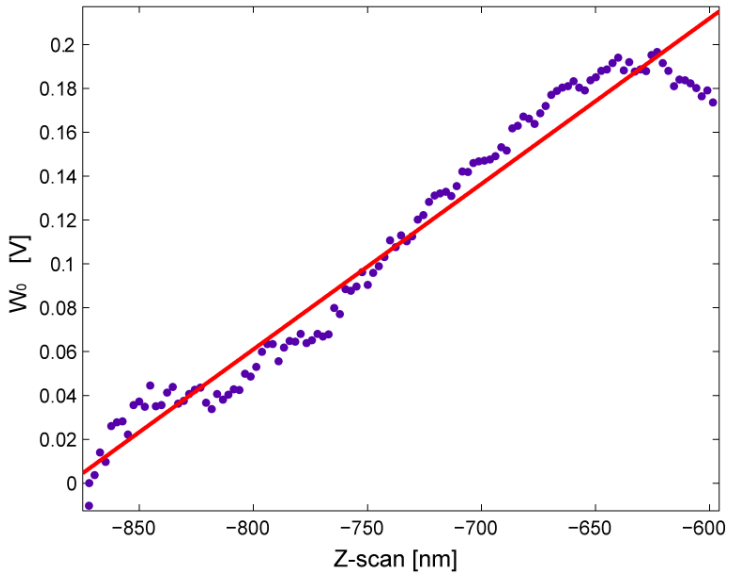

Figure 3.13 W_0 vs Z-scan plot regenerated from F-D measurements

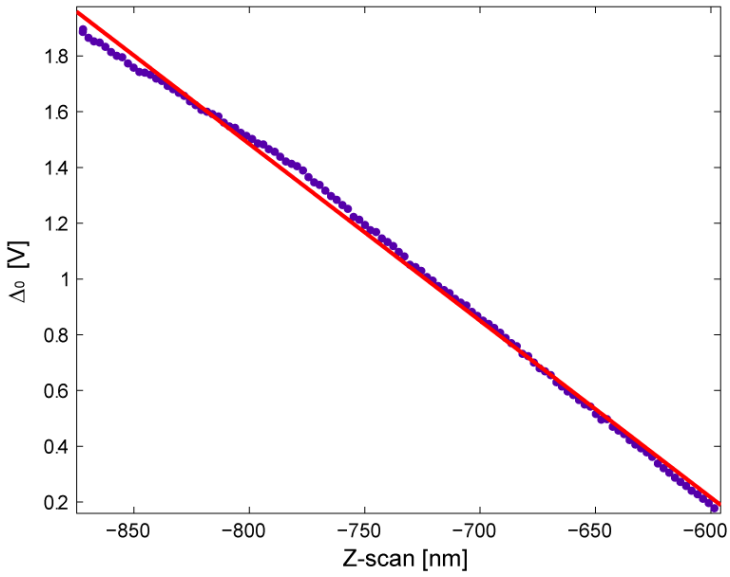

Figure 3.14 Δ_0 vs Z-scan plot regenerated from F-D measurement

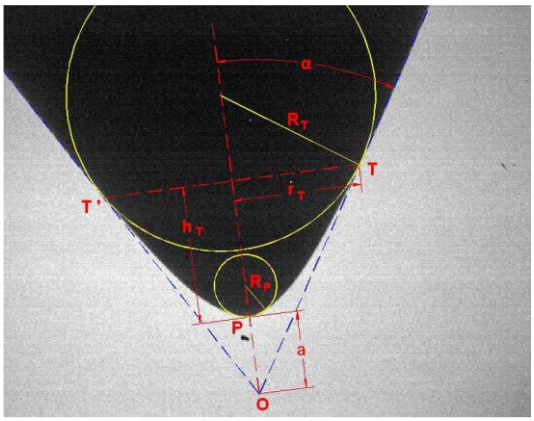

(a)

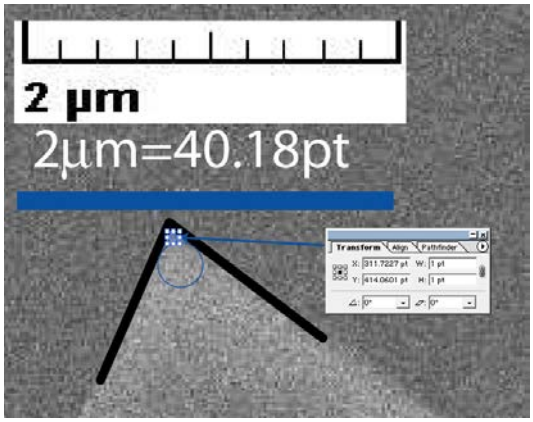

(b)

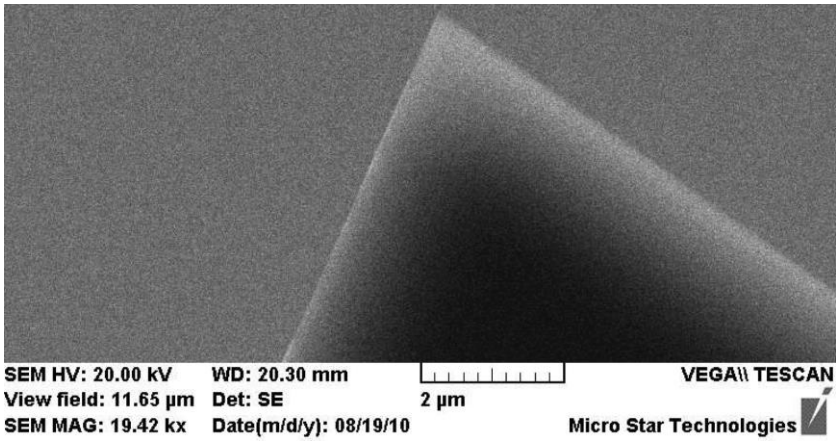

(c)

Figure 3.15 (a) Measurement process described by the manufacturer, (b) edge radius [(2000/40.18*0.5) = 24.88 ≈ 25 nm] measured from the SEM image of the original probe (c) High resolution image of the probe used in the experiment

The stiffness of the AFM probe, as provided by the manufacturer, was used in the calibration process. Therefore, two different methods were used to measure the stiffness of the AFM probe. One of the diamond probes used had a stiffness value of 146 N/m. In first method, the vertical stiffness of the probe was experimentally verified by obtaining the frequency response function (FRF). The natural frequency of the system could be identified using the FRF assuming a simple cantilever beam with a point mass. The

natural frequency was found to be 47.70 kHz, resulting in an approximate vertical stiffness of 133.3 N/m, if an ideal cantilever was assumed. The obtained FRF for the cantilever is shown in Figure 3.16.

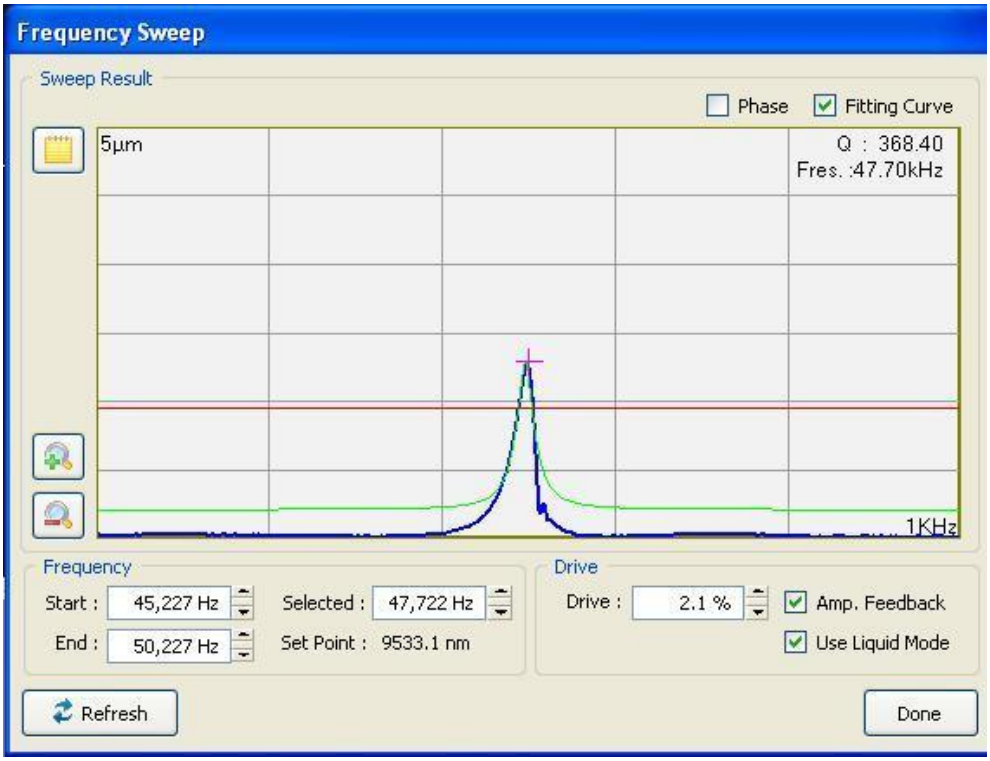

Figure 3.16 Experimental FRF for AFM probe

The difference between the experimentally obtained value and the vendor provided value (146 N/m) was approximately 8.7 %. The deviation may be attributed to the measurement of the probe mass, which is difficult to measure directly; therefore, another approach was considered for the measurement of the stiffness of the cantilever. In a previous study of the University of Calgary's Micro Engineering Dynamics and Automation Lab (MEDAL) [Mehrpouya et al., 2011]; the effects of boundary conditions

were investigated at the tool base, which were found to influence the dynamics of AFM probes.

In order to confirm those results, a commercial finite element analysis (FEA) software (ANSYS) was utilized to simulate a cantilever with a vertical stiffness of 146 N/m. The FEA result was then combined with the given boundary condition through receptance coupling (RC). When the cantilever was clamped at one end, imitating the boundary condition of the experimental setup, the resulting natural frequency was 47.99 kHz. This result was very similar to what was obtained (47.70 kHz) from experimental FRF, with an error of only 0.6% (see Figure 3.17). Therefore, the vertical stiffness value provided by the vendor is very close to the experimentally obtained stiffness value.

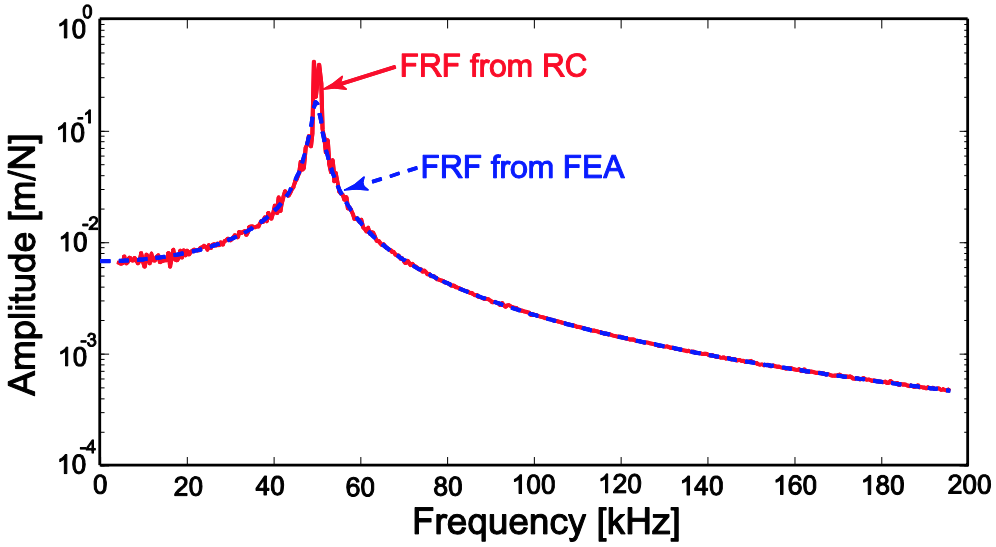

Figure 3.17 Comparison of FRF results obtained using experimental, FEA, and RC methods

The calibration methods for AFM were studied, and the force balance method was extended to investigate nano mechanical machining. The parameters involved in the calibration process were also investigated and later considered in the AFM calibration.

In nano scale, the atomic interaction between the sample surface and AFM probe can be influenced by many other nano scale phenomena such as temperature, humidity. The thermal activation and nano layers of condensed water on sample surface can influence the friction. In this thesis, the development of vibration assisted system and application of vibration assisted machining with AFM was the objective. The cutting process is performed in room temperature and room environment, therefore, the effect of temperature and humidity are not considered. The calibration method is applied to measure the cutting force, to compare the friction coefficients (ploughing, adhesion and apparent) between conventional and different vibration assisted machining. In the following chapters (4 and 5), conventional and vibration assisted machining are discussed, and different phenomena related to nano mechanical machining are compared.

3.3 Vibration Assisted Experimental Setup

Once the sensitivities of the position sensitive photo diodes (PSPD) have been calibrated with respect to the diamond probe in the lateral and vertical directions, the experimental cutting forces can be acquired. In this thesis, soda lime glass, aluminum and gold materials are studied. Chromium, Polycarbonate, Polystyrene, Photoresist and nano filler based (carbon nano fiber and carbon Nanotube) polystyrene were also studied, but the results are not included in this thesis.

The study was conducted for both scribing and vibration-assisted machining to evaluate the cutting performances on different types of material. Please note that there were several atomic force microscopy (AFM) probes used during the experiment, as the probes are fragile. However, the calibration constants are mentioned with each probe change.

In vibration assisted machining, vibration stages were installed on top of the AFM system to allow excitation of the workpiece in three axes. Figure 3.18 presents the overall difference in nano scribing and vibration assisted nano mechanical machining. In conventional nano scribing, the AFM probe indents due to the set point force; and, the material is removed as the workpiece is moved (feed motion) in the X or Y direction. On the other hand, in vibration assisted machining, the AFM probe indents due to the set point force, but the workpiece is moved in the X, Y and Z directions as the workpiece is fed in the X or Y direction. The movements in the X, Y and Z direction other than the feed motion give control over the trench depth and width.

The schematic of the vibration assisted nano mechanical machining setup is shown in Figure 3.19. In vibration assisted machining, the Z-piezo stage (PI P-888.31, Z axis actuator) was attached on top of the XY-piezo stage, which was again placed on top of the XY scanner of the AFM. The cutting forces were measured in a similar way as described for nano scribing, but the sampling rate was 100,000 Hz for Z-axis vibration and XYZ cutting as the applied frequency was 10 kHz. In XY vibration assisted cutting the sampling rate was 10,000 Hz as the applied frequency was 265 Hz.

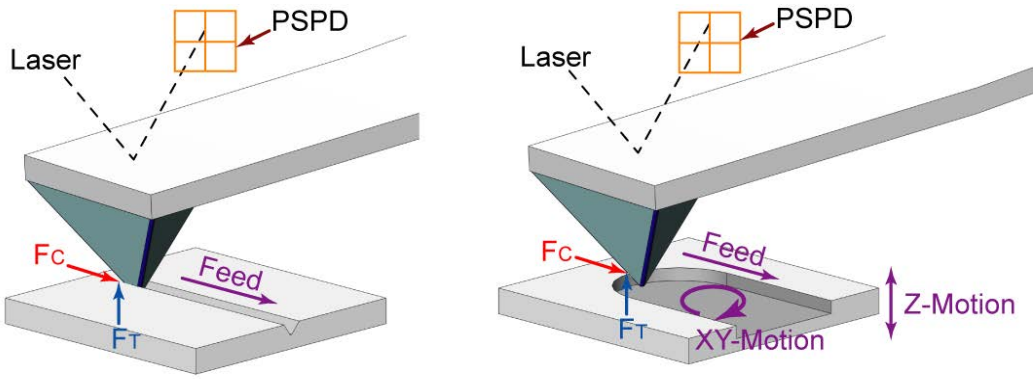

(a) (b)

Figure 3.18 (a) Conventional scratching, (b) vibration-assisted machining

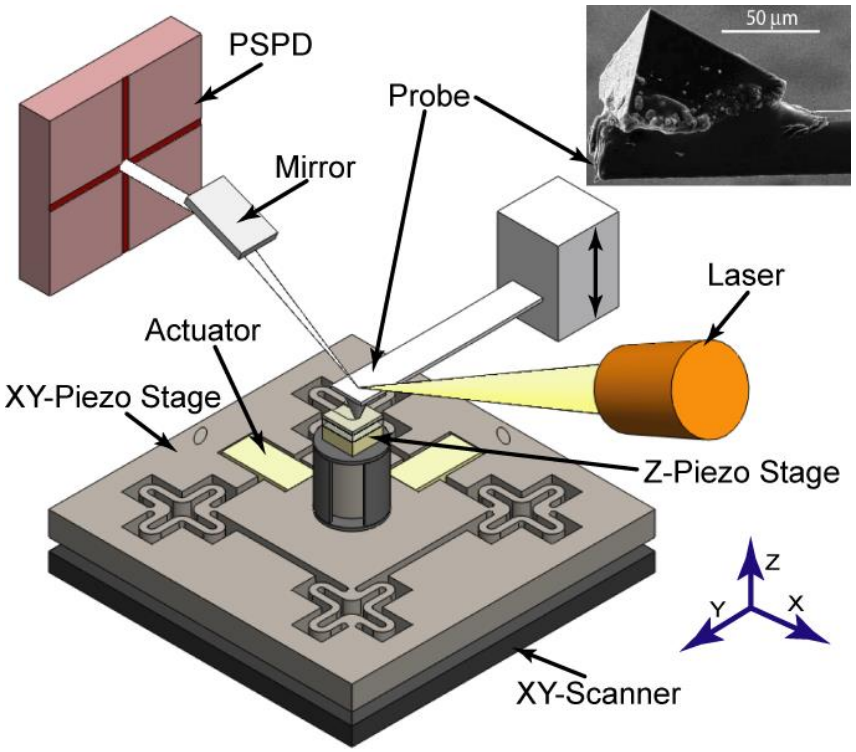

Figure 3.19 Experimental setup for vibration-assisted nano machining

The vibration assisted machining requires a XYZ piezo stage to retrofit with the existing AFM system. In the following section, an in house XYZ piezo actuating system is developed to implement the vibration assisted machining.

3.4 Design of the Nano stage

The nano stage in vibration-assisted machining is responsible for the generation of the motion according to the given signal input. The motion can be circular or elliptical, providing rotational motion to the workpiece.

The design of the nano stage was selected after the examination and testing of several designs. There were several challenges associated with the design of the nano stage, such as the space limitation between the AFM scanner and the AFM head, and crosstalk between the different axes. There was a vertical gap of approximately 20 mm between the AFM scanner and the AFM head; therefore, the stage needed to be designed thin enough to accommodate the stage, the acoustic emission sensor, the actuator for the application of the vertical displacement to the workpiece, and the workpiece itself.

There were four hinged supports connecting the main stage to the support frame of the stage. The stage was actuated via two unidirectional actuators and their motion was combined to generate a two-dimensional (2D) planar motion. An additional unidirectional actuator was placed on the 2D planar stage to provide motion in the vertical direction. Figure 3.20 shows the designed stage that can provide the 2D motion to the actuator.

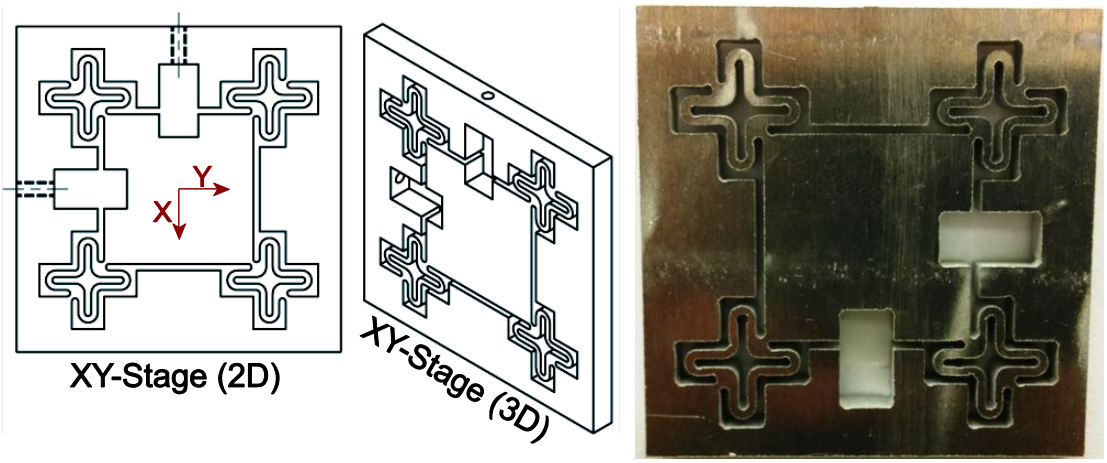

(a) (b)

Figure 3.20 (a) Schematic of the designed stage and (b) the actual stage after fabrication

In the design of the nanometer positioning stage, there were many criteria that needed to be addressed. The geometry, material and manufacturing process were of critical importance as they ultimately determined the function of the piece. These aspects were chosen with consideration of different requirements, such as machinability, range of travel of each axis, piezo size and clearances within the final assembled structure. The following paragraphs outline the design considerations for the positioning stage.

In terms of geometry, the total height of the stage was selected based on the piezo actuator size and the clearance between the AFM scanner and AFM head, which was about 25 mm. The dimensions of the piezo actuator (AE0203D08F) were 3.5 mm x 4.5 mm x 10 mm.

Many experiments incorporate an acoustic emission (AE) sensor to detect the state of the workpiece [Malekian et al., 2010]. Therefore, in the design phase, the AE

sensor holder was considered, and the Z-axis piezo actuator was placed on the AE sensor holder. There should be enough clearance to avoid collisions between the AFM probe and the sample when the AFM head is removed and the probe changed. Considering all these issues, the final thickness dimension of the designed stage was set at 5 mm. The smaller thickness of the stage has the advantage of motion control.

The piezo actuator is attached to the stage manually; therefore, there should be care in placing the two piezo actuators. To minimize crosstalk between the two primary motion axes (x and y) and the other axis (namely the vertical z-axis), both actuators should be placed in the same horizontal plane. By choosing the stage thickness to be similar to the actuator size, the task of centering each actuator with the stage becomes easier and decreases the chance of misalignment, which can eventually lead to axis crosstalk.

The geometry of the stage should also be designed in such a way that it has a symmetric shape. This helps to minimize the off axis drift present in the monolithic flexure joints. As previously mentioned, flexural supports were selected to provide controlled motion to the XY stage. The advantages of using flexures are ease of manufacture, high stiffness, absence of slick-slip and friction effects present in traditional kinematic designs and less hysteresis than rolling or sliding contacts. In addition, very little maintenance is required [Vukobratovich et al., 1988].

Aluminum was selected as the material for the stage. The reasons for choosing aluminum are its higher machinability and lower stiffness compared with steel; therefore,

it is possible to obtain higher displacements from a smaller force applied by the piezo actuators.

For manufacture, the initial plan was the fabrication of the stage using wire electric discharge machining (WEDM); however, as wire EDM was not available, abrasive water jet cutting was chosen instead. This process allows complex two-dimensional profiles to be created quickly and cheaply with a sufficient degree of accuracy.

There are a few considerations when using water jet machining. On one hand, if the thickness of the workpiece is small, the water jet causes a V-shaped taper on the final machined surface. On the other hand, if the thickness is large, the water jet feeds slower, causing a reverse taper on the opposite side. In the fabrication of the stage, an abrasive water jet machine from Omax was used, which could compensate for the taper due to its tilting nozzle head. While not perfect, the manufacturing process chosen met the design requirements laid out.

In the design phase, the stage was analyzed with the finite element method, using ANSYS software to study its dynamic behaviour. The stage was actuated during experiments with different frequencies which can excite natural frequency of the XY stage and therefore, the dynamic behaviour of XY piezo stage should be known. The finite element analysis (FEA) simulation indicated that the first mode of the natural frequency was about 2.77 kHz, as shown in Figure 3.21. The University of Calgary's Engineering Shop fabricated the nano stage using the abrasive water jet (AWJ) cutting method.

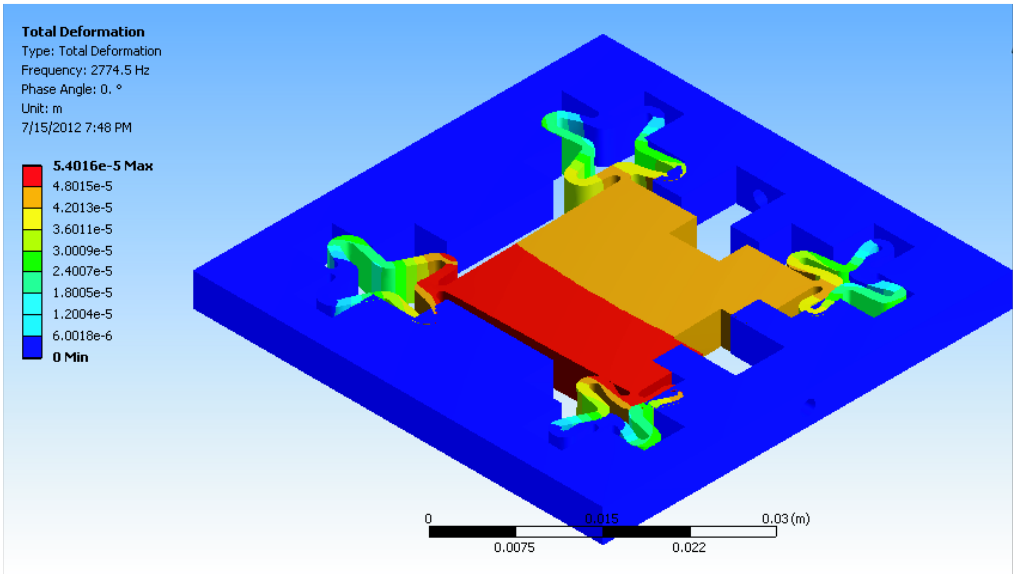

Figure 3.21 FE analysis of the 2D planar stage

The nano stage was designed and put to the test for calibration in the X, Y, and Z directions. In this study, the application input signals to the actuators were supplied from both computer and analog function generators; however, the vibration-assisted cutting phenomena were not affected which will be discussed later.

3.5 Motion Control of the Nano Stage in X, Y and Z Directions

Frequency plays an important role in the actuation of the piezo actuator. As the actuation frequency increases, the current must also increase, depending on the capacitance of the piezo actuator. Therefore, a high-speed amplifier was needed for the actuation of the piezo actuator when high-frequency applications are required. In the application of vibration-assisted machining, the 2D planar motion was kept low (265 Hz) as the speed (15900 rpm) increased corresponding to a large frequency.

Both the Z-axis vibration frequency and the piezo actuator type used for the Z axis were intentionally varied to investigate the Z-axis vibration-assisted cutting phenomena. The motion of the XYZ stage was controlled by using Labview software (version 8.2.1) and a signal generator (National Instrument PCI 6251). An analog function generator (BK Precision 4053) with arbitrary function capabilities was utilized, and a high-speed amplifier (Physik Instrumente E-501.0) was used to amplify the signal before sending the signal to the actuator.

The XY planar stage was then used to generate the motion, which was measured by a capacitance displacement sensor (Lion Precision C3-D). The measurements were then plotted against each other to see the motion generated by the designed stage. Noise and crosstalk among the different axes were also measured. Figures 3.22a and 3.22b show the input signals to the X- and Y-axis piezo actuators, and their corresponding outputs from the XY stage is shown in Figure 3.22c. The input signal (*sinusoidal function*) in the X and Y axes had a phase difference of 90°; and, the amplitude was 2.0 V (peak to peak) after the signal was amplified 10 times by the high-speed amplifier.

The outputs of the stage showed that the shape was not circular, but elliptical when the magnitudes in the X and Y axes were the same (2.0 V). This indicates that the stiffness's of the XY stages were not similar in X and Y direction. The stiffness differences may be attributed to the fabrication of the XY stage, as the AWJ fabrication method has an issue with precision [Kovacevic, 1991]. Therefore, there were stiffness differences even after making the stage symmetrical.

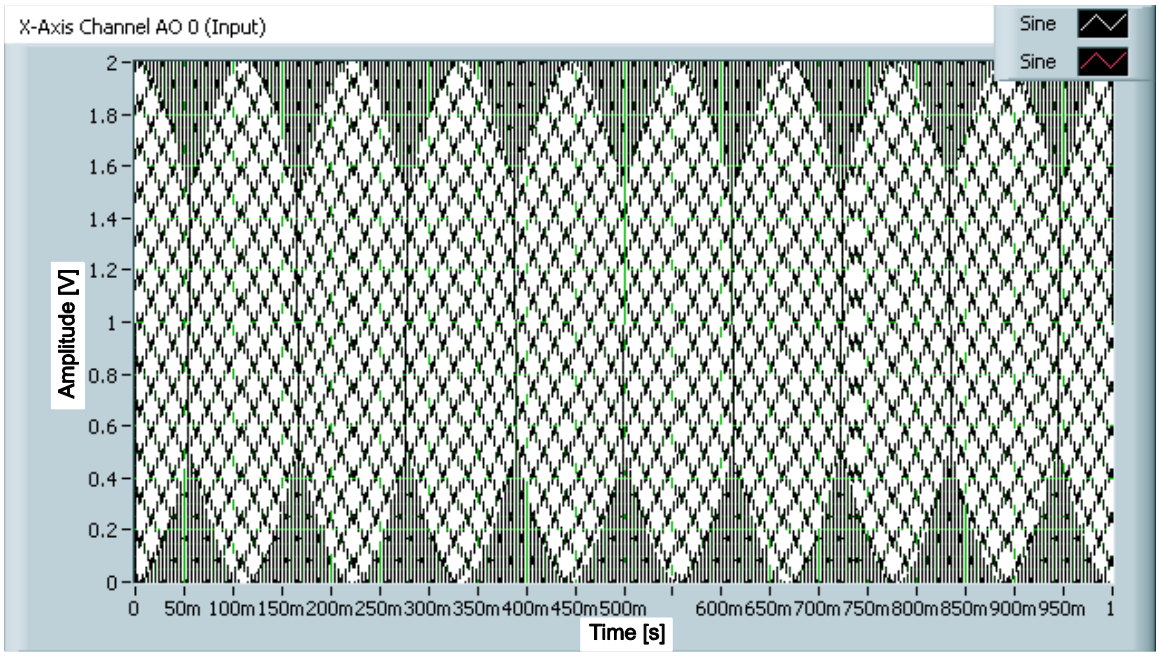
X-Axis Channel AO 0 (Input)
Sine
Sine
Amplitude [V]
2
1.8
1.6
1.4
1.2
1
0.8
0.6
0.4
0.2
0
0 50m 100m 150m 200m 250m 300m 350m 400m 450m 500m 600m 650m 700m 750m 800m 850m 900m 950m 1
Time [s]

(a)

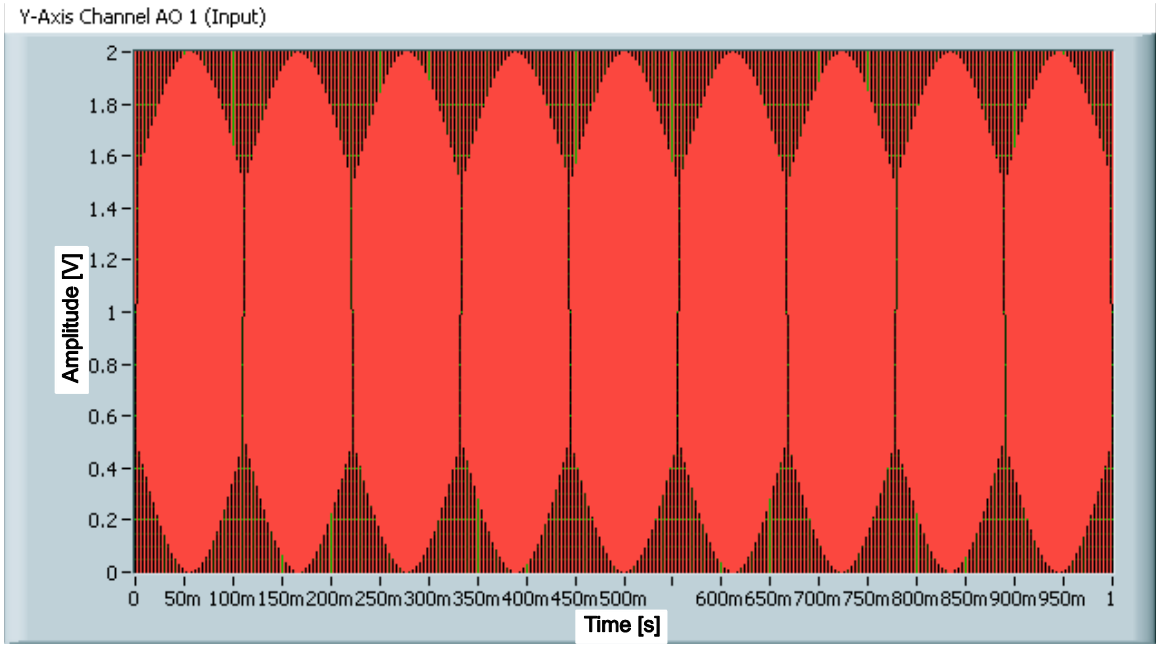
Y-Axis Channel AO 1 (Input)
Amplitude [V]
2
1.8
1.6
1.4
1.2
1
0.8
0.6
0.4
0.2
0
0 50m 100m 150m 200m 250m 300m 350m 400m 450m 500m 600m 650m 700m 750m 800m 850m 900m 950m 1
Time [s]

(b)

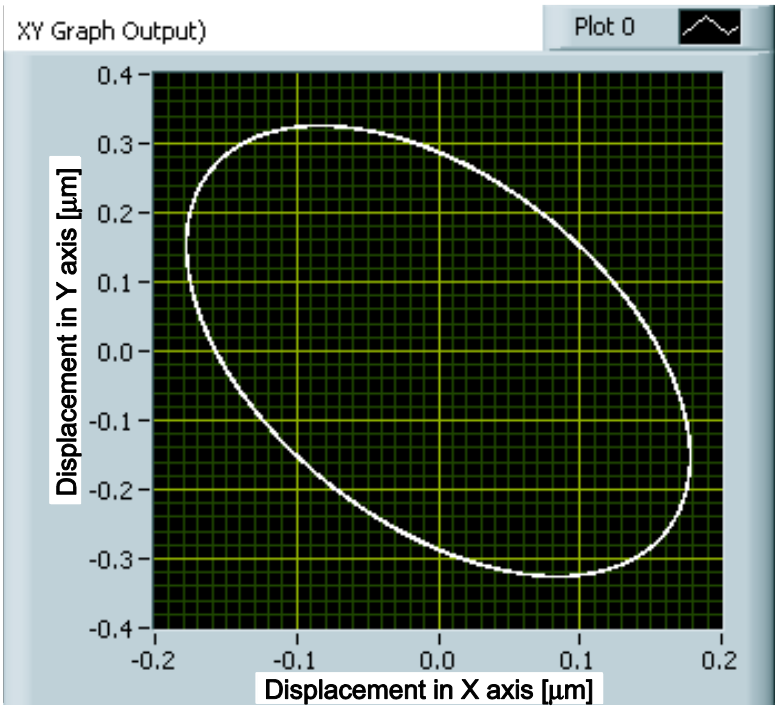

(c)

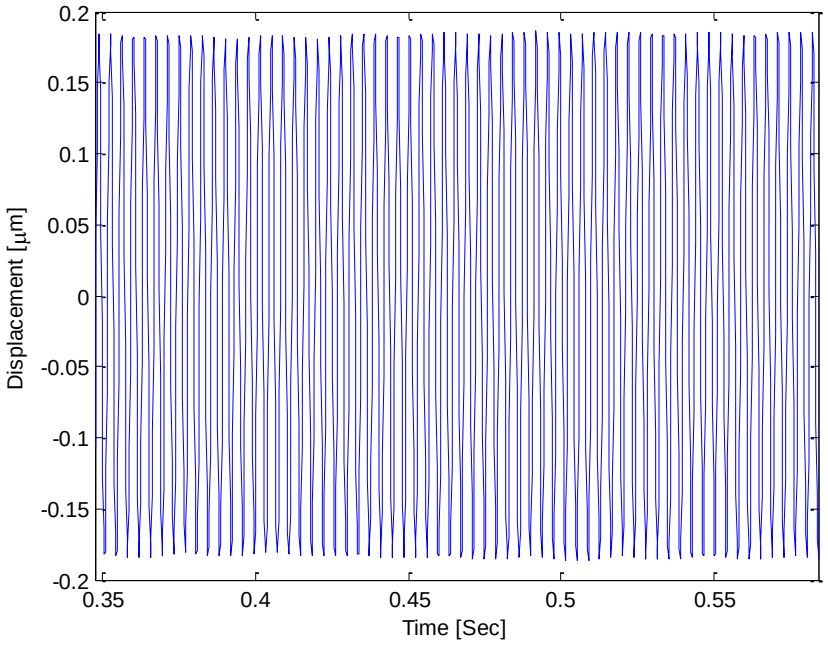

(d)

Figure 3.22 (a, b) Input signals to the XY stage, (c) shape generated by the XY stage (µm), and (d) measured displacement in the X axis

Electric discharge machining (EDM) is the common practice for the manufacture of precision stages; however, an EDM facility was not available. Therefore, the generation of a circular motion is determined through the application of different amplitudes, and similar amplitude can then be used to generate elliptical motion.

The measured shape of the stage exhibited minimal noise, as noisy output makes the plot thicker. The measured signal is shown in the X axis in Figure 3.22d. The sensitivity factors for the XY stage were 188 nm/V and 340 nm/V obtained for the X and Y directions, respectively. The displacement in the Z axis was also measured when the XY axis was actuated; and, the displacement was found to considerably less (approximately 2-3 nm, as shown in Figure 3.23) than those of the X (714 nm) and Y (1292 nm) axes. Therefore, the crosstalk was almost negligible in the Z axis when the XY axis was actuated. The displacement of the Z-stage depends on the actuator type and applied frequency. The applied frequency and relative displacement are discussed for a particular type of piezo actuator in Chapter 5.

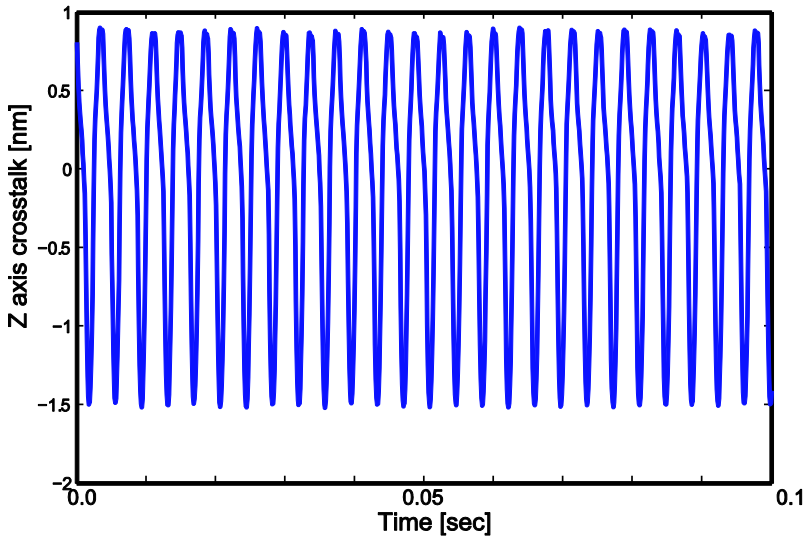

Figure 3.23 Crosstalk in the Z axis due to the applied motion in the X and Y axes.

3.6 Summary

In chapter 3, the basic operation of an atomic force microscope is described, and how to use it for scanning and basic lithography nano scribing process. The nano scribing on different material will be shown in Chapter 4 where in the developed calibration method will be implemented to measure the forces involved in atomic scale machining. The challenges in different existing calibration method to implement in nano mechanical machining has been solved by applying extended force balance method.

In addition, there are several factors that can affect the lateral calibration are considered and added to the calibration procedure. The temperature and humidity affect on the calibration method is not considered, as the temperature and humidity controlling system was not available with the current instruments. Moreover, the fabrication process was performed in a room environment from a manufacturing point of view; therefore, variation in the temperature and humidity of the room could be ignored. However, the temperature and humidity was measured during calibration and experiment and mentioned; therefore, an investigation can be carried out to study the effect of temperature and humidity on the calibration factor.

The methodology of vibration assisted machining system is described and to achieve it, a 3-axis piezo actuated stage is developed and tested. The stage was able to generate a particular shape according to the given signal. The stiffness of the XY stage in X and Y direction was not same which is due to the fabrication error of abrasive water jet cutting system. The 3-axis stage is implemented to fabricate gold sample and this portion is described in Chapter 5.

CHAPTER 4. INVESTIGATION OF NANO SCALE MACHINING BEHAVIOUR

In this chapter, the nano scribing method is investigated using the AFM probe for both brittle and ductile materials. Investigating two different materials provides elucidation of nano scale cutting mechanisms. The scribing was investigated first using a soda lime glass. In cutting of brittle material, crack formation and propagation depends on the depth of groove edge radius of the cutting tool. However, if the depth of groove is comparable to the edge radius, the brittle material can be cut in ductile mode. In the AFM probe based nano scribing method, it was possible to cut glass in the ductile mode due to the hydrostatic pressure exerted under the AFM probe which prevented crack initiations and propagations. This process can eliminate the chemical etching method and to reduce the chemical foot print.

The nano scribing method is applied to investigate sputtered aluminum. Since the operating conditions of AFM machining was in a regular air environment, a thin layer of oxide forms on the sputtered aluminum. The material removal behaviour of ductile material is investigated and a friction model developed to compare the experimental friction. It was observed that, the friction phenomena works in a different way for brittle and ductile material. The study of ductile and brittle material will enrich the level of understanding for nano scale material removal.

4.1 Scribing on Soda Lime Glass

Soda lime glass is a brittle material. The cutting of ductile and brittle materials is quite different. In ductile cutting, ploughing and shearing depend on the edge radius of the tool and the depth of groove. Shearing occurs in ductile materials when the depth of groove is higher than a certain value, which is called the minimum uncut chip thickness (MUCT). In the machining of brittle materials, there is another depth of groove after which ductile cutting becomes brittle cutting; this depth of groove is referred to as the critical uncut chip thickness (CUCT).

Ductile cutting of brittle materials is the process of machining these materials at certain cutting conditions that allow plastic deformation of the workpiece material and leave a crack free surface [Ngoi et al., 2000]. Lawn [1979] investigated an uncut chip thickness (h) at which brittle material failure during indentation changed from plastic deformation to fracture and called it the critical depth of groove (h_C).

It was later confirmed that the brittle materials have this transition in deformation regime from brittle to ductile as the depth of groove decreases [Bifano et al., 1991]. The transition from a brittle to ductile regime of cutting is described based on the balance between the surface energy and the strain energy. It has been suggested that such a transition in the deformation regime occurs because the energy needed for plastic deformation of a brittle material is less than the energy required for the propagation of preexisting cracks at small-scale cutting geometries [Puttik, 1980].

There are a few hypotheses describing ductile cutting of brittle materials. One of the theories states that the ductile cutting is a function of the density of

defects/dislocations in the workpiece material and therefore the size of the stress field. The size of stress field depends on the size of uncut chip thickness as depicted in Figure 4.1. A smaller chip thickness results in the smaller stress field containing fewer defects and produces less cracks compared to the larger depth of groove; so cutting occurs at the ductile regime and avoids propagation of cracks by avoiding cleavage initiation at the defects in the workpiece [Nakasuji et al., 1990].

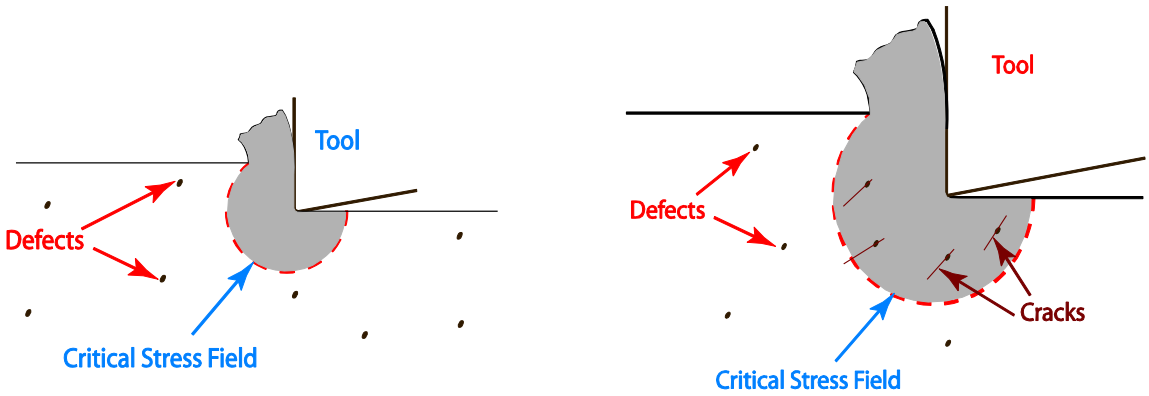

(a) (b)

Figure 4.1 Stress field around the tip of the tool (a) small depth of groove (b) large depth of groove [Nakasuji et al., 1990]

Ductile to brittle transition has been shown to be a function of parameters such as cutting speed and the geometry of the tool [Blake, 1990]. A large negative rake angle is more favorable since high hydrostatic pressure is exerted on the glass to minimize crack initiations [Uddin et al., 2004]. Figure 4.2 shows the distribution of hydrostatic pressure around the cutting edge when the edge radius re is comparable to uncut chip thickness h, resulting in the negative effective rake angle α_e. The elastic recovery, h_{er} may occur depending on the elastic nature of workpiece. In addition, brittle materials at higher

temperature also promote ductile cutting [Sreejith et al., 2001], which can be explained by higher fracture toughness at increased temperatures.

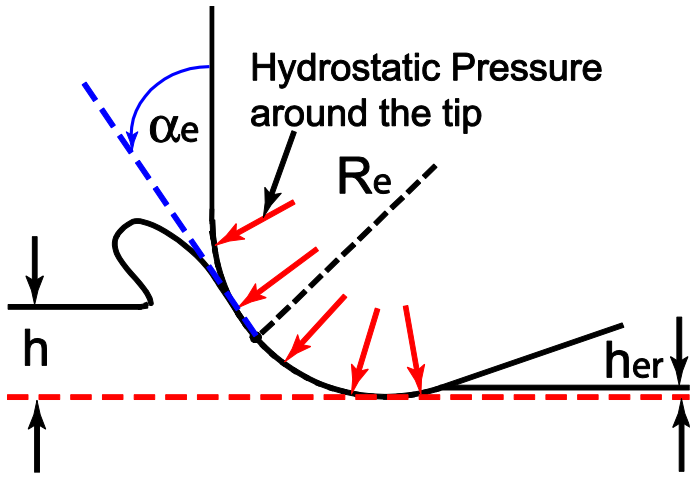

Figure 4.2 Hydrostatic pressure around the cutting tip

With the increase in depth of engagement between the tool and the workpiece, the interaction between the tool tip and the workpiece is considered in several phases as shown in Figure 4.3. In the first stage, the forces between the tool tip and the surface causes adhesion friction and the surface deformation occurs in the elastic regime. In the second phase (ploughing), the tool starts to deform the workpiece material plastically. As the engagement depth is increased further, the tool starts to cut the workpiece and chip formation starts. The transitional depth between the ploughing and shearing cutting regime is denoted as the MUCT. In the ductile regime or after exceeding the MUCT, the material is removed as a continuous chip and the finished surface contains fewer flaws. In the case of brittle material, cracks can initiate and cause decrease in forces; yet, the discontinuous chips occur due to the brittle nature of cutting and causes cloudy surface finish which is covered by residual cracks [Nakasuji et el., 1990].

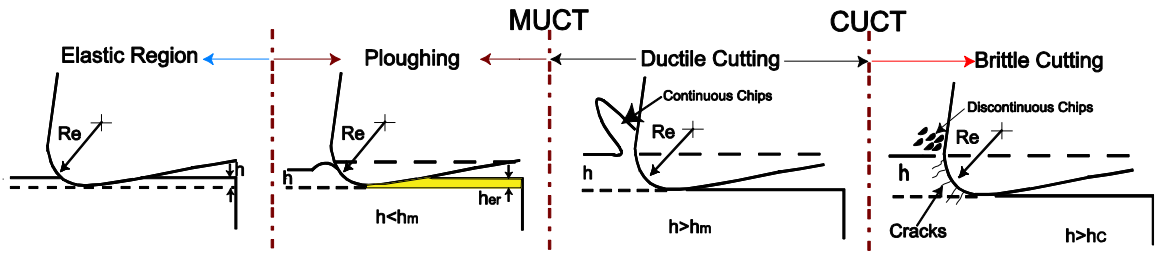

Figure 4.3 Different cutting regime of brittle material depending on the uncut chip thickness

The AFM probe was calibrated before scribing soda lime glass, however, this study was performed before the detailed investigations of the various affecting parameters and the lateral forces will be smaller what is reported in this thesis. The vertical sensitivity was 5.28e-8 m/V and the lateral calibration factor was found to be 3.136e-5 N/V. The recorded room temperature and humidity during calibration and experiment was 22°C and 9% respectively. The objective was to perform the ductile cutting of brittle material and to find the MUCT and CUCT.

The experimental conditions selected are shown in Table 4.1. Two different types of load (constant and ramp) was selected. The ramp type load was selected to find the transition between ductile and brittle cutting. The maximum load was possible to apply was 70 μN, however, the maximum applied load was limited to 60 μN for the safety of the probe.

Table 4.1 Experimental conditions for scribing test on soda lime glass

Scratch No.	Type of Force	Thrust Force
1	Constant Force	30 μN
2	Constant Force	40 μN
3	Constant Force	50 μN
4	Constant Force	60 μN
5	Ramp Force	0-50 μN
6	Ramp Force	0-60 μN

Forces can provide a plethora of information for machining operations. The interpretation of the forces, in terms of the dominant cutting regimes in the scratching process, requires an understanding of the deformation mechanisms in the ploughing, shearing and brittle cracking regimes. Figure 4.4 depicts the measured cutting and thrust forces and AE signals. Since the probe was set to the contact scanning mode before it started working at the lithographic mode, it experienced a contact mode set point force (~500 nN) before beginning the scratching process. When the process started, the stage brought the probe's tip to a new set point, which had been defined in the lithographic mode as 0 N; and, the stage moved to the starting point of the scratch. The scratching then began, and the tip went back to the set point value of the lithographic mode.

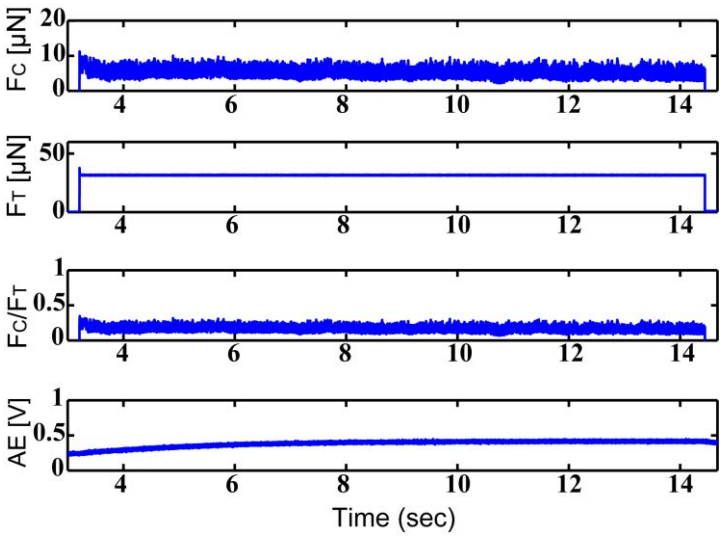

(a) 30 μN at 1.0 μm/s

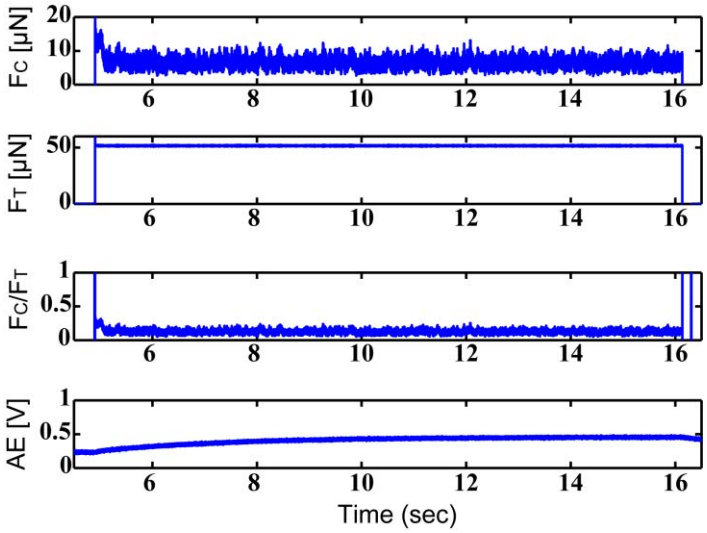

(b) 50 μN at 1.0 μm/s

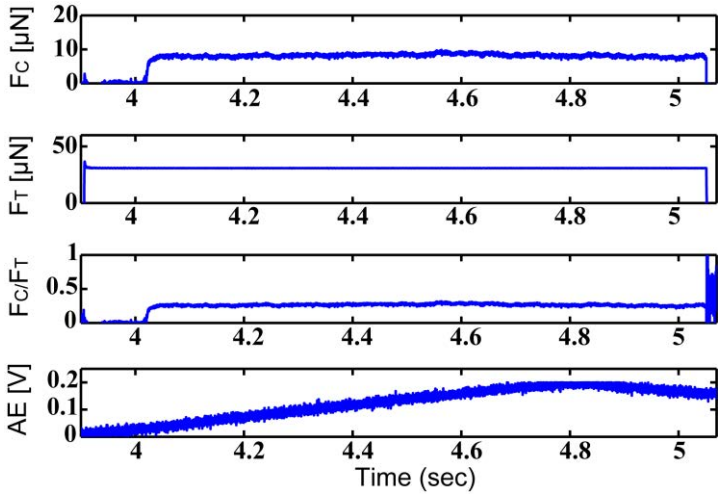

(c) 30 μN at 5.0 μm/s

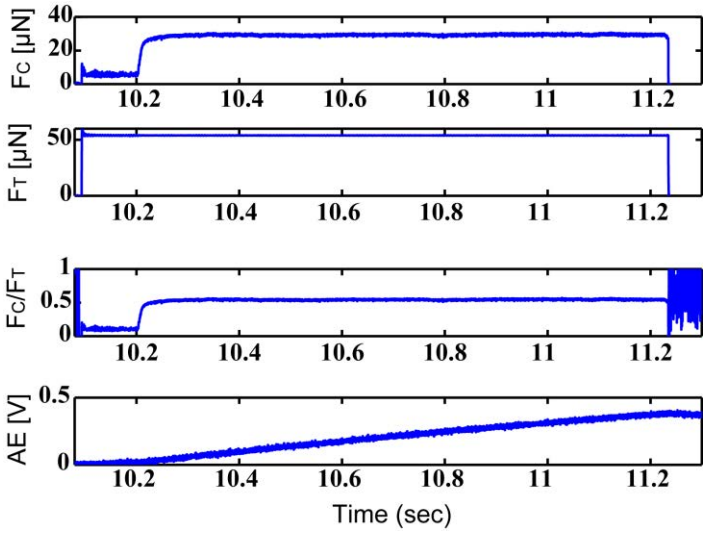

(d) 50 μN at 5.0 μm/s

Figure 4.4 Scratching forces corresponding to constant thrust forces

In Figure 4.4, the cutting force (F_C), thrust force (F_T), apparent friction coefficient ($\mu = F_C/F_T$) and unfiltered AE voltage signals are plotted for the applied constant thrust forces of 30 and 50 μN at 1.0 μm/s and 5.0 μm/s. The cutting force was constant for a

constant applied force; and, the AE signal was measured. At the end of the cutting, the AE signal was observed to be decreasing very slowly, which was due to the drift of the sensor [Malekian et al., 2010].

In the authors' micro scratching test investigations using a conical indenter (R_e of 15 μm) on the sloped soda-lime glass [Sajjadi et al., 2009], it was found that, the apparent friction coefficient value to be approximately 0.5 in the ductile cutting regime and the micro scratching by using conical tool is shown in Figure 4.5.

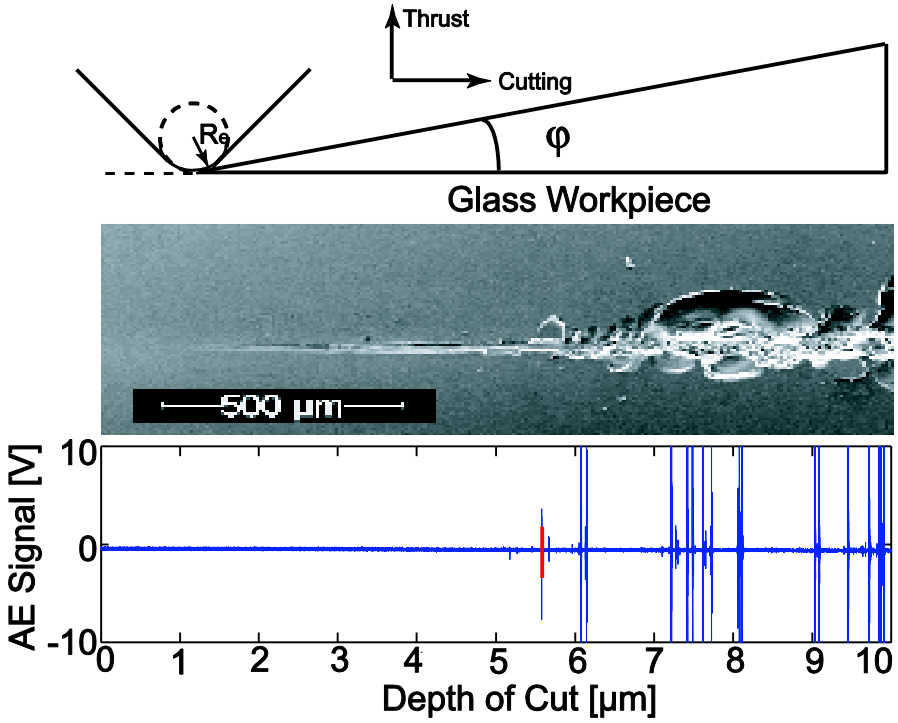

Figure 4.5 Ductile to brittle transition of soda lime glass in micro scratching [Sajjadi et al., 2009]

However, in the AFM scratching test, the friction coefficient was found to be smaller than that of the micro scale. The average friction coefficient was determined to be

approximately 0.15 for both 30 and 50μN forces at 1.0 μm/s. The variation of load at the lower feed rate did not change the friction coefficient, unlike the findings of [Ahn et al., 2009], who had found that, if the depth of groove was varied, then the friction coefficient also varied. However, the friction coefficient varied when the feed rate was increased; and, the apparent friction coefficient was found to be approximately 0.26 for a 30 μN thrust force and 0.5 for a 50 μN thrust forces at 5.0 μm/s. At a higher feed rate, the friction coefficient increased with the increase in applied load and a small amount of slippage may happen [Figures 4.4c and 4.4d] at the very beginning of cutting at higher feed rate. The friction coefficient increased when the feed rate increased. Tambe et al. [2004, 2005] investigated the effect of velocity on the deformation friction coefficient using the AFM probe and found the similar trend.

The AE sensor was used to determine whether cracks propagated; and, in micro-scale scratching, it was possible to observe a sudden jump in the voltage from the AE sensor when a crack propagated as illustrated in Figure 4.5 [Sajjadi et al., 2009]. However, in the nano-scale scratching tests, where the scratching conditions are depicted in Table 4.1, the AE signals did not show any sudden jump or burst. From these observations, it was assumed that, the scratch tests were predominantly performed in the ploughing and ductile cutting regimes.

Figure 4.6a illustrates the topography of the machined groove and the depth of penetrations, reflecting the force applied for scratching. The cross section of the scratches shows the amount of the piled-up material on both sides of the trench for both the feed rates of 1.0 and 5.0 μm/s. The height of the piled-up material also varied, depending on the amount of applied force. The depth of groove increased with increases in applied

force, resulting in more material pushed to the side of the trench. The pileup heights for different feed rates did not vary significantly as shown in Figure 4.6b, despite the fact that different friction coefficients were observed.

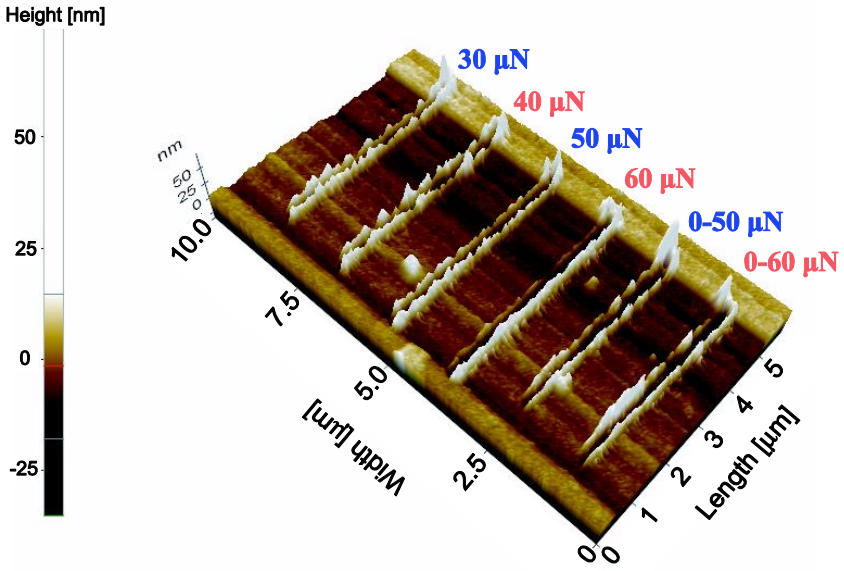

(a) Topographical view of scratches at 1.0 µm/s

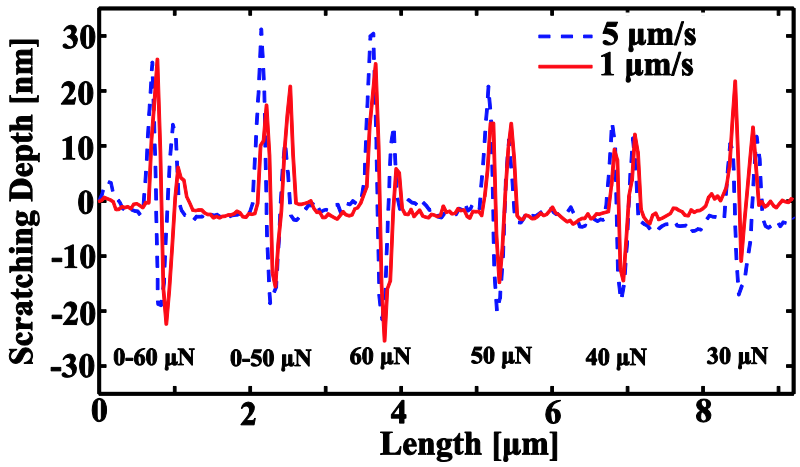

(b) Cross sections of scratches

Figure 4.6 (a) Topographical view of the scratches and (b) scratch depths with pileup heights at corresponding loads

4.1.1 Investigation of Minimum Uncut Chip Thickness (MUCT)

To investigate the regime of deformation in the scratching process, it has been suggested by [Ahn et al., 2009] that the ratio of the pileup height to the scratching depth needs to be examined. In nano-scale scribing, comparative size of pileup in respect to depth of the groove is found to be representative of the cutting regime; where in ploughing dominant scratching the ratio of pileup height over groove depth is much higher than that of shearing dominant scratching. The vertical line perpendicular to scratch line was used to measure the scratching depth or depth of groove, h, and the average pileup height, h_p, as the average of the pileup on both sides of the groove, h_1 and h_2 are the pileup height beside the trench, i.e. $h_p = (h_1+h_2)/2$. The scratching depth and heights were measured using the scanned surfaces from the ultra sharp probe (edge radius < 10 nm).

In the ploughing regime ($h_p/h > 1$), because no chip was formed, all the deformation occurred as the removed materials piled up on both sides of the groove. Hence, it is expected that there will be a higher ratio in the ploughing regime than in the shearing dominant zone. In the shearing regime ($h_p/h < 1$), the material is removed as chips so less amount of pileup occurs and the average pileup should be less than the scratching cut. Figure 4.7 depicts how the scratching depth and pileup heights were defined on the cross-sectional view of a scratch. The pile up area A1, A2 and A3 is calculated to identify the ploughing shearing phenomena according to molecular dynamic simulation suggested by Yan [2006].

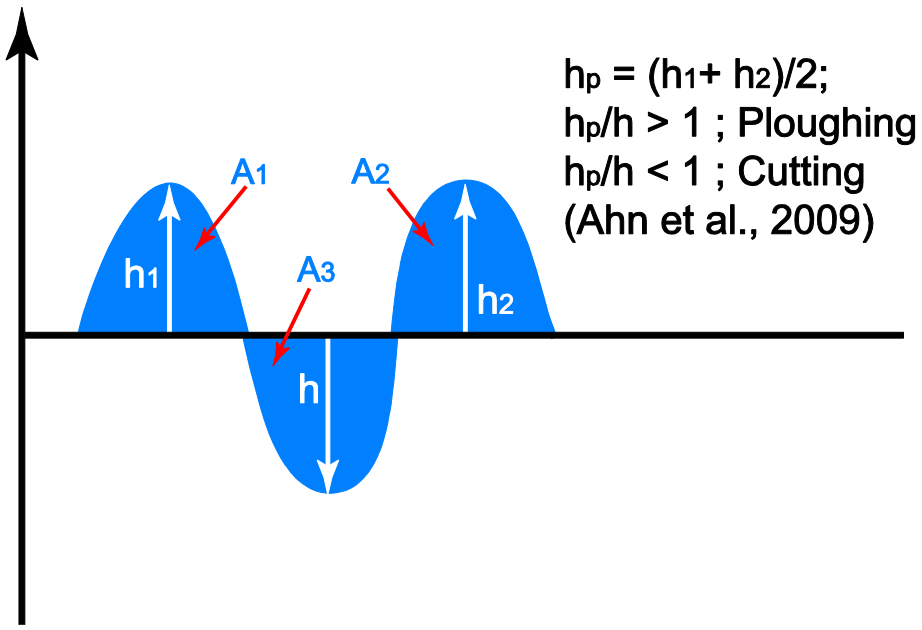

Figure 4.7 Cross-sectional view of the trench with pileup heights

Figure 4.8 was obtained by finding the pileup ratios for different forces and feed rates. There were few points below the ratio of 1.0. This may be due to chip formations and preexisting surface defects, such as roughness and waviness caused by nonuniform deposition and internal stress. The repeatability of this experiment was good, because, at least 6 sets of experiments were conducted; and, in every case, similar trends were found. The MUCT was found to be 13-14.5 nm (gray areas in Figure 4.8) regardless to the different feed rates, except for the 0-50 μN ramp force, which may be due to the irregularities on the surface and measurement error in spite of having high accuracy AFM system [Khurshudov et al., 1997]. The transition between the ploughing to shearing regime was not sharp, since the sample surface was not optically flat and the reference points to measure h, h_1 and h_2 were different for each feed rate due to the surface roughness.

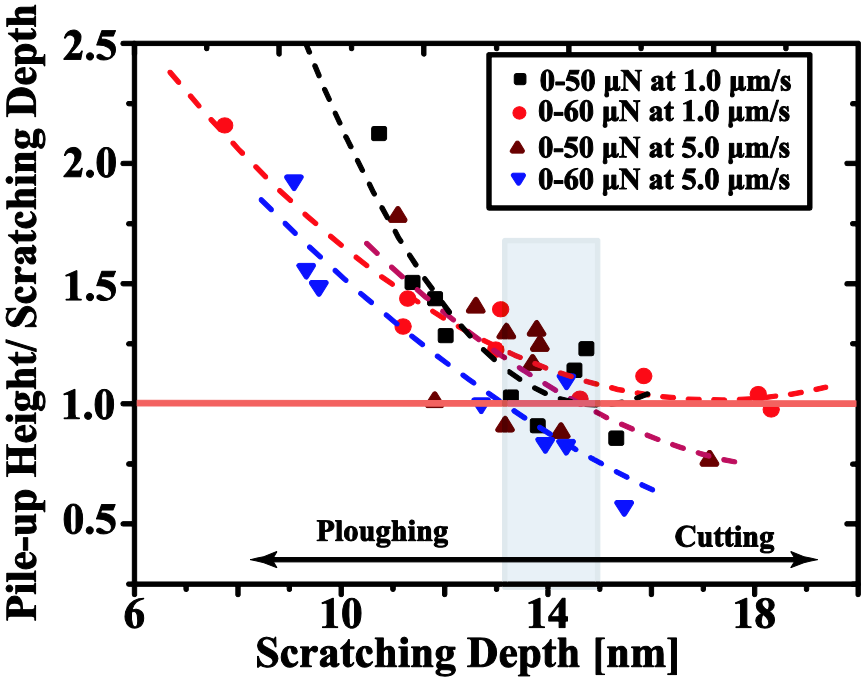

Figure 4.8 Ratio of pileup heights over scratching depth vs. scratching depth plot

Another approach based on Yan [2006] was used to investigate the ductile cutting phenomena. According to Yan [2006], molecular dynamics (MD) simulations for monocrystaline copper, there is a relationship between the trench made and the material removed in terms of area, not by pileup height. In this study, the areas for 'A_1', 'A_2' and 'A_3' shown in Figure 4.9 were calculated; however, calculations indicated that 'A_1+A_2' was usually higher than 'A_3'. According to Yan [2006], this phenomenon is due to pure ploughing. Figure 4.9 shows the calculated areas at a certain cross section. Compared to pileup height ratios, the area ratio is still uncertain from an experimental point of view, due to difficulties in acquiring accurate areas and to the front pileup effects, which are difficult to account for in the two-dimensional (2D) analysis.

The AFM measurement has a drawback in measuring overhanging structures, such as burrs. As the AFM probe measures the overhanging burrs, the AFM probe does not consider undercut (i.e. the empty space below the burr); therefore, the image generated is a solid area, which exaggerates the measurement of real area. However, in MD simulation, the real cross section can be measured. Moreover, the MD simulation was performed on crystalline material where as glass is an amorphous material and for this reason the results could be different but more investigations are required.

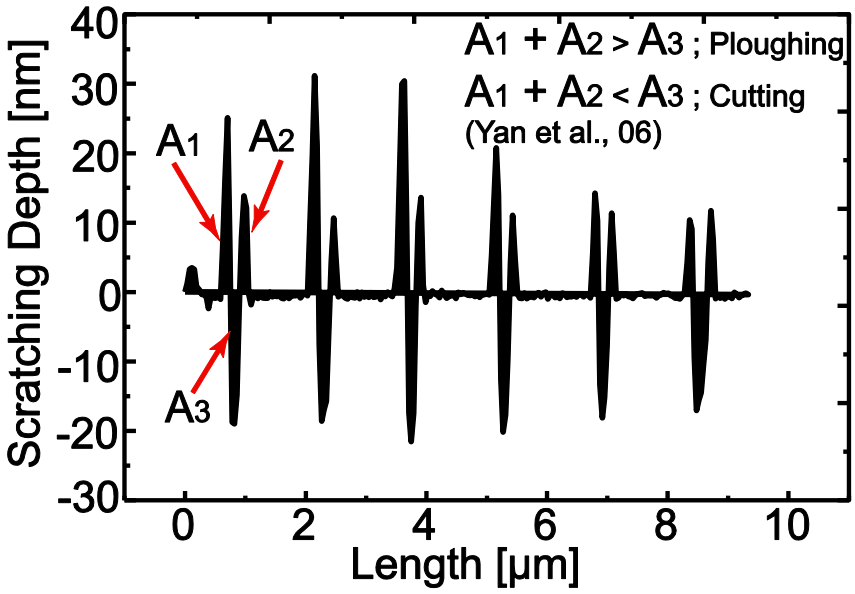

Figure 4.9 Piled-up areas (front view) 1.0 µm/s

4.1.2 Investigation of Depth of Grooves

The effects of feed rate and thrust forces have significant influences on the depth of groove in the nano-scale. The depth of groove variation (at least six point measurements were performed and the average value of the depth is considered), depending on different feed rates and constant applied forces, were analyzed and is

shown in Figure 4.10 with error bars in the measurement. Malekian et al. [2010] found variations in scratching depths and scratch quality of the machined surface depends on the feed rates, when they machined chromium material with the AFM and compared the side view. For nano-scale scratching of glass, the scratching depth varied with the varying feed rates, and this investigation has shown similar results with the authors' previous study.

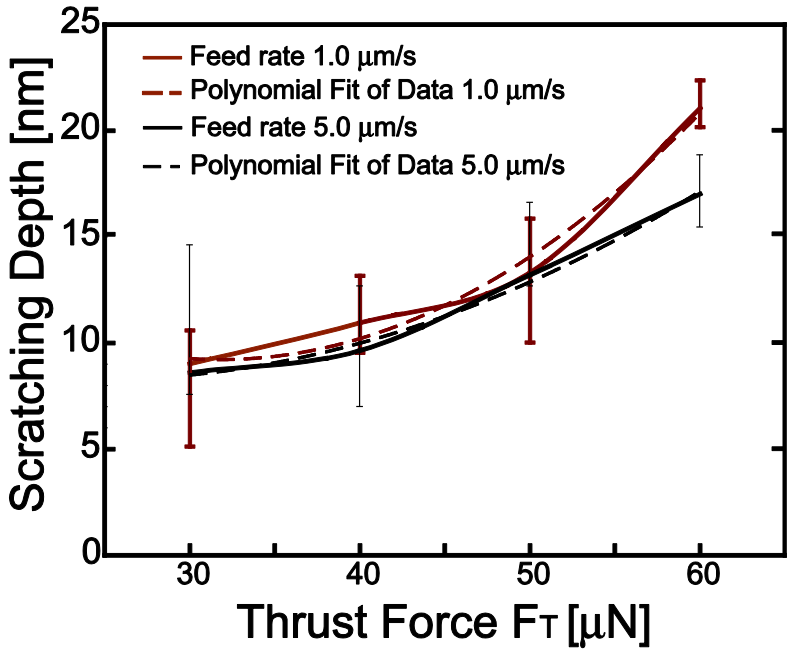

Figure 4.10 Scratching depth of groove with variation in the thrust force and feed rate

As illustrated in Figure 4.4, the feed rates have a significant effect on friction, and this may be attributed to different depths for different feed rates. Therefore, the feedback servo system may also be affected, especially at high feed rates. The depths at different feed rates with respect to the applied thrust force (F_T is in µN and scratching depth 'h' is in nm) plot was curve fitted by polynomial interpolation shown in Equation 4.1:

$$h(F_T) \approx 23.94 + 0.93F_T - 0.015F_T^2; \ (Feed\ rate\ 1.0\ \mu m/s)$$
$$h(F_T) \approx 12.31 + 0.34F_T + 0.007F_T^2; \ (Feed\ rate\ 5.0\ \mu m/s) \quad 4.1$$

This relationship shown in Equation 4.1 describes the relationship between the feed rates, thrust force and depth of groove. This relationship predict the possible depth of groove if these three factors are considered for soda lime glass.

The coefficient of determination, the R^2 value, for the equation is calculated to be 0.97. The polynomial interpolation method is used as it provided higher coefficient of determination and while the curve fitting equation is evaluated it provided minimal deviation (1-2 nm) from the real measurement. Moreover, it was observed that, the relationship is non-linear in nature, and if higher force is applied, the nominal rake angle will influence the scratching process instead of effective rake angle (which result in the negative rake angle).

Ductile cutting of brittle material is possible in the AFM scribing method; and, the measurement of the MUCT, cutting forces, effect of feed rates and thrust forces are investigated. In vibration-assisted cutting, the chip thickness is smaller due to the pulsating cutting; therefore, ductile cutting of brittle material is more efficient in terms of the obtained depth of groove and tool wear [Moriwaki et al., 1992].

In this section the ductile nature of a brittle material is studied by AFM. The brittle material can be fabricated in a ductile mode with AFM without having any brittle fracture which can reduce the use of chemical etching process and the environmental foot prints. The effect of feed rates on friction and thrust force, depth identification will help to understand the nano scale machining behaviour of other ductile and brittle material. In

the next section, nano scribing of aluminum is performed to understand the nano scale friction and depth identification model is developed based on our previous study [Malekian et al., 2010].

4.2 Scribing on Aluminum

Aluminum is widely used due to its excellent machinability characteristics. Therefore, a sputtered aluminum workpiece was prepared using the physical vapor deposition (PVD) technique, where pure (99.9999%) aluminum was deposited at a thickness of approximately 500 μm on a silicon substrate. The surface roughness of the workpiece was measured to be approximately 4.0 nm. The AFM probe used for this experiment had a vertical sensitivity of 5.281×10-8 m/V and a lateral calibration factor of 3.1363e -5 N/V. The room temperature and humidity measured during calibration and experiments were 21°C and 11%, respectively.

In this study, several sets of tests are performed at three different feed rates. Both constant and ramp forces were applied. The experimental conditions for machining aluminum are shown in Table 4.2.

Table 4.2 Experimental conditions applied on aluminum sample

Feed Rates (μm/s)	*Force (N)*
0.5	10, 12, 14, 16 and 0-16
1.0	10, 12, 14, 16 and 0-16
5.0	10, 12, 14, 16 and 0-16

4.2.1 Force Analysis

As the probe was dragged along the surface, the workpiece material was either compressed or ploughed. Figure 4.11 shows the experimental cutting and thrust forces due to increasing ramp forces, the apparent friction factor (i.e. F_C/F_T) and the AE signals during a scratch at a feed rate of 5.0 μm/s. The thrust force (F_T) was increased linearly from 0 to 16 μN; and, the cutting force (F_C) was observed to increase almost linearly as the thrust force increased, but had some fluctuations that may have been caused by additional vibrations in the cantilever due to the control feedback loop. Therefore, low-pass filters (i.e. second-order Butterworth with a cutoff frequency of 4.0 kHz) were applied to the force measurements to reduce fluctuations in force due to ambient noise. The AE signals increased and could be correlated to the resultant forces. Based on this observation, an AE sensor can be effectively employed to monitor the plastic deformation of the workpiece material.

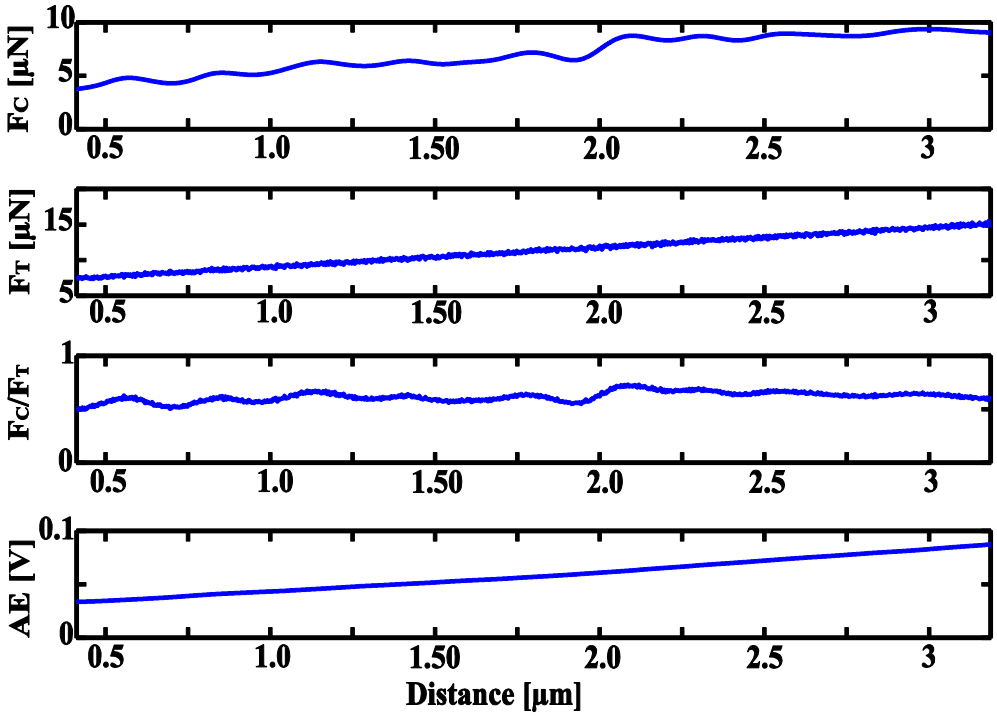

Figure 4.11 Ramp force and AE measurements at 5.0 μm/s

4.2.2 Topography Analysis

The surface profiles of the scribed workpiece were acquired using an ultra sharp probe to scan in the non-contact mode. Figure 4.12a illustrates the three-dimensional AFM scanned image of the scribed surfaces produced at a feed rate of 5.0 μm/s. The front view (Figure 4.12b) at five different thrust force settings are also depicted.

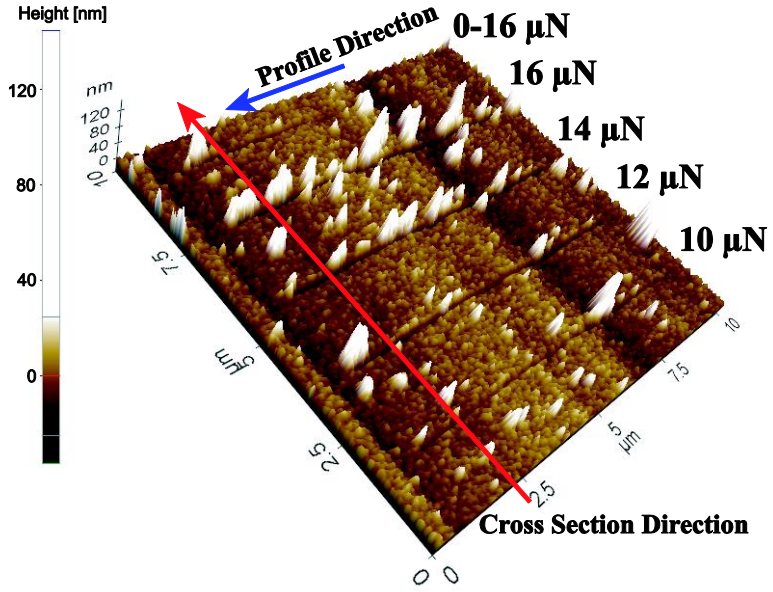

(a)

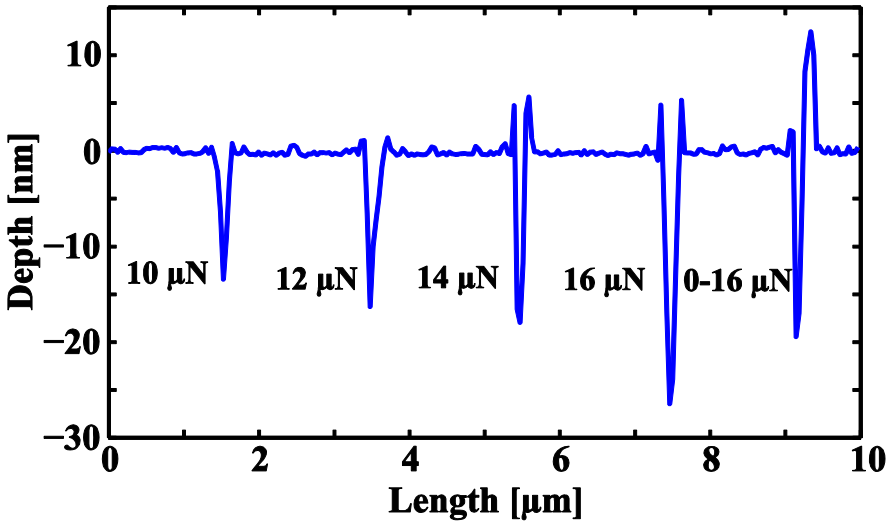

(b)

Figure 4.12 (a) AFM scanned surface, and (b) front profiles in the cross-sectional direction at different thrust forces

Side pileup is an important parameter to be analyzed in mechanical machining, because it reflects the behaviour of many cutting parameters. Moreover, when cutting a

channel, side pileup is not acceptable. When there is no pileup, it has been observed that some materials are accumulated at the end of the cut trench, which is called residual debris. In making a channel, the aspect ratio, trench width and trench depth are also very important parameter to observe.

It can be observed from Figures 4.12a and 4.12b that pileup is influenced by both the applied thrust force and the feed rate. Very small side piling effects were observed for constant thrust forces of 10 and 12 μN; however, greater side pilings were observed for higher cutting forces.

It was also investigated the effects of the feed rate on the depths and pilings. It was observed that, feed rates had a minimal effect on the trench depths, which was slightly higher (by 3%) at 0.5 μm/s compared to 5.0 μm/s for similar magnitudes of forces. At lower feed rates, it was found that, the side pilings to be greater than at the higher feed rates. A similar observation was reported by Biswas [1997], where higher feed rates contributed to higher temperatures, minimizing side pilings. Figure 4.13 shows trenches that were cut at the different feed rates and cutting forces previously described.

The probe tip shape (i.e. orientation of the probe tip) also influences the piling up of material; however, the cutting forces for all those directions are difficult to obtain. Another investigation to identify this phenomenon was performed. Four trenches were cut by different sides of the probe tip, as shown in Figure 4.14a, at a force of 20 μN and a feed rate of 1.0 μm/s. (The yellow arrow shows the machining directions and the blue marking on the probe show the probe surface involved in machining.) A very small amount of piled-up material was found when the trench was cut by side 1 (arrow showing

downward) and side 2 (arrow showing upward), but the amount of residual debris was higher for side 1. The cutting forces were also difficult to obtain for the directions of both sides 1 and 2.

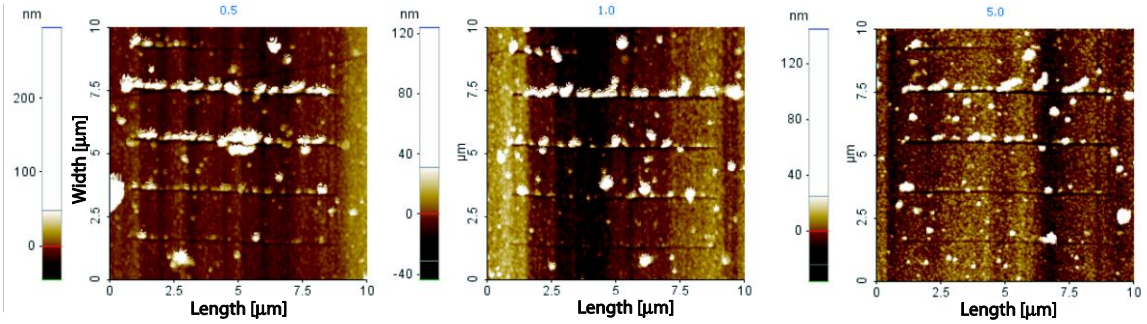

Figure 4.13 Topography of trenches cut in 0.5 µm/s (left), 1.0 µm/s (middle) and 5.0 µm/s (right)

It was observed that the depth also varied, depending on the probe shape in Figure 4.14a. It is important to observe how the channel quality changes with the shape of the probe tip, particularly when a complex channel is necessary, because the timing of the different sides of the probe tip will have an impact on the machining.

The applicable cutting force depends on the cantilever stiffness, and the stiffness of the cantilever depends on the material properties of the cantilever. A high stiffness cantilever is very expensive. To overcome this situation, multiple (8 times) pass cutting was applied, and the topography is shown in Figure 4.14b, where a force of 10 µN was applied, and the trench was machined from left to right. The result shows a significant pile (60.86 nm) of material, but the trench had a comparatively deeper depth of groove (121.28 nm), which can be compared to the depth and pileup value shown in Figure 4.12.

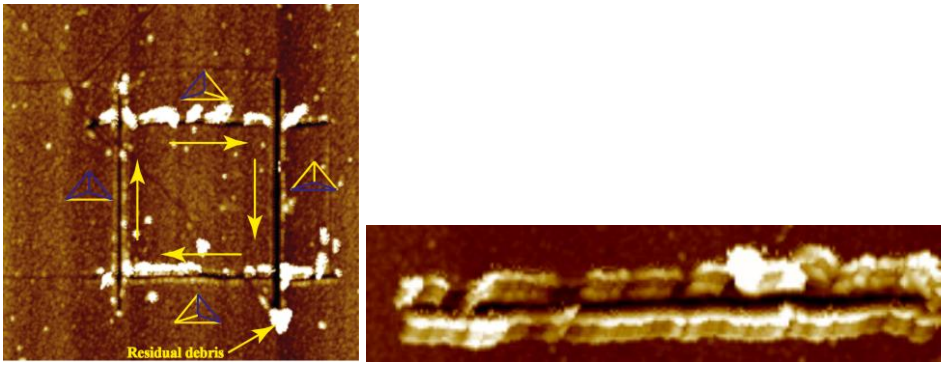

(a) (b)

Figure 4.14 Trench cut by different sides of the probe tip (a), and (b) trench cut by multiple pass

4.2.3 Ploughing Force Modelling and Friction Parameters

An understanding of the cutting forces in the nano scale is important for the analysis of the interaction between the workpiece materials and the tip. The cutting forces are influenced by the mechanical characteristics of the tool and workpiece, such as the cutting and friction coefficients and the elasto-plastic deformation effects.

The ploughing force model is based on the scratching of the AFM probe onto the workpiece. Figure 4.15 depicts the infinitesimal forces associated with the scribing process, where the probe has a tip radius (R_e) and tip semi-angle (α_a = 30°), and η is the angle that the normal vector makes with respect to the feed direction integrated over the area of contact. The apparent friction coefficient (μ) is due to the combination of the adhesion friction (μ_a) and the ploughing friction (μ_p) coefficients [Sin et al., 1979], i.e. $\mu = \mu_a + \mu_p$. To obtain the total forces, the infinitesimal forces need to be integrated over the whole area of contact as:

$$\vec{F} = \int_{-\pi/2}^{\pi/2} \int_{0}^{h} (\kappa \hat{n} + \mu_a \kappa \hat{t}) dA \qquad 4.2$$

where κ is the cutting coefficient (GPa) and $\hat{n}$ and $\hat{t}$ are the normal and tangential unit vectors, respectively.

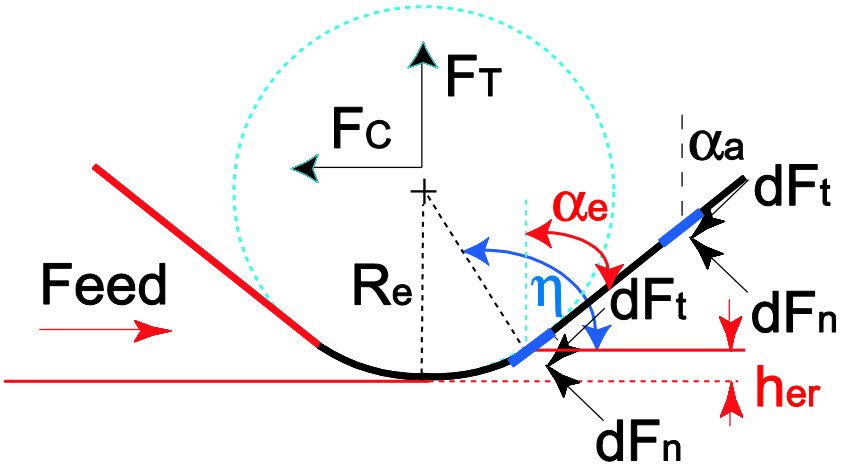

Figure 4.15 Infinitesimal forces on an element of an AFM tip

As shown in Figure 4.15, the angle between the infinitesimal element on the scratch tool and the vertical line is no longer equal to the apex angle (α_a = 30°) when the depth of groove (h) is small. The angle now becomes an effective apex angle, denoted as α_e. Thus, the forces in the cutting and thrust directions can be rewritten as:

$$F_C = \begin{cases} \int_{-\pi/2}^{\pi/2} \int_{0}^{h} \left[\kappa \cos\alpha_e \cos\eta + \mu_a \kappa \sin\alpha_e \cos\eta\right] dA & when \;\; h < R_e(1-\sin\alpha_a) \\ \int_{-\pi/2}^{\pi/2} \int_{0}^{h} \left[\kappa \cos\alpha \cos\eta + \mu_a \kappa \sin\alpha \cos\eta\right] dA & when \;\; h \geq R_e(1-\sin\alpha_a) \end{cases}$$

$$F_T = \begin{cases} \int_{-\pi/2}^{\pi/2} \int_{0}^{h} \left[\kappa \sin\alpha_e - \mu_a \kappa \cos\alpha_e\right] dA & when \;\; h < R_e(1-\sin\alpha_a) \\ \int_{-\pi/2}^{\pi/2} \int_{0}^{h} \left[\kappa \sin\alpha_e + \mu_a \kappa \cos\alpha\right] dA & when \;\; h \geq R_e(1-\sin\alpha_a) \end{cases} \qquad 4.3$$

$$dA \cong \begin{cases} \dfrac{R_e^2}{\sqrt{2R_e h - h^2}} d\eta dh & when \;\; h < R_e(1-\sin\alpha_a) \\ \dfrac{R_e\cos\alpha_a + (h - R_e(1-\sin\alpha_a))\tan\alpha_a}{\cos\alpha_a} d\eta dh & when \;\; h \geq R_e(1-\sin\alpha_a) \end{cases}$$

There are several assumptions and limitations that affect the accuracy of the ploughing force model. It was assumed that the majority of cutting occurs in the ploughing dominant cutting regime. Also, the cutting coefficient is assumed to be constant between the workpiece and probe; and, the effects of the ridge formation and elastic recovery of the material are not considered in the model. The depth of groove was limited to be less than the tip radius, since the model is based on a spherical tip.

At higher depths of cut (i.e. greater than the tip radius), it was observed that, the chips sometimes adhered to the probe, perhaps affecting the force measurements. In addition, the tetrahedron shapes of the tip affected forces and cutting behaviour, where the orientation had a strong influence when the depth was greater than the tip radius [Park et al., 2008].

From Equation 4.2 and the cutting depth (h) from ramp cutting (0-16 μN) shown in Figure 4.12b, the cutting coefficient (k) and adhesion friction coefficient (μ_a) can be identified based on the experimental forces in the cutting and thrust directions and the area of AFM probe involved in cutting. Figure 4.16 shows the cutting coefficient calculated for the scratches produced at 5 μm/s. The depth of groove below the initial surface roughness was disregarded, since the initial surface roughness affected the measured accuracy. Scribing with ramp forces was utilized to identify this parameter.

As can be observed in Figure 4.16, the cutting coefficient increased as the depth of groove decreased. This phenomenon can be attributed to two factors: size effects and aluminum oxides on the surface. The size effects, which increase the stress as the scale is decreased, have been attributed to different causes, such as material work hardening due to strain, strain rate and strain gradient [Vollertsen et al., 2009]. The sputtered aluminum sample formed oxides in the top layer, as it came into contact with air; and, aluminum oxide is harder than that of pure sputtered aluminum.

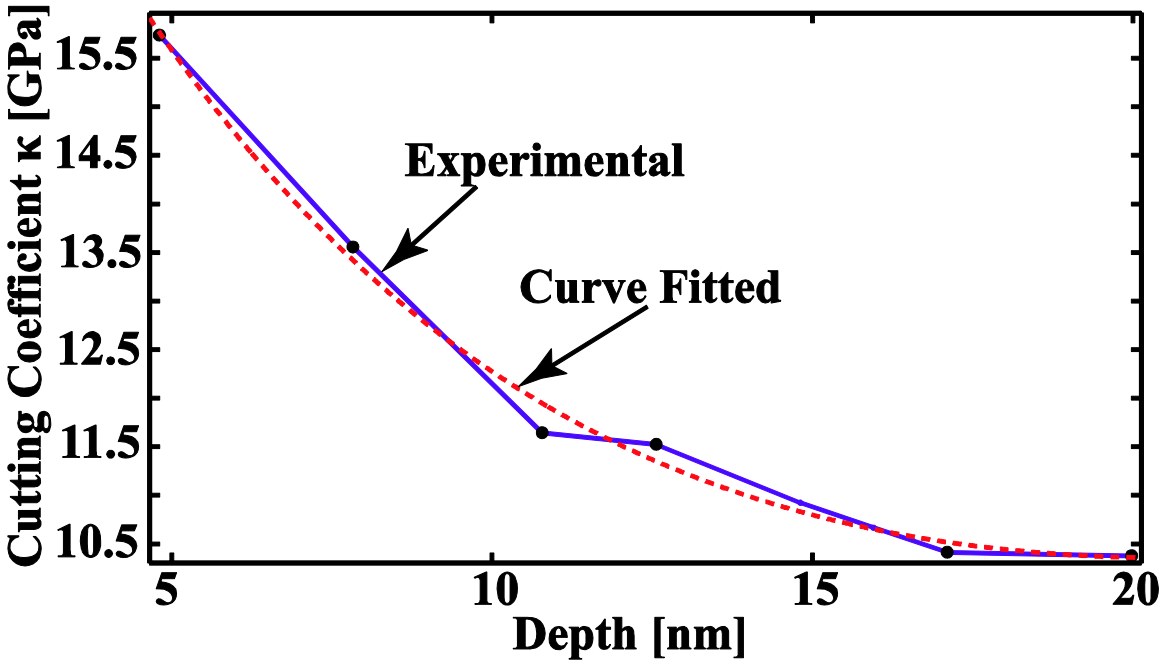

Figure 4.16 Identified and curve fitted cutting coefficients from the ramp force at 5 μm/s

The tribological parameters were also investigated by finding the adhesion friction coefficient from Equation 4.3. The adhesion friction coefficient (μ_a) decreased as the depth increased, as shown in Figure 4.17. This may be attributed to the directions of the workpiece material with respect to the tip radius and depth of groove. This may be

due to more rubbing against the surface when the depth of groove is smaller. This adhesion friction coefficient was smaller than the ploughing friction coefficient.

The ploughing friction coefficient (μ_p), which is caused by plastic deformation of workpiece material, was acquired by using the ploughing model presented by Goddard et al. [1962]:

$$\mu_P = \frac{2}{\pi}\left[\left(\frac{2R_e}{w}\right)^2 \sin^{-1}\left(\frac{w}{2R_e}\right) - \left\{\left(\frac{2R_e}{w}\right)^2 - 1\right\}^{1/2}\right] \qquad 4.4$$

where w is the width of the trench. Goddard considered the tip to be spherical instead of sharp, which is applicable in our case.

The widths of trenches were measured using measurement software (Park AFM XEI Data Analyzing), after scanning the surface with an ultra sharp probe. The ploughing friction coefficient obtained from Equation 4.4 linearly increased from 0.47 to 0.67 when the depth increased from 4.81 to 19.98 nm. Figure 4.17 show that the ploughing friction made a much greater contribution to the apparent friction coefficient than did the adhesion friction. The adhesion friction (μ_a) was calculated from Equation 4.3, and the apparent friction coefficient was calculated by adding the ploughing and adhesion friction. The experimental apparent friction coefficient increased from 0.53 to 0.66 when the depth increased from 4.81 to 19.98 nm, whereas the apparent friction coefficient obtained from the model was approximately constant around at 0.69.

The differences between the experimental and modeled apparent friction coefficients arise from the model's assumptions and side piling effects. Moreover, aluminum oxides on the surface may have affected the friction parameters. When the feed

rate remained constant, the experimentally obtained apparent friction coefficients were similar for both the constant and ramp forces.

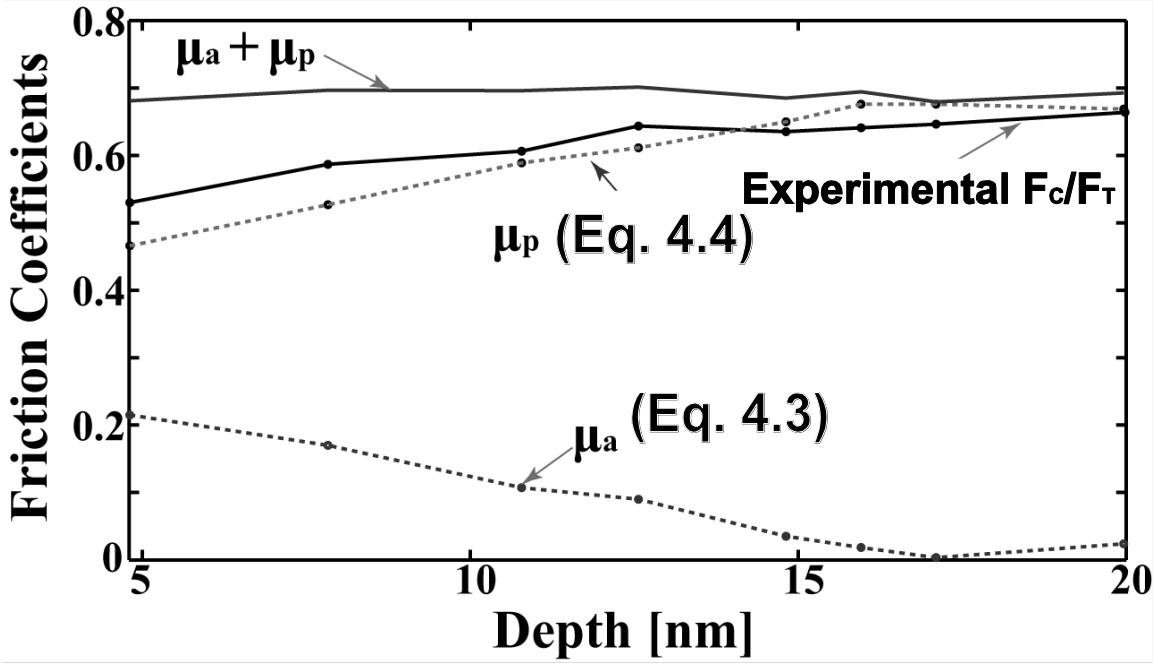

Figure 4.17 Comparison of the overall, ploughing and adhesion friction coefficients at 5 μm/sec

The widths of trenches were measured using the measurement software (XEI Data Analyzing), after scanning the surface with an ultra sharp probe. The ploughing friction coefficient obtained from Equation 4.3 linearly increased from 0.47 to 0.67 when the depth increased from 4.81 to 19.98 nm. Figure 4.17 show that the ploughing friction made a much greater contribution to the apparent friction coefficient than did the adhesion friction. The experimental apparent friction coefficient increased from 0.53 to 0.66 when the depth increased from 4.81 to 19.98 nm, whereas the apparent friction coefficient obtained from the model was approximately constant around at 0.69. The

differences between the experimental and modeled apparent friction coefficients arise from the model's assumptions and side piling effects. Moreover, aluminum oxides on the surface may have affected the friction parameters. When the feed rate remained constant, the experimentally obtained apparent friction coefficients were similar for both the constant and ramp forces.

The experimental friction coefficients for different feed rates were also investigated. At the lower feed rates of 0.5 and 1.0 μm/s, the experimentally obtained apparent friction coefficient was higher (i.e. approximately 0.76 for a thrust force of 12 μN compared to 0.61 at 5.0 μm/s). At the lower feed rates, the piled-up material was higher compared to that of the higher feed rates; thus, the contact area increased. Therefore, greater piling up of material could contribute to additional friction.

The ploughing force model was verified by comparing the depths of cuts (h) from the model and experiments. The depth of groove was identified by minimizing a particular experimental thrust force from the modeled thrust force [Malekian et al., 2010], as outlined in Equation 4.5:

$$Min\{F_{T\exp} - F_{T\mathrm{mod}}\} = Min\{F_{T\exp} - \kappa(h)A_L(h) - \mu_a(h)\kappa(h)A_V(h)\}$$

where

$$A_L = \begin{cases} \frac{\pi}{2}(2R_e h - h^2) & when\ h < R_e(1-\sin\alpha_a) \\ \frac{\pi}{2}\left[(h - R_e(1-\sin\alpha_a))\tan\alpha_a + R_e\cos\alpha_a\right]^2 & when\ h \geq R_e(1-\sin\alpha_a) \end{cases} \qquad 4.5$$

$$A_V = \begin{cases} R_e{}^2(\theta - \frac{1}{2}\sin 2\theta), \quad \theta = \cos^{-1}(1-\frac{h}{R_e}) & when\ \ h < R_e(1-\sin\alpha_a) \\ R_e{}^2(\frac{\pi}{2} - \alpha_a - \frac{1}{2}\sin 2\alpha_a) & when\ h \geq R_e(1-\sin\alpha_a) \\ \quad + \left[h - R_e(1-\sin\alpha_a)\right]\left[(h - R_e(1-\sin\alpha_a))\tan\alpha_a + 2R_e\cos\alpha_a\right] & \end{cases}$$

The cutting coefficient (κ) was taken from the curve fitting of the experimental results shown in Figure 4.16, and the adhesion friction coefficient (μ_a) was taken from Figure 4.17. The obtained value of *h* from the depth identification for a thrust force of 10 μN and a feed rate of 5.0 μm/s was about 14.56 nm whereas it was 13.44 nm in the experiment. For similar feed rates, the overall difference in depth identification was approximately 12%. This deviation may have been caused by several assumptions made for the model and by the non-uniformity of the material.

4.3 Summary of Nano Scribing

In nano scribing, two different types of material were studied in relation to the depth of groove, feed rate effects, width of the groove, cutting forces and apparent friction coefficient. The depth of groove is very small in nano scribing and depends on the stiffness of the probe, material hardness, applied force and feed rates. The soda lime

glass had smaller depth of groove compare to sputtered aluminum. The width of the groove was limited by the depth of the groove, as there is no lateral motion. The feed rate affects the depth of groove, which decreases with increases in the feed rate.

Both the lateral force and the apparent friction coefficient increases with increase in the feed rates. The apparent friction coefficient can be calculated from the adhesion and ploughing friction coefficient while applying the ramp force. The measured friction coefficient and the modeled friction coefficient differed, although both coefficients had similar trends.

A simplified ploughing force model for AFM scribing was formulated, and the adhesion friction and cutting coefficients were identified through the experimentally acquired cutting and thrust forces. It was observed that the cutting coefficient increased as the depth of groove decreased, and it was speculated that this phenomenon was due to size effects and aluminum oxides on the surface. The ploughing friction coefficient was also determined from the geometrical interpretation of the forces and trench areas. In addition, the depth of groove can be predicted based on the model for a sputtered aluminum workpiece.

The challenges in nano scribing are, limited depth of groove, width, large amount of burr formation and large friction coefficient. To address these issues, vibration assisted nano mechanical machining is implemented. The chip load on the cutting tool is less in vibration assisted machining, which will reduce the cutting forces and as a result the depth of groove will increase, the friction force will reduce and the width of groove will

increase. However, the study of brittle and ductile material in this chapter has enabled us to understand the limitations of the nano scribing process.

CHAPTER 5: VIBRATION ASSISTED NANO MECHANICAL MACHINING

Vibration assisted cutting was implemented of sputtered gold as the oxide formation on the pure gold is limited. The limited oxide formation on the surface of pure gold gives uniform material properties compared to other metallic substrates. However, the grain boundaries of the gold particles can still influence the cutting or friction forces. The difference in the methodology of nano scribing and vibration assisted nano mechanical machining is described before. In vibration assisted cutting, a rotational motion is provided to the workpiece. The rotation motion of the workpiece mimics the milling process and the chip load on the AFM probe is reduced compare to conventional cutting. Therefore, the burr formation and the friction should be reduced as well. In this chapter, vibration assisted nano machining will be applied and at the same time the results will be compared to nano scribing results to find out the advantages and disadvantages of different cutting methods.

5.1 Methodology of Vibration Assisted Machining

Vibration-assisted machining is a complex process and requires close attention in order to synchronize all the cutting parameters. In AFM probe based nano mechanical machining, vibration is applied to the workpiece instead of the cutting tool. Conventional vibration-assisted machining is performed by 2D elliptical motion on a fixed plane that is perpendicular to the vertical axis. However, circular/elliptical vibration-assisted machining can be performed on other planes as well. Figure 5.1 shows vibration-assisted machining performed on different planes, where the elliptical motion in the XZ plane is conventional elliptical vibration-assisted machining and the elliptical machining in the XY plane mimics the milling process.

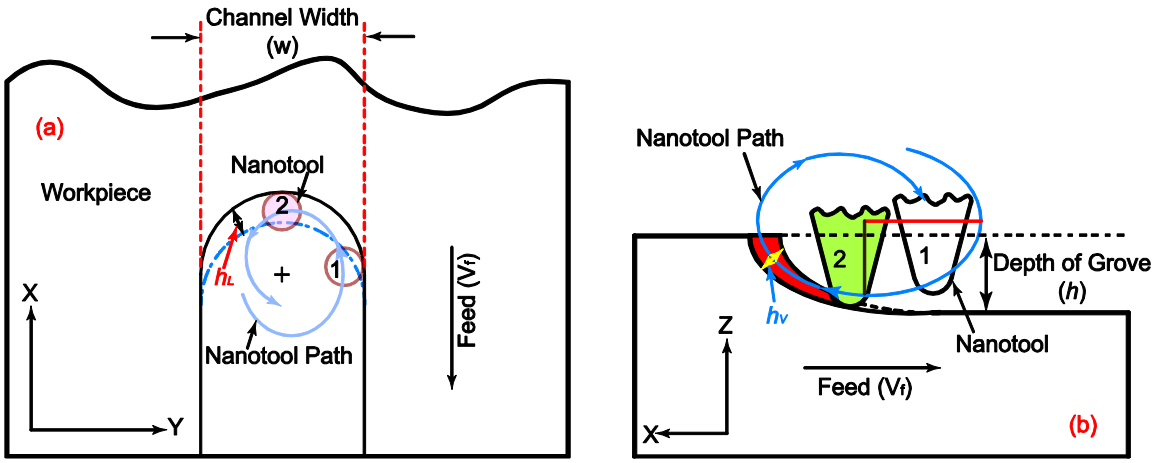

Figure 5.1 Vibration-assisted nano scale cutting: (a) on the XY plane and (b) on the XZ plane [Gozen et al., 2010]

Despite the complexity associated with vibration-assisted machining, there are many advantages, as discussed perviously. AFM probe based vibration-assisted

machining can also contribute to the machining of micro/nano scale features by adding advantages found in macro scale machining.

Tip-based micro/nano mechanical machining is performed mainly by scratching; and, the cutting forces, tool wear rates, pileups and burr formations are quite high. AFM probe based vibration-assisted machining can eliminate these problems of conventional machining by reducing the cutting forces with intermittent cutting and tool/workpiece interactions. As it was discussed that, in vibration assisted nano mechanical machining, the chip load is less therefore, there is a difference in the chip generation. The chip generation method will show why the cutting forces will be less and the depth of groove will increase in vibration assisted machining

5.2 Chip Generation Mechanism in Vibration Assisted Machining

Unlike in macro machining, the tool-material interaction in nano scale cutting operation is significantly affected by interaction forces. In order to understand and estimate the effects of Z-axis vibration on the resulting depth of groove, the dynamic properties of the probe in contact with the material are investigated. A finite element (FE) model of a cantilever beam was considered with a spring at the end, where the spring represented the contact stiffness between the probe and the material. The contact stiffness k^* can be found from Equation 5.1, where E^* is the reduced modulus of elasticity, R_e is the radius of the contact surface, F_T is the thrust force applied at the contact area [Mostofa et al., 2013]:

$$k^* = \sqrt[3]{6E^{*2}R_eF_T} \qquad 5.1$$

The thrust force F_T is identified from conventional scribing experiments. The reduced modulus of elasticity E^* of the workpiece material can be found from nano-indentation experiments, which was identified to be 77.5 GPa. In the analysis of the indentation results, the Oliver-Pharr method [Oliver et al., 2004] was utilized. Knowing that the experimental set point force was kept constant at 20 μN, the contact stiffness k^* of the probe-workpiece contact was approximately 3001 N/m, as calculated using Equation 5.1

A FE simulation was performed based on the cantilever-spring model, where the cantilever had a static stiffness of 163 N/m and contact stiffness k^* (3001 N/m) was calculated from Equation 5.1. A frequency response function (FRF) of the probe while the scribing was in process was then identified, as shown in Figure 5.2. The FEA analysis was performed by using MATLAB, considering beam specifications, cantilever beam and boundary conditions. A simple point-mass-spring system was assumed to represent the system of a cantilever in contact with the sample surface [Rabe et al. 1996]. Two different stiffness parameters play roles in the overall response of the system: the cantilever static stiffness and the contact stiffness.

The specifications of beam was given as a length of 662 μm, a width of 24 μm, probe material of sapphire with a density of 3980 kg/m3, frequency range of 0 - 10 MHz, element type was a 3D beam element, number of elements was 10, beam cross section was a semicircle and boundary conditions of fixed free cantilever beam with contact stiffness working between the probe tip and sample surface, as shown in Figure 5.2.

From the FRF plot, the ratio of the displacement of the probe to the force at a vibration of 10 kHz was 0.317 nm/μN. The FRF provides the deflection of probe due to the applied thrust force at a certain vibration frequency.

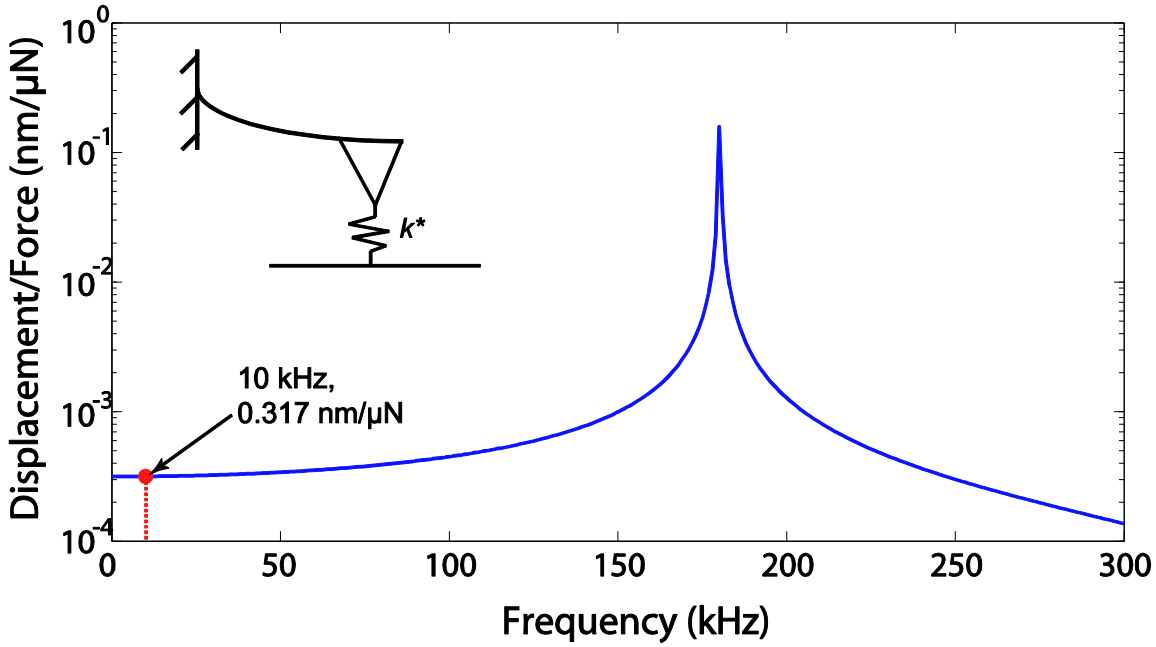

Figure 5.2 FRF of the AFM probe in the conventional scribing process

The change in the resulting depth of groove due to the application of Z-axis vibration-assisted machining can be predicted based on the initial depth of groove without vibration, applied vibration amplitude, and the deflection of probe at the maximum force applied. Figure 5.3 shows a schematic of how the final depth of groove in Z-axis vibration-assisted machining was estimated.

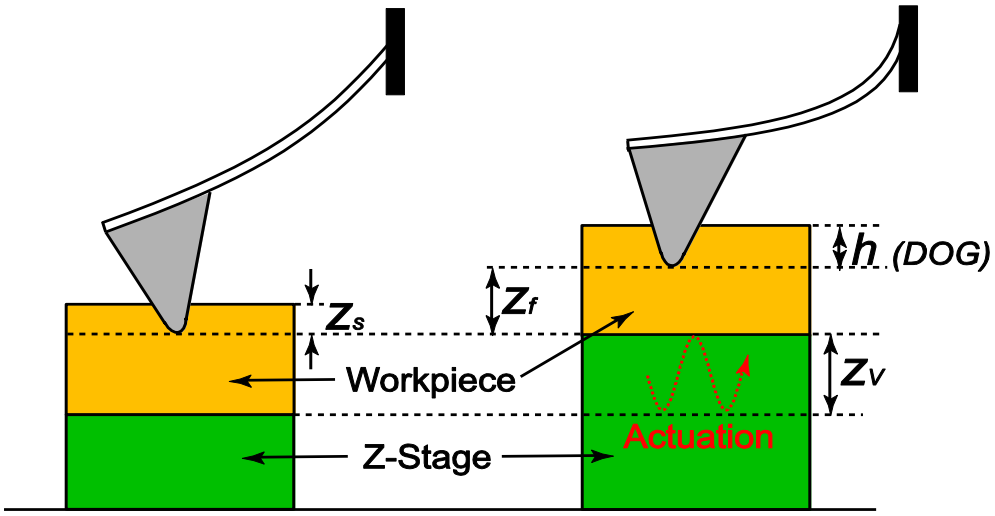

Figure 5.3 Schematic of Z-axis vibration-assisted machining

In conventional scribing, the depth of groove is achieved by the set point force and this initial depth of groove due to the set point force is called z_s. When the Z-axis vibration stage is actuated, the workpiece moves upward. The maximum displacement of the workpiece surface is denoted as z_v, equal to the peak-to-peak vibration displacements. If the probe cantilever is rigid, the tool penetrates into the surface as much as the workpiece has displaced; however, the cantilever is deflected upward due to the applied force. The amount of deflection z_f can be calculated from the measured thrust force F_T and the FRF at the applied frequency (see Figure 5.2). Therefore, the total depth of groove achieved from the Z-axis vibration-assisted machining (h) is found using Equation 5.2:

$$h = z_s + z_v - z_f \qquad 5.2$$

The depth of groove estimated using this equation was comparatively analyzed with the experimental results from Z-axis vibration-assisted machining and combination of XY and Z-axis vibration-assisted machining. The described estimation of depth of groove will be verified depending on the experimental findings.

In vibration assisted machining, the cutting tool should follow an elliptical/circular path according to the applied signal to the actuator. To verify the tool motion, relatively soft material (Photoresist HPR 504) is machined so that the tool path can be seen. The rotational motion of the XY-piezo stage was confirmed when a signal was applied to the sample and the stage was kept running at the end of cutting. In Figure 5.4, the scanning electron microscope (SEM) image shows a circular tool mark at the end of groove, which indicates the AFM probe followed a circular pattern.

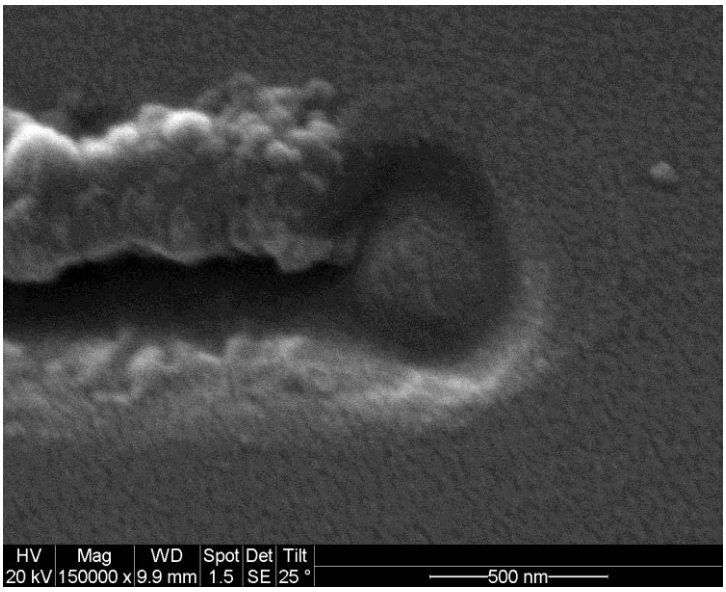

Figure 5.4 SEM image of the trench end showing circular tool path due to XY piezo stage motion

5.3 Vibration-Assisted Machining

A sputtered gold sample was used to examine vibration-assisted nano machining though many materials have been tested, the results for gold cutting is presented as a representative material since gold show significantly less oxidizations compared to other metallic materials. The surface roughness was measured before every experiment was performed; and, the average surface roughness (R_a) was approximately 4.6 nm, and the maximum height (Rz) was approximately 56.2 nm. These values could be different depending on location; however, the machining was performed near the measurement area. The investigation was 4-pronged: nano scribing, Z-axis vibration cutting, XY planar vibration cutting and XYZ vibration cutting. The X-, Y- and Z-axes displacements were provided by the function generator. There were no voltage amplifier; therefore, the Z-axis signal was kept at 10 kHz.

The displacement of the Z-stage was measured by a capacitance sensor, with the measurement shown in Figure 5.5. The signal was measured by the capacitance sensor and then the fast Fourier transform (FFT) was taken to find the displacement of the Z-axis piezo actuator. The supplied voltage from the function generator was not applied to the piezo actuator, due to high frequency and high capacitance; therefore, the ratio of displacement to input voltage was identified as 32.5 nm/V at 10.0 kHz (26 nm at 0.8 V and 10 kHz, resulting in the ratio of displacement to input voltage as 32.5 nm/V).

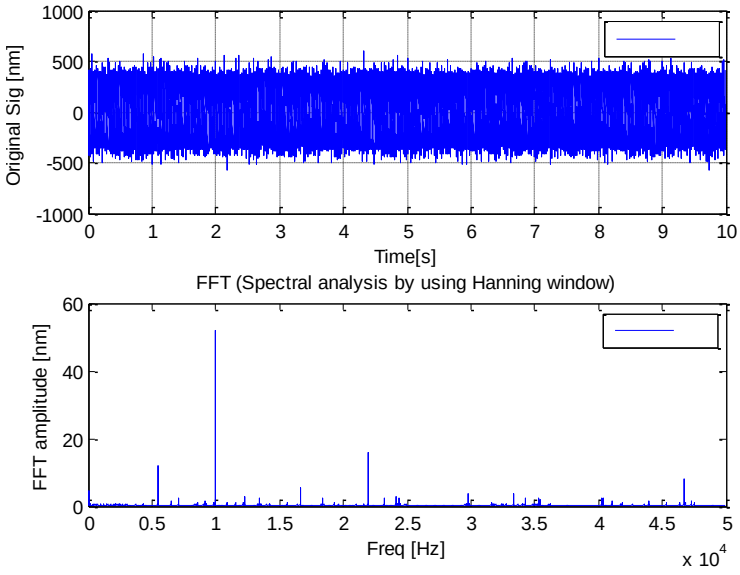

Figure 5.5 Displacement of the Z-axis piezo actuator at 20 V (peak to peak) and a frequency of 10 kHz

The XY plane was excited at 265 Hz with 714 nm and 1292 nm for the X-axis and Y-axis (peak to peak) displacements, respectively. The thrust force was 20 μN, and the feed rate was 0.5 μm/s. The experiment was repeated at least three times for each condition. The lateral and vertical calibration factors were found to be 5.37 and 9.63 μN/V, respectively. The temperature and humidity during the calibration and vibration assisted cutting experiment were measured and recorded as 19°C and 13%, respectively.

5.3.1 Cutting Results

The cutting forces were monitored, and the scratching areas were scanned with a sharp AFM probe (3-5 nm) to get high-resolution images. The cutting results are summarized in Table 5.1. The depth of groove, apparent friction (F_C/F_T) coefficient and

ratio of pileup to depth of groove were measured. The investigation showed that, when vibration-assisted nano machining was active, the depth of groove increased, the apparent friction coefficient decreased, and the ratio of pileup to depth of groove indicated that vibration-assisted machining was dominated by shearing instead of ploughing.

Table 5.1 Comparison of different cutting methods

Cutting Conditions	No Vibration	Z-Axis Vibration (10 kHz)	XY Planar Vibration (265 Hz)	XYZ Vibration (XY: 265 Hz; Z: 10 kHz)
Depth of groove (nm)	$14^{+0.4}_{-0.6}$	$34^{+2.0}_{-0.4}$	$162^{+3.0}_{-6.7}$	$178.5^{+5.0}_{-5.4}$
F_C/F_T	0.246	0.212	0.209	0.199
Pileup/depth of groove	2.14	1.64	0.98	1.19

The comparative topography and measured cutting forces are compared in Figure 5.6 which illustrates the AFM topography with surface and depth profiles and cutting and thrust forces for each method used in the experiments. The width of groove increased along with the increase in depth, following the tetrahedral geometry of the AFM probe.

The cutting forces were measured and the chip generating mechanism is identified. The direct visualization of the cutting method is difficult due to the small size of the AFM probe and the high speed vibration cutting. Therefore, the mechanism described in this thesis is based on the measured cutting force, deflection of the cantilever, and frequency response of the cantilever considering contact stiffness while scribing. Hence, the real cutting method may differ if direct visualization or cutting simulation is possible. Molecular dynamic (MD) simulation is performed by scholars [Urbakh et al., 2004] for scribing in tribology study but the simulated results deviates from the experimental results as the MD simulation can not be done in low feed rates due to higher computing power. The FFT analysis of the Z, XY and XYZ vibration-assisted cutting is displayed in Figure 5.7. It was observed that the amplitude (V) was large at the applied frequency for each case.

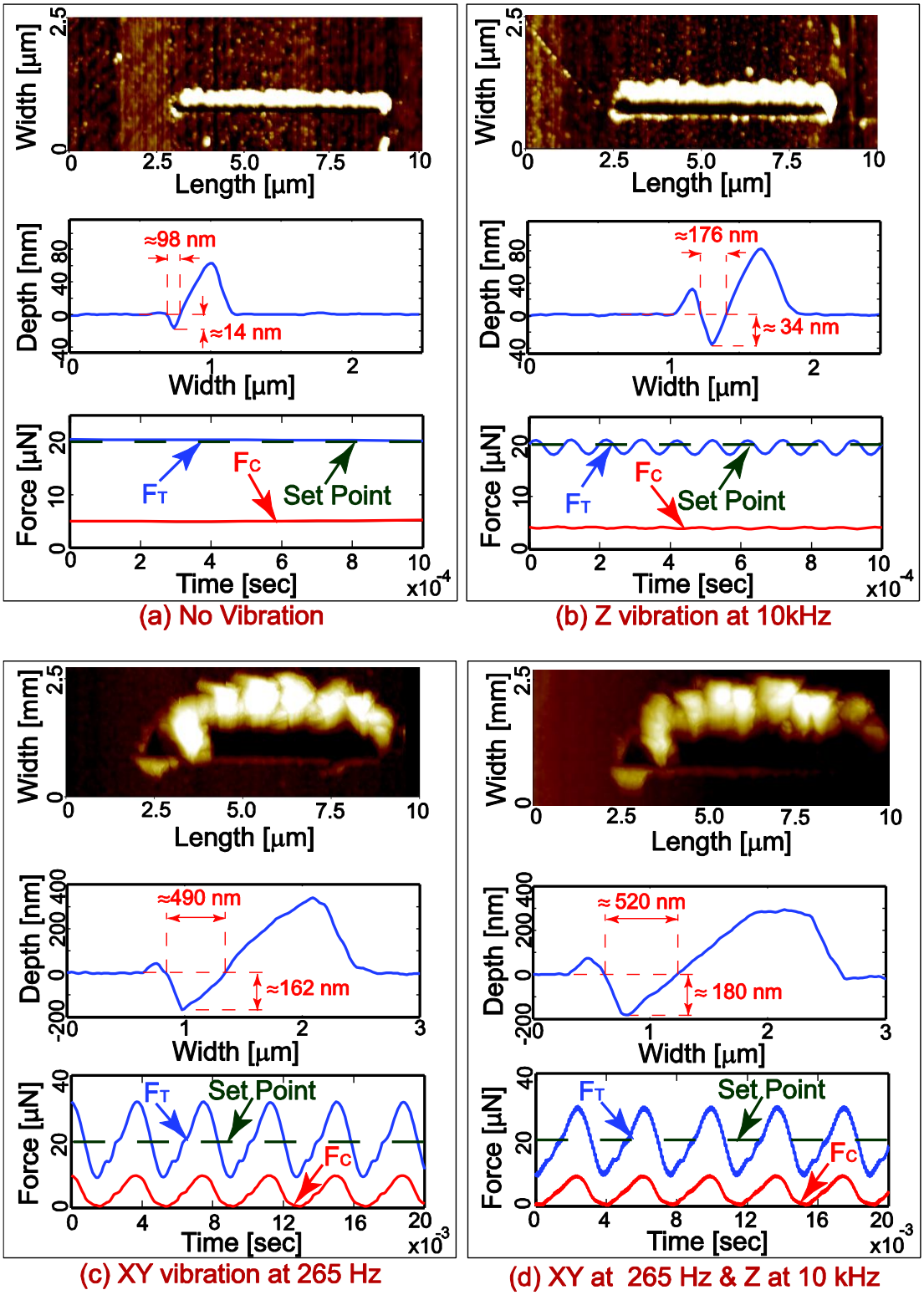

Figure 5.6 AFM topography, depth profile and force measurements for each vibration technique

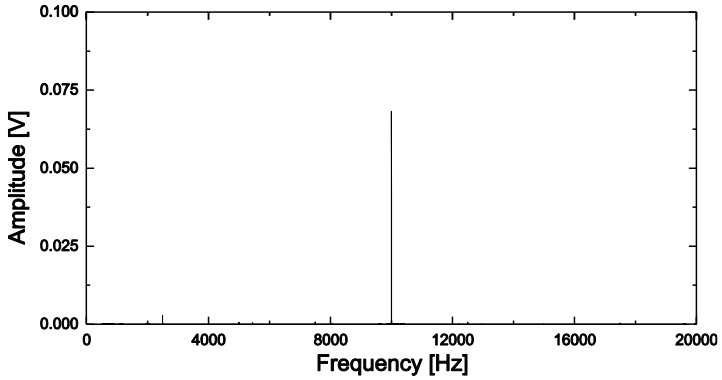

(a)

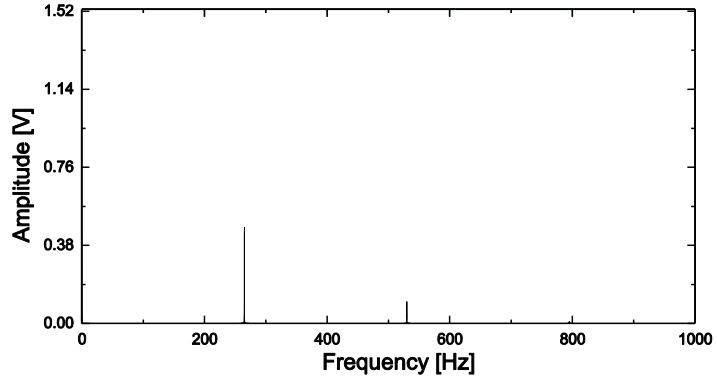

(b)

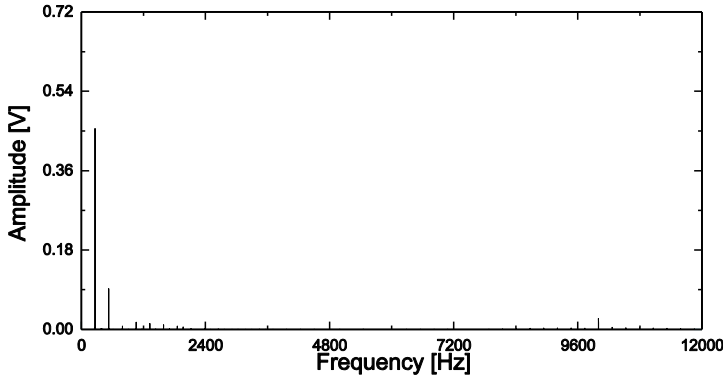

(c)

Figure 5.7 FFT analyses of the thrust forces for (a) Z-axis vibration cutting, (b) XY planar vibration cutting, and (c) XYZ vibration cutting

5.3.2 Chip Generation Mechanism Validation

The total depth of groove from the Z-axis vibration-assisted machining was estimated using Equation 5.2. The depth of groove obtained from the conventional scribing technique z_s was 14 nm, the workpiece displacement z_v was 26 nm, and the displacement of the probe due to the maximum force 20 μN (z_f) at 10 kHz vibration was 6.34 nm (see Figure 5.2). The total estimated depth of groove was 33.5 nm, which was 1.47% different from the experimental result. It can be concluded that the estimation technique is valid, and the Z-axis vibration-assisted machining is a viable method to control the depth of groove.

In Figure 5.6, as the depth of groove increased, the average forces decreased with Z-axis vibration-assisted machining (conventional lateral force of 4.92 μN, Z-axis vibration machining of 4.24 μN). The reduction in forces can be attributed to the vertical vibration and continuous feed, which create similar effects to that of a 2D vibration-assisted cutting technique. In 2D vibration machining, the elliptical motion of the tool detaches the tool from the workpiece by applying velocity in the opposite direction of the tool feed, reducing the average forces. In addition, the upward motion of the tool pushes the chip upward, assisting the chip flow. This reverses the friction force, thereby significantly reducing the shear angle and resulting in further decreases in cutting and thrust forces [Moriwaki et al., 1995].

Figure 5.6c illustrates the results for XY vibration-assisted machining. While the average thrust force was maintained at the set point force, the depth of groove (DOG) increased from 14 nm of the conventional scribing to 162 nm with the XY planar vibration-assisted machining. It was observed that the minimum cutting force reached

almost 0 N. The thrust force maintained its average value at the set point force of 20 μN, with a maximum thrust force at 30 μN and a minimum thrust force at 10 μN.

The comparison of the conventional scribing and XY planar vibration-assisted machining is illustrated in Figure 5.6. In conventional scribing technique, the tool makes groove of width (*w)*, where the uncut chip thickness in top view is considered same as *w* shown in Figure 5.8.

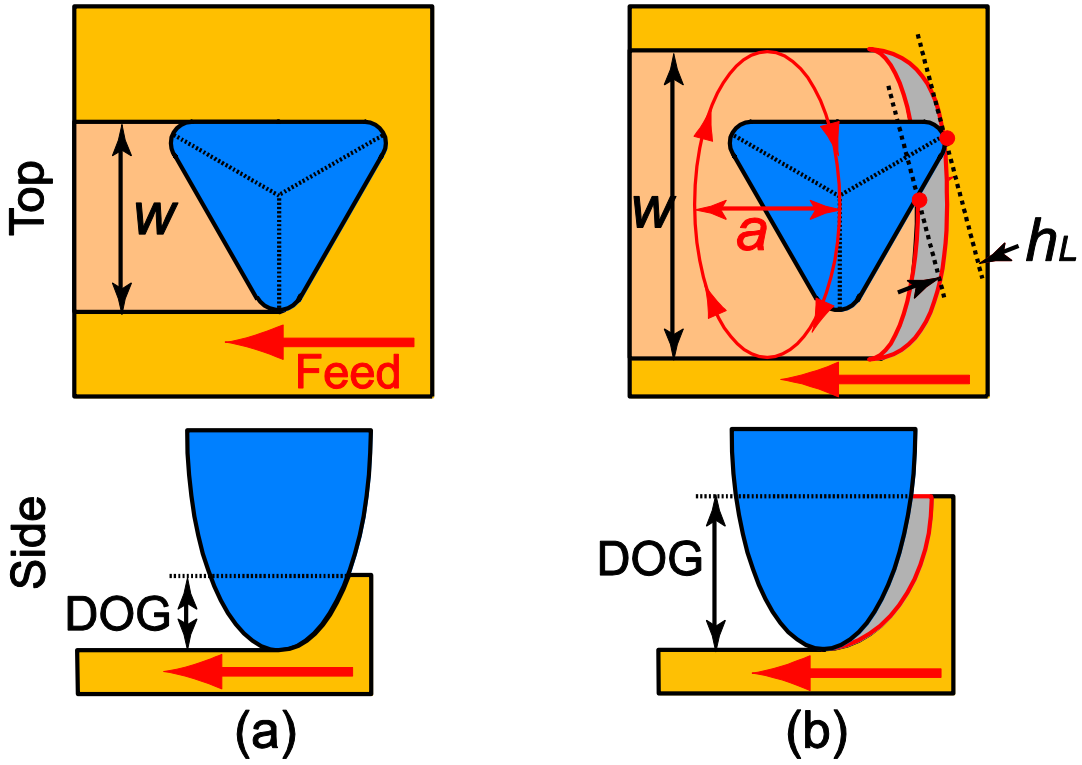

Figure 5.8 Top and side views of (a) conventional scribing and (b) XY vibration-assisted machining

In XY vibration-assisted machining, the process mimicked milling operations by rotating the workpiece in the XY plane to cut a smaller amount of the uncut chip thickness h_L at each vibration cycle. While the groove width *w* has increased due to the

tool motion, the actual amount of uncut chip thickness h_L at each instance is smaller since the uncut chip thickness is found with respect to the instantaneous tool velocity of the rotational motion.

With smaller amount of uncut chip thickness, applied forces are reduced greatly. In order to maintain the average thrust force at the set point force, the tool goes into the material deeper. Thus the depth and width of the groove obtained in XY planar vibration-assisted machining were significantly larger than both conventional scribing and Z-axis vibration-assisted machining. Force modelling and precise control of depth of groove in XY vibration-assisted machining are difficult since the vibration amplitudes applied to the workpiece and the relative tool path do not match due to the large deflection of the probe.

XYZ vibration-assisted machining was performed in order to combine the effects of XY vibration with Z-axis vibration-assisted machining, giving more controls to resultant geometry of groove. As it is shown in Figure 5.9d, the combination of XY (265 Hz) and Z (10 kHz) vibration-assisted machining increased the depth of groove more than any other cutting method described, and the effects of the Z-axis vibration were directly added to those of XY vibration-assisted machining. The Z-axis frequency was chosen depending on the capacitance displacement sensor limitations. The 10 kHz frequency of the piezo actuator was measured to characterize the piezo actuator at that frequency. On the other hand, the XY frequency was chosen corresponding to the rpm value and considering AFM probe safety. The 265 Hz frequency applied 15,900 rotation per minute to the XY stage. The cutting starts from zero rpm; therefore, the sudden application of a higher frequency could make the AFM probe vulnerable. Therefore, 265

Hz was applied to the XY stage for safety of the AFM probe. Moreover, the crosstalk between the X and Y stages was minimal at 265 Hz when tested.

Using Equation 5.2, the total depth of groove in XYZ vibration-assisted machining was estimated to be 178.49 nm. The initial amount of depth of groove from the XY planar vibration-assisted machining (z_s) was 162 nm, the workpiece displacement in Z-axis (z_v) was 26 nm, and the probe deflection due to the maximum force 30 μN (z_f) at 10 kHz excitation was 9.51 nm. The average depth of groove of 178.5 nm was measured from the experiment using XYZ vibration-assisted machining. This demonstrates that Z-axis vibration-assisted machining can provide additional control to the depth of the fabricated features with high accuracy.

Table 5.2 The error calculation between the experimental results and estimation

Method	Estimation (nm)	Experimental Results (nm)	Error (%)
Z-axis vibration	33.5	$34^{+2.0}_{-0.4}$	$1.5^{+6.9}_{-0.3}$
XYZ vibration	178.46	$178.5^{+5.0}_{-5.4}$	$0.02^{+2.75}_{-3}$

In nano mechanical machining, the uncut chip thickness is very small that they are comparable to the edge radius of the tool. When the uncut chip thickness is small enough that it is smaller than minimum uncut chip thickness, the transition of cutting mode occurs, ploughing (plastic deformation) of material becomes more dominant than shearing (removal as chips) [Park et al., 2009]. Ploughing not only takes more forces than shearing but leaves side pileups as well. Effects of the vibration-assisted machining in

burr reduction were assessed using scanning electron microscopy (SEM) images of the resulting grooves from each method (see Figure 5.9).

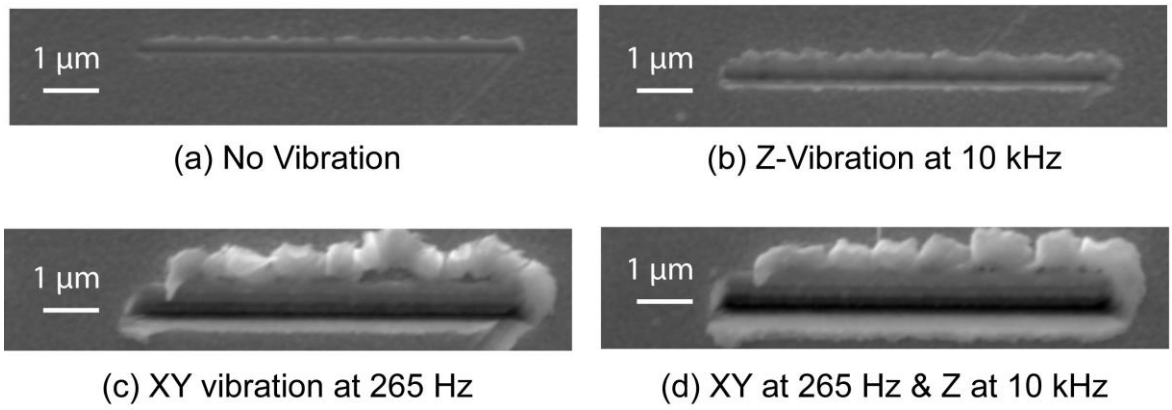

Figure 5.9 Comparison of burr and chip formation

Depth profiles from Figure 5.6 of all grooves, showed that there was large pileup on one side and smaller pileup on the other side. It was assumed that deformed material was piled up on one side due to the slanted tool geometry. SEM images in Figures 5.9c and 5.9d revealed that the large pileups were actually the segmented chips created by XY planar vibration-assisted machining. There was no chip formation in conventional scribing and Z-vibration-assisted machining. The XY planar vibration has induced more shearing of the material than ploughing, similar to the milling process.

5.4 Nano Pattern Fabrications

Nano patterns are surface features that can enhance different scientific applications where the surface-to-volume ratio is important, such as security [Phillips,

2004] and optics [Park et al., 2008]. The many shapes of nano patterns can be fabricated with AFM. Figure 5.10 shows elliptical nano patterns fabricated on a photoresist sample with vibration-assisted machining and nano scribing processes. The vibration-assisted machining provided wider channel than the nano scribing process. Figure 5.11 shows a schematic and AFM image of a repeating nano pattern of circular cuts. In smaller pattern machining, the pileup material appears to be problem in achieving a perfect nano pattern [Aurich et al., 2009].

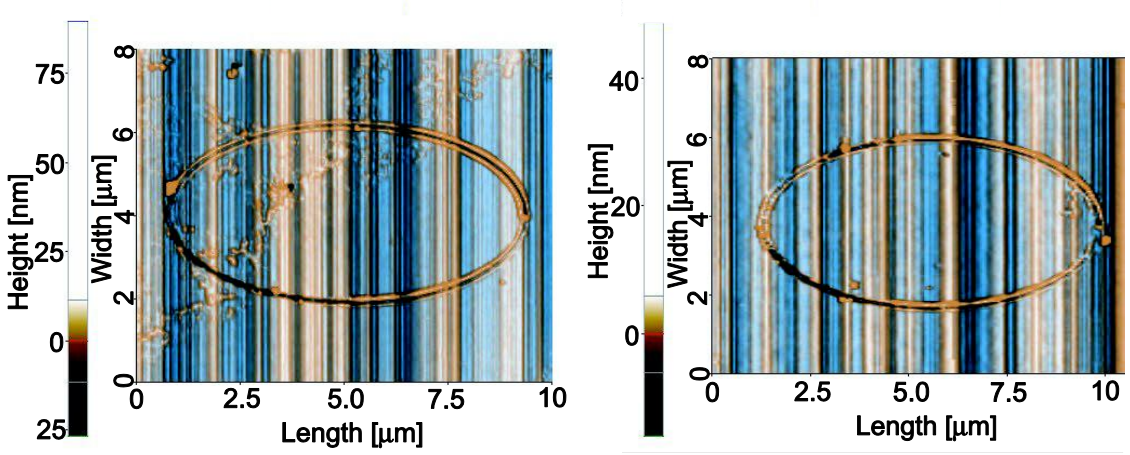

(a) (b)

Figure 5.10 Nano pattern fabrications with (a) vibration-assisted machining (10 µN, 5.0 µm/s and 0.5V) and (b) nano scribing (10 µN, 5.0 µm/s)

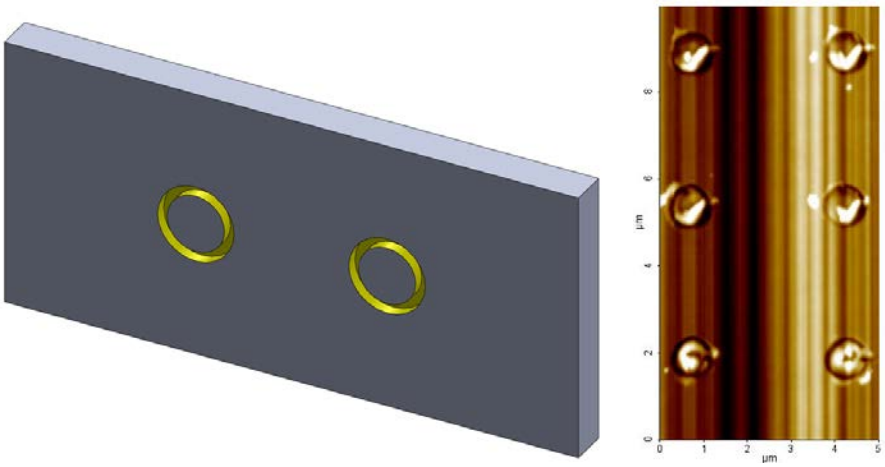

(a) (b)

Figure 5.11 (a) Schematic of nano pattern and (b) fabrication of repeating nano pattern (From the top, 5, 6 and 7 μN, 0.5 V, 1.0 μm/s)

Bitmap image information can be used to fabricate features with AFM. Various complex shapes can be fabricated using image information. A drawing of a maple leaf was made with Microsoft Paint software and used to fabricate a feature on gold through nano scribing, Z-axis vibration and XY vibration cutting. For all cutting methodologies, the set point force was 15 μN and the feed rate was 2.0 μm/s. From the function generator, the Z-axis vibration was 10 V and 10 kHz, and the XY vibration was 5 V and 265 Hz. Figure 5.12 shows the nano fabrication of the maple leaf with the different methods. It was observed that the fabricated features had different depths (No vibration = 14.7 nm; Z vibration = 34.6 nm; XY vibration = 68.06 nm) of groove depending on the fabrication methodology.

The fabrication of nano patterns by using bitmap image information could also vary. According to the bitmap image, either the black area or white area could be

fabricated. In Figure 5.12, the nano pattern was fabricated using the black region; whereas the white area was used for the fabrication of the features shown in Figure 5.13shows the fabrication of similar feature where the white area has been fabricated.

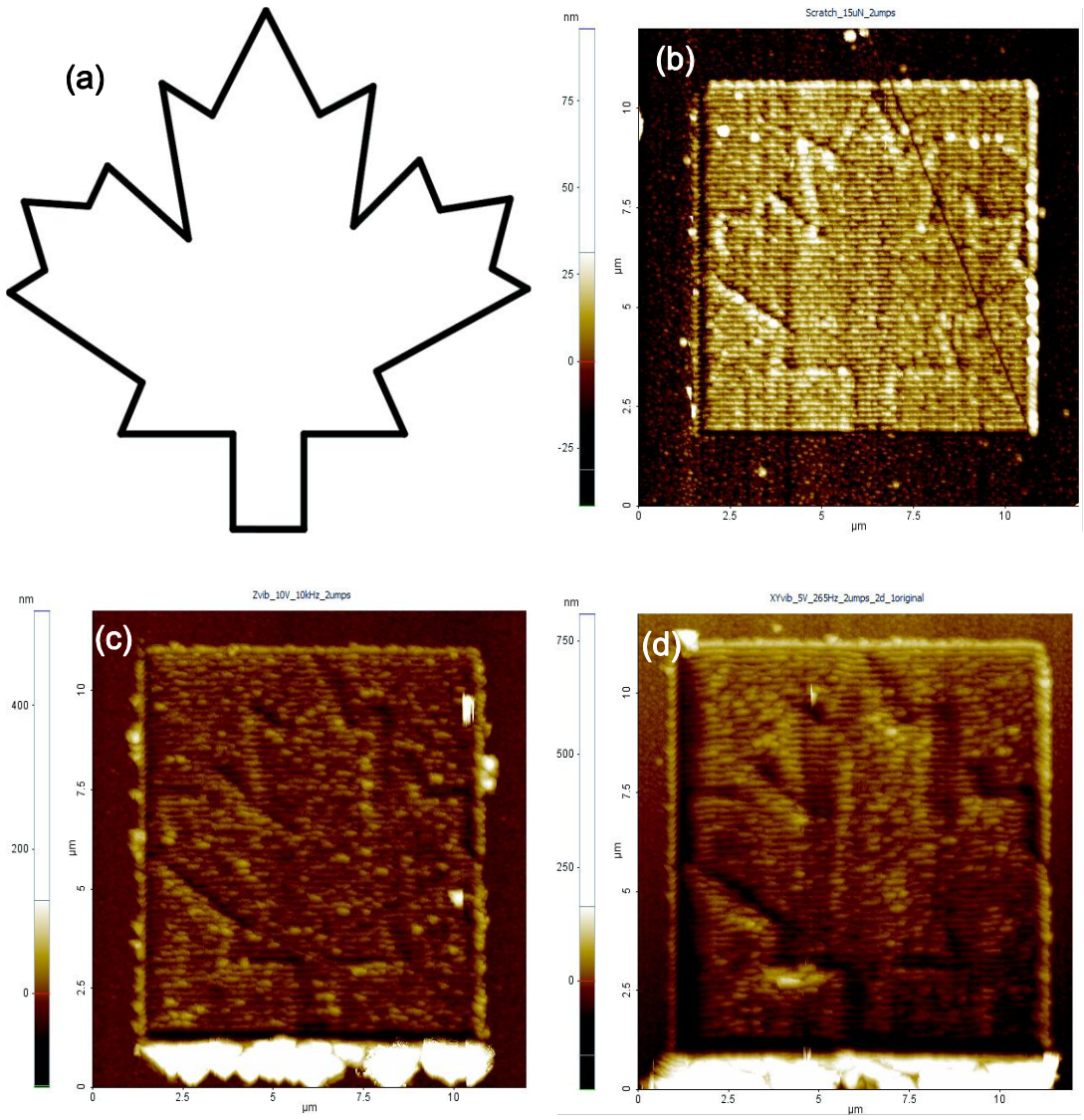

Figure 5.12 Fabrication of a complex feature using the black area of the bitmap image (a): (b) nano scribing, (c) Z-axis vibration, and (d) ZY planar vibration cutting

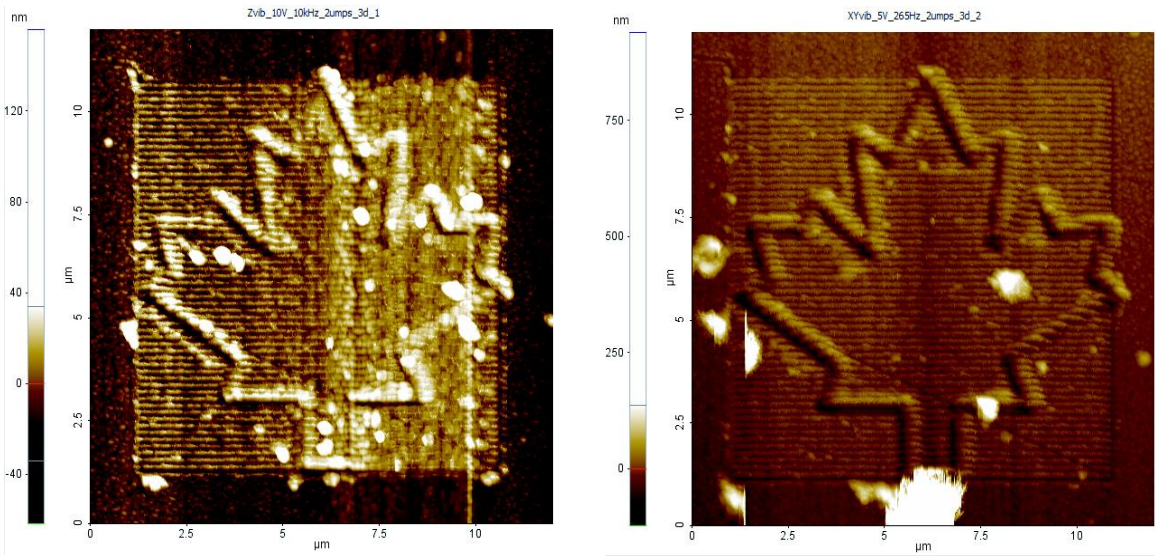

(a) (b)

Figure 5.13 Fabrication of a complex feature using the white area of the bitmap image in Figure 5.13 (a) Z-axis vibration (10V, 10 kHz) and (b) XY planar vibration cutting (5V, 265 Hz)

5.5 Summary of Vibration Assisted Nano Machining

In this chapter, nano scribing, Z-axis vibration cutting, XY planar vibration cutting and XYZ vibration cutting were applied on different materials, and different types of features were fabricated. It was observed that the vibration-assisted nano machining could provide better machinability in terms of a deeper depth of groove with a limited stiffness of cantilever and reduced pileup in machining. The lower friction can increase the tool life and cutting cycle.

The tribological study provided an increased understanding of nano scale machining with AFM. It was observed that the friction coefficient in vibration assisted nano mechanical machining is less than conventional nano scribing. The friction

coefficients in vibration assisted cutting even smaller if it is compared to the obtained depth of groove and width of the groove and compare it with nano scribing.

Nano pattern machining in vibration-assisted nano mechanical machining is much easier and can engrave any features with the appropriate condition settings. However, it was observed that, in machining nano patterns, the tool shape may play an important role in pileup, as different sides of the probe may engage in cutting.

Further studies are needed in vibration-assisted nano scale machining. Difficulties may arise from uncertainties in the nano scale, such as the workpiece grain boundary effect, the influence of humidity on probe sensitivity and water film lubrication of the workpiece, and tip-probe misalignment affecting chip formation.

CHAPTER 6. SUMMARY AND FUTURE WORKS

The application of miniature components has increased extensively in recent years; and, there are different types of processes in the fabrication of miniature components. There is no doubt that photolithography plays a very important role in fabricating miniature components. However, only a few materials can be used as workpieces in photolithography and do not include alloys, composites, polymers and ceramics. Moreover, this technology is not able to fabricate 3D geometries. These limitations pushed researchers and manufacturers to utilize chemical fabrication processes that were not environmentally friendly. In addition, mask making costs in fabricating customized products make the photolithography process inefficient.

Tool-based fabrication can overcome the limitations associated with the photolithography process, and micro machining is able to fabricate miniature components. The cutting tool used in micro machining can be as small as 50 μm (diameter of milling tool) [Malekian et al., 2010]. However, with the advent of different biological and bio-influenced applications that may require nano scale features, such as nano channels on glass, the dimensions can be as small as 15 nm in depth [Mao et al., 2005].

The fabrication method for nano-sized channels is chemical etching, which requires the use of chemicals. Channels of this size can also be easily fabricated with AFM (atomic force microscopy) probe based scribing, as shown in this thesis. With

vibration-assisted machining, the fabrication range, in terms of required depth and width, is much wider than with the nano scribing method.

In tool-based nano fabrication, optimal cutting requires investigations into different factors, such as excessive cutting force, friction, tool wear, material removal rate and vibration. In nano scale machining, the tool is fragile and tool failure can occur during cutting; therefore, the selection of cutting parameters is important.

In this thesis, the chip formation mechanism, cutting forces, wear rate, friction and material removal rate were studied in nano scribing and vibration-assisted machining. It was found that vibration-assisted machining has many advantages over the nano scribing method. The calibration method to measure the cutting forces was extended and a friction model was developed; however, the friction model was more suitable for nano scribing and requires more investigation for its use with vibration-assisted machining. Depth identification was also performed for nano scribing; however, it did not work for vibration-assisted machining, as the cutting principles are different.

In this thesis, various materials were utilized, such as glass, aluminum and gold. Polycarbonate, polystyrene and nanocomposites (carbon nanotube based polystyrene) were also investigated, although the results are not included here. It was observed that materials that are difficult to use as workpieces with the photolithography process can be employed using vibration-assisted nano mechanical machining.

The ductile cutting of brittle material was investigated, and it was shown that glass or ceramic material can be fabricated without any brittle failure. The minimum uncut chip thickness (MUCT) was identified for soda lime glass.

The cutting parameters play important roles in nano mechanical machining, regardless the principle of cutting. The feed rate is important to the depth of groove: the depth of groove decreases with increases in the feed rate. The feed rate and hence the depth of groove also influence the chip thickness in vibration-assisted cutting and lateral force in nano scribing. Increases in thrust force also increase the depth of groove; however, the relationship between the thrust force and the depth of groove was found to be nonlinear.

Three different types of vibration-assisted machining were performed and their performances were evaluated. XYZ vibration-assisted machining provided the higher depth of groove, lower friction and wider groove than Z-axis and XY planar vibration cutting. However, the difference between XY and XYZ vibration-assisted machining was small (10%). Vibration-assisted machining enabled AFM probe based nano scale machining to use limited probe stiffness to obtain much larger depths and widths than was possible in the nano scribing method. The lower friction in vibration-assisted machining definitely increases the life of the tool.

6.1 Novel Contributions

In the AFM probe based conventional nano scribing method, there are many limitations. A vibration-assisted nano mechanical system was developed and applied to various materials to investigate machining performances and compare them to those of conventional scribing. Vibration-assisted machining provided better machining performances than scribing, in terms of lower cutting force and greater depth and width

of the machined channel. It has also provided better machinability while fabricating complex shapes. Vibration-assisted nano mechanical machining, therefore, presents significant potential for nano scale machining, eliminating various limitations of the scribing method. The novel contributions in this thesis are discussed in the following subsections.

6.1.1 Development of a Vibration-Assisted Nano Mechanical System

The first major challenge in the establishment of a vibration-assisted nano mechanical machining method using commercial atomic force microscopy (AFM) was the development of the XYZ stage. The XYZ stage was designed to apply circular or elliptical motion to the workpiece in XY plane and normal vertical displacement (i.e. Z-axis) to the XY plane. The uniqueness of this stage includes its mounting method, its rotational motion and the reduced crosstalk among the X, Y and Z axes.

No extra fixtures are required, and the XYZ stage can be easily placed on and removed from the AFM scanner. The scanning of the workpiece by AFM can be done without removing the stage or the workpiece.

There are various motions that can be generated using this XYZ stage, with the possible applied motions categorized as one-dimensional (only X, Y or Z), two-dimensional (XY, XZ or YZ) and three-dimensional (XYZ) motions. Each axis is controlled by an individual actuator and can be actuated independently. Many of the described motions have been applied in order to evaluate their performances. XYZ planar vibration cutting has shown the best machining results so far. The cutting

experiments were repeated many times with different experimental conditions and materials. In every case, the stages generated reasonably repeatable results.

6.1.2 Suppression of the Stiffness Limitation of the AFM Probe

In the AFM probe based nano mechanical machining technique, the stiffness of the AFM probe has been a major concern. A high stiffness cantilever is expensive; and, it is difficult to obtain larger depths of cut with a low stiffness cantilever, especially with hard/brittle materials, such as ceramic and glass.

In vibration-assisted nano mechanical machining, the stiffness limitation has been suppressed; and, it was possible to obtain a deeper depth of groove while using a similar magnitude of thrust force. The suppression of the limitation in probe stiffness was observed in both XY planar vibration-assisted and Z-axis vibration-assisted nano mechanical machining techniques. However, the stiffness limitation in Z-axis vibration-assisted nano mechanical machining was much higher than that of the XY planar vibration-assisted cutting, as the obtained depth was greater in XY vibration cutting.

The width of the machined channel can be controlled in XY plane vibration-assisted cutting. In the scribing method, the width of the machined channel is restricted by the probe shape and the maximum depth during machining. In vibration-assisted nano mechanical machining, the width of the channels are no longer limited by the depth of groove and the probe shape, rather the width of the channel is controlled by the XY stage motion.

Different cutting methodologies were tested in the fabrication of nano patterns, and vibration-assisted machining provided more depth of groove. Z-axis vibration and XY vibration machining did not damage the feature;, therefore, the accuracy can be maintained during vibration-assisted machining.

6.1.3 Calibration of AFM and Depth Identification

In nano mechanical machining, it is difficult to measure the cutting forces, as conventional force sensors cannot be used, due to the smaller magnitude of the forces (few nN to few μN). Most of the available calibration methods for AFM probe based nano mechanical machining were investigated; and, the extended force balance method was developed for AFM calibration.

The effects of the facet angle and tilting of the calibration artifact were investigated and are considered in the extended force balance method. The friction coefficient between the silicon artifact and diamond tip of the AFM probe was also investigated based on the literature. The friction coefficient values were different from those previously used for silicon and diamond-like carbon (DLC). The vertical stiffness of the cantilever provided by the vendor was also verified by measuring the frequency response function and using the receptance coupling method.

AFM probe based scribing was also investigated cutting, and the depths of groove at different machining conditions were identified from experimental and mathematical equations. Depth identification was performed for scribing; however, the width of the

groove and lowered cutting force of vibration-assisted nano mechanical machining resulted in the friction model not being able to identify the depth of groove.

6.2 Assumptions and Limitations

In the study of nano scale fabrication, there are many variables and unknowns, which are difficult to deal with; therefore, errors may arise from various sources. In this thesis, some of the unknown parameters were identified; and, as a result, the cutting methodology was improved.

The lateral calibration method is a complex method, and various studies with different methodologies can be found in the literature. It was observed that the calibration artefact facet angle, the friction coefficient between the diamond probe and the silicon artefact, the tilting angle and the stiffness of the cantilever could influence the lateral calibration factor. Therefore, accurate measurements of these parameters are necessary to calibrate the AFM. The tool shape and orientation can also influence the friction, which still requires study, as the friction model derived for nano scribing failed to predict the friction in vibration-assisted machining.

The AFM nano machining was investigated while placed in a room with no humidity and temperature control. Therefore, the effects of temperature and humidity may influence the reported parameters. The substrate fabricated in nano scribing and vibration-assisted machining may contain a water film of a few nanometers on its surface, which can provide lubrication to the probe sample interface.

The surface roughness and waviness plays an important role in the measurement of lateral cutting forces or the friction coefficient. The cutting force fluctuates, if the surface contains significant roughness and waviness. Therefore, the average friction coefficient is different than what it should be in reality. The grain boundaries of material can also influence the cutting forces. The surface roughness and grain boundary effects are ignored in the analysis of the cutting forces.

The workpiece preparation is important, as the required surface should be very flat. Sputtering and spin coating methods were used for preparing the workpiece in this thesis. However, the annealing or heating of the substrate is usually performed after the sputtering and spin coating to provide heat treatment and drive away moisture. However, the sample properties may vary, even from a similar substrate; therefore, workpieces with uniform properties are required to obtain uniform results.

There are many other parameters that can affect nano scale machining, such as instrument compliance, tip roundness, front and side pileup, and thermal drift. The cantilever may have several deflection modes; and, in this thesis, only the deflection from thrust and lateral forces were considered, since it was deemed that the vertical and lateral deflections were the dominant deflection modes.

6.3 Future Works

Cutting tool based nano mechanical machining is gaining ground, as the number of publications is increasing every year. Scholars from all around the world (e.g. Canada,

South Korea, and USA) are now concentrating on nano scribing, vibration-assisted machining, and CNC (computer numeric control) nano scribing.

Several challenges exist in AFM probe based nano scale machining. The small size of the cutting tool causes direct visualization problems; therefore, an understanding of nano scale material removal is difficult. The molecular dynamics simulation of nano scribing has been performed; however, simulation for vibration-assisted nano mechanical machining is still nonexistent.

Cutting simulation for macro and micro scales can be performed with different finite element analysis (FEA) simulation software; and, nano scale vibration-assisted cutting can be simulated by increasing the AFM probe size by several magnitudes. However, there is no FEA simulation software for molecular level interactions, which are one of the dominant factors in nano scale machining.

The calibration method can be more defined by incorporating thermal and humidity effects, so that the cutting force measurements are more accurate. The tool shape and orientation effects on calibration should be studied, as different sides of an AFM probe cut when 3D features are fabricated.

The friction model should be redefined for vibration-assisted nano mechanical machining. The depth of groove in vibration-assisted machining is quite large; therefore, the AFM probe based friction model and the single asperity model were not able to predict the friction phenomena in vibration-assisted machining.

AFM probe based machining can be used to characterize nanocomposite materials. The interaction of nano fillers and a polymer matrix can be identified by nano

scribing or vibration-assisted machining. The alignment effect of nano fillers on the cutting forces and friction can also be studied with nano scale machining.

Ultrasonic vibration can be also used in Z-axis vibration cutting; however, the power requirement to actuate the Z-axis actuator in the MHz range is quite large.

Nonetheless, there is theoretical evidence that, if the cantilever can be actuated in the MHz range or much higher than the natural frequency of the AFM probe, the AFM probe dynamically stiffens and depth control in Z-axis vibration cutting is possible. The experimental setup used in this research could not provide enough power to the actuator to actuate at the MHz range; therefore, experiments were not conducted.

REFERENCES

Archard, J.F., 1953, Contact and rubbing of flat surfaces, Journal of Applied Physics, 24: pp. 981

Asay, D.B., and Kim, S.H., 2006, Direct force balance method for atomic force microscopy lateral force calibration, Review of Scientific Instruments, 77: 043903(9pp).

Ahn, J.H., Lim, H.S., Son, S.M., 1999, Improvement of micromachining accuracy by 2Dimensional vibration cutting, Proc ASPE, 20: pp. 150–153.

Ahn, B.W., Lee, S.H., 2009, Characterization and acoustic emission monitoring of AFM nanomachining, Journal of Micromechanics and Microengineering, 19: 045028 (6pp).

Aurich, J.C., Dornfeld, D., Arrazola, P.J., Franke, V., Leitz, L., Min, S., 2009, Burr-analysis, control and removal, CIRP Annals - Manufacturing Technology, 58: pp. 519–542

Barel, I., Urbakh, M., Jansen, L., Schirmeisen, A., 2010, Multibond dynamics of nanoscale friction: the role of temperature, Physical Review Letters, 104 (6): pp. 066104 (1)- 066104 (4).

Becker, E. W., Ehrfeld, W., Hagmann, P., Maner, A., and Münchmeyer, D., 1986, Fabrication of microstructures with high aspect ratios and great structural heights by synchrotron radiation lithography, galvanoforming, and plastic moulding (LIGA process), Microelectronic Engineering, 4: pp. 35-56.

Bhushan, B., 2005, Nanotribology and nanomechanics, Wear, 259: pp. 1507-1531.

Bhushan, B., 2011, Nanotribology and nanomechanics II: Nanotribology, Biomechanics and Industrial Applications, 3rd edition, Springer Publication.

Bifano, T.G., Dow, T.A., Scattergood, R.O., 1991, Ductile-regime grinding: a new technology for machining brittle materials, Journal of Engineering for Industry, 113 (2): 184-189.

Binning, G., Quate, C.F., Gerber, Ch., 1986, Atomic force microscopy, Physical Review Letters, 56(9): pp. 930-934

Biswas, S.K., Kailas, S.V., 1997, Strain rate response and wear of metals, Tribology International, 30(5): pp. 369-375.

Bitter, J.G.A., 1963, A study of erosion phenomena part I, Wear, 6(1): pp. 5-21.

Blake, P.N., 1990, Ductile regime machining of germanium and silicon, Journal of the American Ceramics Society, 73 (4): pp. 949-957.

Brehl, D.E., Dow, T.A., 2008, Review of vibration-assisted machining, Precision Engineering, 32 (3): pp. 153-172.

Brinksmeier, E., Glabe, R., 1999, Elliptical vibration cutting of steel with diamond tools, American Society of Precision Engineers Conference Proceedings, 20: pp. 163-166.

Byrne, G., Dornfeld, D., Denkena, B., 2003, Advancing cutting technology, Annals of CIRP, 52(2): pp. 483-507.

Cappella, B., Dietler, G., Force-distance curves by atomic force microscope, Surface Science Reports, 34: pp.1-104.

Cerniway, M.A., 2001, Elliptical diamond milling: kinematics, force, and tool wear. MS thesis, North Carolina State University.

Chae, J., Park, S.S., 2007, High frequency bandwidth measurements of micro cutting forces, International Journal of Machine Tools & Manufacture, 47: pp.1433–1441.

Chau, R., Datta, S., Doczy, M., Doyle, B., Jin, B., Kavalieros, J., Majumdar, A., Metz, M., Radosavljevic, M., 2005, Benchmarking nanotechnology for High-performance and low-power logic transistor applications, IEEE Transaction on Nanotechnology, 4(2): pp. 153-158

Christy, L.H., Richard, P.V.D., L., 2001, Nanosphere lithography: a versatile nanofabrication tool for studies of size-dependent nanoparticle optics, Journal of Physical Chemistry B, 105: pp. 5599-5611.

Dornfeld, D., Min, S., Takeuchi, Y., 2006, Recent advances in mechanical micromachining, Annals of CIRP, 55(2): pp.745-768.

Finnie, I., 1960, Erosion of surfaces by solid particles, Wear, 3: pp. 87-103.

Furukawa, Y., Moronuki, N., 1988, Effect of material properties on ultra precise cutting processes, Annals of CIRP, 37 (1): pp. 113-116.

Gahr, K.H.Z., 1998, Wear by hard particles, Tribology International, 31(10): pp. 587-596.

Gauthier, C., Lafaye, S., Schirrer, R., 2001, Elastic recovery of a scratch in a polymeric surface: experiments and analysis, Tribology International, 34(7): pp. 469-479.

Gnecco, E., Bennewitz, R., Gyalog, T., Loppacher, Ch., Bammerlin, M., Meyer, E., and Güntherodt, H,-J., 2000, Velocity dependence of atomic friction, Physical Review Letter, 84(6): pp. 1172-1175.

Goddard, J., Wilman, H., 1961, A theory of friction and wear during the abrasion of metals, Wear, 5: 114-135.

Gozen, B.A., Ozdoganlar, O.B., 2010, A rotating-tip-based mechanical nano-manufacturing process: nanomilling, Nanoscale Research Letter, 5: pp. 1403–1407.

Hirai, Y., Yoshida, S, Takagi, S., Takagi, S., Tanaka, Y., Yabe, H., Sasaki, K., Sumitani, H., 2002, High aspect pattern fabrication by nano imprint lithography using fine diamond mold, Microprocesses and Nanotechnology Conference, Nov.6-8, Tokoyo Japan, pp. 26-27.

Hokkirigawa, K., Kato, K., 1988, An experimental and theoretical investigation of ploughing, cutting and wedge formation during abrasive wear, Tribology International, 21(1): pp. 51-57.

Jalili, N., Laxminarayana, K., 2004, A review of atomic force microscopy imaging systems: application to molecular metrology and biological sciences, Mechatronics, 14: pp. 907-945.

Jin, M., Murakawa, M., 2001, Development of a practical ultrasonic vibration cutting tool system, Journal of Material Processing Technology, 113 (1-3): pp. 342-347.

Karp, J,H., Tremblay, E.J., and Ford, J.E., 2010, Planar micro-optic solar concentrator, Optics Express, 18(2): pp. 1122-1133.

Khurshudov, A.G., Kato, K., Koide, H., Wear of the diamond tip sliding against silicon, Wear, 203-204: pp. 22-27.

Kovacevic, R., 1991, Surface texture in abrasive waterjet cutting, Journal of Manufacturing Systems, 10(1): pp. 32-40.

Kulkarni, A.V., Bhushan, B., 1996, Nano/pico indentation measurements on single-crystal aluminum using modified atomic force microscopy, Materials Letters, 29(4-6): pp. 221–227.

Lawn, B.R, Marshall, D.B., 1978, Hardness, toughness, and brittleness: an indentation analysis, Journal of The American Ceramic Society, 62 (7-8): pp. 347-350.

Li, Q., Dong, Y., Perez, D., Martini, A., Carpick, R.W., 2011, Speed dependence of atomic stick-slip friction in optimally matched experiments and molecular dynamics simulations, Physical Review Letters, 106(12): pp. 126101(1)-126101(4).

Liu, X., DeVor, R.E., Kapoor, S.G., Ehmann, K.F., 2004, The mechanics of machining at the microscale: assessment of the current state of the science, Transaction of ASME, 126: pp. 666-678.

Lucca, D.A., Herrmann, K., Klopfstein, 2010, M.J., Nanoindentation: measuring methods and applications, Annals of CIRP, 59(2): pp. 803-819.

Ma, C.X., Shamoto, E., Moriwaki, T., Zhang, Y., Wang, L., 2005, Suppression of burrs in turning with ultrasonic elliptical vibration cutting, International Journal of Machine Tools & Manufacture, 45: pp. 1295-1300.

Magonova, S.N., Elingsa, V., Whangbo, M.-H., 1997, Phase imaging and stiffness in tapping-mode atomic force microscopy, Surface Science, 375 (2-3): pp. L385-L391.

Malekian, M.M, Park, S.S., Jun, M.B.G., 2009, Tool wear monitoring of micro-milling operations, Journal of Material Processing Technology, 209(10): pp. 4903-4914.

Malekian, M., Park, S.S., Strathearn, D., **Mostofa, M.G.**, Jun, M.B.G., 2010, Atomic force microscope probe-based nanometric scribing, Journal of Micromechanics and Micro Engineering, 20(11): 115016.

Malekian, M., 2010, Investigation of micro milling process, PhD Thesis, University of Calgary, Canada.

Malekian, M., **Mostofa, M.G.,** Park, S.S., Jun, M.B.G., 2012 Modeling of minimum uncut chip thickness in micro machining of aluminum, Journal of Materials Processing Technology, 212(3): 553-559.

Mao, P., Han, J., 2005, Fabrication and characterization of 20 nm planar nanofluidic channels by glass–glass and glass–silicon bonding, Lab on a Chip, 5: pp. 837-844,

Mehrpouya, M., Park, S.S., 2011, Prediction of atomic force microscope probe dynamics through the receptance coupling method. Review of Scientific Instruments, 82: pp. 125001.

Moriwaki, T., Shamoto, E., Inoue, K., 1992, Ultraprecision ductile cutting of glass by applying ultrasonic vibration, Annals of CIRP, 41(1): pp. 41 (ductile cutting of brittle material)

Moriwaki, T., Shamoto, E., 1995, Ultrasonic elliptical vibration cutting, Annals of CIRP, 44: pp. 31–34. (burr supression)

Mostofa, M.G., Noh, J.H., Ahn., J.H., Kang, D.B., 2010, Tooling device design for vibration-assisted high speed shaping of PMMA, Journal of Mechanical Science and Technology, 24 (8): pp. 1623-1629.

Mostofa, M.G., Park, C.I., Park, S.S., 2013, AFM probe based nano mechanical scribing of soda lime glass, Journal of manufacturing processes, 15(4): pp. 625-634.

Nakasuji, T, Kodera, S., Hara, S, Matsunaga, Ikawa, N, Shimada, S, Diamond turning of brittle material for optical components, Annals of CIRP, 1990: 39 (1): 89-92.

Nath, C., Rahman, M., 2008, Effect of machining parameters in ultrasonic vibration cutting, International Journal of Machine Tools and Manufacture, 48(9): pp. 965-974.

Nath, C., Rahman, M., Neo, K.S., 2009, Machinability study of tungsten carbide using PCD tools under ultrasonic elliptical vibration cutting. International Journal of Machine Tools & Manufacture, 49: 1089-1095.

Neilson, J.H., Gilchrist, A., 1968, Erosion by a stream of solid particles, Wear, 11(2): pp. 112-122.

Ngoi, B.K.A, Sreejith, P.S., 2000, Ductile regime finish machining, International Journal of Advanced Manufacturing Technology, 16: 547-550.

Notargiacomo, A., Foglietti, V., Cianci, E., Capellini, G., Adami, M., Faraci, P., Evangelisti, F., Nicolini, C., 1999, Atomic force microscopy lithography as a nanodevice development technique, Nanotechnology, 10: pp. 458–463.

Oliver, W.C., Pharr, G.M., 2004, Measurement of hardness and elastic modulus by instrumented indentation, Journal of Material Research, 19(1): pp. 3-20.

Park, J.W., Lee, C.M., Choi, S.C., Kim, Y.W., Lee, D., 2008, Surface patterning for brittle amorphous matrial using nanoindenter-based mechanochemical nanofabrication, Nanotechnology, 19(8): 085301-5.

Park, S.S., Malekian, M., 2009, Mechanistic modeling and accurate measurement of micro end milling forces, Annals of CIRP, 58(1): 49-52.

Phillips, G.K., 2004, Security document with nano pattern, US Patent, US6692030 B1.

Piner, R.D., Zhu, J., Xu, F., Hong, S., Mirkin, R.D., 1999, Dip-pen nanolithography,

Science, 283: pp. 661-663.

Puttik, K., 1980, The correlation of fracture transitions, Journal of Physics D: Applied Physics, 13: 2249-62.

Rahnama, R., Sajjadi, M., Park, S.S., 2009, Chatter suppression in micro end milling with process damping, Journal of Material Processing Technology, 209(17): pp. 5766-5776.

Ruan, J.A., Bhushan, B., 1994, Atomic-scale friction measurements using friction force microscopy Part I general principles and new measurement techniques, ASME Journal of Tribology, 116(2): pp. 389-396.

Sajjadi, M., Malekian, M., Park, S.S., 2009, Investigation of micro scratching and machining of glass, Proceedings of the 2009 ASME International Manufacturing Science and Engineering Conference, West Lafayette, Indiana, October 4-7.

Salvadori, M.C., Lisbao, F.S., Fernandes, F.M., 2008, Novel method for measuring

nanofriction by atomic force microscope, Journal of Vacuum Science & Technology B, 26(2): pp. 643-650.

Shamoto, E., Moriwaki, T., 1994, Study on elliptical vibration cutting, Annals of CIRP, 43(1): pp. 35-38.

Shamoto, E., Moriwaki, T., 1999, Ultraprecision diamond cutting of hardened steel by applying elliptical vibration cutting. Annals of CIRP, 48(1): pp. 441-444.

Shamoto E., Suzuki, N., Tsuchiya, E., Hori, Y., Inagaki, H., Yoshino, K., 2005, Development of 3 DOF ultrasonic vibration tool for elliptical vibration cutting of sculptured surfaces, Annals of CIRP, 54(1): pp. 321-324.

Shekhawat, G.S., Dravid, V.P., 2005, Nanoscale imaging of buried structures via scanning near-field ultrasound holography, Science, 310 (5745): pp. 89-92.

Shimada, S., Ikawa, N., Tanaka, H., Ohmori, G., Uchikoshi, J., Yoshinaga, H., 1993, Feasibility study on ultimate accuracy in microcutting using molecular dynamics simulation, Annals of CIRP, 42(1): pp. 91-94.

Shin, W.K., An, J.H., Jeong, H.D., 2011, Optimization of the physical cleaning conditions for nanotechnology, Annals of CIRP, 60: pp. 579-582.

Sills, S., Overney, R.M., 2003, Creeping friction dynamics and molecular dissipation mechanism in glass polymers, Physical Review Letters, 91(9): pp. 095501(1)-095501(4)

Sin, H., Saka, N., Suh, N.P., 1979, Abrasive wear mechanics and grit size effect, Wear, 55: 163-190.

Sreejith, P.S., Ngoi, B.K.A., 2001, New materials and their machining, International Journal of Advance Manufacturing Technology, 18: pp. 537–544.

Tambe, N.S., Bhusan, B., 2004, Scale dependence of micro/nano-friction and adhesion of MEMS/NEMS materials, coatings and lubricants. Nanotechnology, 15: pp. 1561-1570.

Tambe, N.S., Bhusan, B., 2005, Friction model for the velocity dependence of nanoscale friction. Nanotechnology, 16: pp. 2309-2324.

Taniguchi, N., 1983, Current status in, and future trends of, ultra precision, machining and ultrafine materials processing, Annals of CIRP, 32(2): pp.573-582.

Tautz, J., Roces, F., Hölidobler, B., 1995, Use of a sound based vibratome by leaf cutting ants, Science, 267: pp.84-86.

Uddin, S.M., Seah, K.H.W., Li, X.P., Rahman, M., Liu, K., 2004, Effect of crystallographic orientation on wear of diamond tools for nano-scale ductile cutting of silicon, Wear, 257: 751–759.

Urbakh, M., Klafter, J., Gourdon, D., Israelachvili, J., 2004, The non linear nature of friction, Nature, 430: pp. 525-528.

Varenberg, M., Etsion, I., and Halperin, G., 2003, An improved wedge calibration method for lateral force in atomic force microscopy, Review of Scientific Instruments, 74: pp. 3362–7.

Vieu, C., Carcenac1, F., Pépin, A., Chen, Y., Mejias, M., Lebib, A., Manin-Ferlazzo, L., Couraud, L., Launois, H., 2000, Electron beam lithography: resolution limits and applications, Applied Surface Science, 164(1-4): pp. 111-117.

Vijay, S., Pamula, V.k., Fair, R.B., 2004, An integrated digital microfluidic lab-on-a-chip for clinical diagnostics on human physiological fluids, miniaturisation for chemistry, Biology & Bioengineering, 4: pp. 310-315.

Vogler, M.P., DeVor, R.E., Kapoor, S.G., 2004, On the modeling and analysis of machining performance in micro-end milling, Part I: surface generation, Journal of Manufacturing Science and Engineering, Transactions of the ASME, 126(4): pp. 685-694.

Vollertsen, F., Biermann, D., Hansen, H.N., Jawahir, I.S., Kuzman, K., 2009, Size effect in manufacturing of metallic components, Annals of the CIRP, 58: 566-587.

Wang, F., Zhao, X., 2007, Effect of contact stiffness on wedge calibration of lateral force in atomic force microscopy, Review of Scientific Instruments, 78(4): 043701 (4pp).

Wang, H., Feng, J., Hu, X., Ng, K.M., 2008, Tribological behaviors of aligned carbon nanotube/fullerene-epoxy nanocomposites, Polymer Engineering and Science, 48(8): pp. 1467-1475.

Wei, Z., Zhao, Y.P., Ruan, S.L., Gao, P., Yu, T.X., 2006, A study of the tribological behaviour of carbon-nanotube-reinforced ultrahigh molecular weight polythene composites, Surface and Interface Analysis, 38: pp. 883-886.

Yabu, H., Shimomura, M., 2005, Simple fabrication of micro lens arrays, Langmuir, 21: pp. 1709-1711.

Yan, Y.D., Sun, T., Dong, S., Luo, X.C., Liang, Y.C., 2006, Molecular dynamics simulation of processing using AFM pin tool, Applied Surface Finish, 252: pp. 7523-7531.